Dissertation
submitted to the
Combined Faculties for the Natural Sciences and for Mathematics
of the Ruperto-Carola University of Heidelberg, Germany
for the degree of
Doctor of Natural Sciences

presented by

Diplom-Biochemiker Mihály Koltai

born in Budapest, Hungary

Oral examination: May 2016

Quantitative analysis of microbial sensing and motility

Referees:

Prof. Dr Victor Sourjik

Prof. Dr Ursula Kummer

Szüleimnek és nővéremnek

Acknowledgements

I would like to sincerely thank my advisor Professor Dr Victor Sourjik for a multitude of reasons. First, for accepting me in his group, in which I have found a friendly and cooperative environment to do science and where I have gained much both in terms of knowledge and as a person during my PhD. From the very beginning he provided me with a model to emulate as to how science, and specifically quantitative biology, should be done: for the thrill of discovery itself, seeking organizing principles to make sense of the data biology inundates us with. I have been happy to have an advisor who welcomed and encouraged new ideas and initiatives if he saw scientific merit, while gently dissuading when foreseeing a dead-end.

Among my colleagues I must thank first of all Dr Alvaro Banderas and Dr Alexander Anders, my experimental collaborators in the project on yeast mating. What started as a brief collaboration to provide some quantitative intuition for yeast mating experiments grew into the main thrust of my PhD thesis. I feel that through our collaboration we highlighted some fundamentals of this intriguing signaling and regulatory system that had been neglected by the bulging systems biology literature on the yeast mating pathway. We unexpectedly found intelligence and even, in a sense, powers of 'foreseeing the future' in a unicellular microbe. It has been a pleasure to work and think together, to discuss and discard ideas, sometimes at unlikely hours and venues, combining data and theory, to arrive finally at an overarching narrative that surprised us with its coherence. I would also like to thank Dr Carey Nadell from Professor Dr Knut Drescher's group for his help on evolutionary modeling.

I would like to thank Professor Dr Kai Thormann and Dr Sebastian Bubendorff of *Justus-Liebig-Universität Gießen* for the collaboration on the motility of the bacteria *Shewanella*, a project that led to a joint publication. The members of my Thesis Advisory Committee, Professor Dr Ursula Kummer and Dr Ilka Bischofs gave me useful advice on which way (not) to go. I thank them for their guidance and expertise. I would like to thank Dr Jürgen Pahle for being on my defence committee as the fourth member.

I have made numerous friends these years, some of whom had left the group meanwhile; I would like to thank Mohit, Gabriele, Alex, Alvaro, Silke, Anja, Iaroslav, Vihang, Rahul, Yu and my other colleagues for friendship and a healthy work environment.

Finally, I thank my family for their support. I needed their support and advice many times and they were always there for me. *Köszönöm.*

Summary

Microbes need to extract relevant information from their environment and use this information to produce adequate behavioral responses that ensure their survival. Quantitative, mathematical analysis of microbial sensory systems (such as various signaling pathways) and their effectors (such as bacterial motors) forms the basis of the field of systems biology. Because of their relative simplicity, in comparison with analogous systems in multicellular organisms, these structures are more amenable to quantitative modelling. In this dissertation I present the quantitative analysis of three microbial sensory-effector systems, two in bacteria and one in the unicellular eukaryote *Saccharomyces cerevisiae*. In all three cases I look at a behavior that is an evolutionarily selected response to a given problem that the microorganism is confronted with. I then explain the mechanistic basis of this response in the sensory or effector system by a mathematical model.

In the first case, mating in yeast cells, the problem the cells need to solve is to establish the likelihood of mating and invest cellular resources accordingly to prepare for the mating event. The solution that wild-type yeast $MAT\mathbf{a}$ cells have evolved to tackle this problem is fractional sensing, the ability to sense robustly the fraction of partner cells in a mixed population. The mechanism that enables this behavior is the degradation of the partner cells' pheromone signal by a secreted enzyme. I show mathematically that the necessary consequence of this mechanism is the rescaling of the signal strength proportionally to the *fraction* of partner cells, as opposed to their absolute quantity. Additionally, I also explain the experimentally observed difference between the fractionally sensing wild-type cells and the mutants performing absolute sensing, due to the latter's lack of a signal attenuation mechanism. Moreover, by a cost-benefit model of mating, I show that the strategy of fractional sensing and resource investment is optimal, as compared to sensing the absolute amount of partners.

In the second case, I look at the most prevalent bacterial signaling systems, the so-called two-component systems and their capacity to generate bistability, or, in behavioral terms, memory. In the case of two-component systems that control developmental processes, an irreversible shift is required at the level of individual cells: once the system is turned 'on', it should not revert to its 'off' state, within some range of the input. At the population level, because of the stochasticity of chemical reactions and variation in expression levels, a bistable control system can result in a bimodal distribution with some cells in 'on' and others in 'off' state. In fluctuating and unpredictable environments this strategy of 'bet hedging' is another advantageous feature of bistability. I first describe post-translational mechanisms that can generate bistable behavior and analyze the parametric properties of bistable systems. Second, I show that the transcriptional

auto-induction of pathway components can lead to bistability in the 'canonical' two-component system with a bifunctional sensor kinase as well, a question not resolved in the previous literature.

In the third case, I analyze the motility of the marine bacteria *Shewanella putrefaciens*. Higher efficiency of spreading and chemotaxis is expected to lead to higher fitness as it enables a bacterial population to better explore and exploit the resources of its environment. Wild-type *Shewanella* cells achieve this higher efficiency by inducing a lateral flagellar system, leading to a lower mean turning angle. By lowering the mean of the turning angle distribution, the presence of the lateral flagella leads to higher directional persistence and hence increased spreading efficiency. By both analytical calculations and stochastic simulations I reproduce the experimentally observed trends of spreading. Furthermore, I show that in shallow gradients the higher directional persistence also leads to higher chemotactic efficiency.

By mathematical analysis I was able to identify the mechanisms underlying these evolutionarily selected behaviors. Moreover, in the case of yeast mating, I also showed that the observed behavior of fractional sensing is optimal in cost-benefit terms. In the case of transcriptionally induced bistability in bacterial two-component systems, the analysis identified parametric properties of bistable systems that can be potentially used to engineer monostable signaling systems into bistable ones experimentally.

Zusammenfassung

Mikroorganismen müssen relevante Informationen aus ihrer Umwelt wahrnehmen und verwenden, um geeignete Verhaltensantworten zu geben, die ihr Überleben sichern. Die quantitative, mathematische Analyse von mikrobiellen Sinnessystemen (wie Signaltransduktionswegen) und den zugehörigen Effektoren (wie bakteriellen Motoren) bildet die Grundlage des Wissenschaftsfeldes der Systembiologie. Aufgrund ihrer relativen Unkompliziertheit im Vergleich zu analogen multizellulären Systemen sind diese Systeme zugänglicher für quantitative Modellierung. In der vorliegenden Dissertation präsentiere ich die quantitative Analyse von drei mikrobiellen Sensor-Effektor-Systemen - zwei bakteriellen sowie einem System des unizellulären Eukaryonten *Saccharomyces cerevisiae*. In jedem dieser Fälle betrachte ich ein Verhaltensmuster, das eine evolutionär selektierte Reaktion auf ein gegebenes Problem ist, mit dem der Mikroorganismus konfrontiert wird. Ich erkläre und analysiere dann die mechanistische Grundlage des Verhaltensmusters innerhalb des relevanten sensorischen oder Effektorsystems mithilfe eines mathematischen Modells.

Im ersten Fall untersuche ich das Paarungsystem von *S. cerevisiae*. Das Problem, welches die Zellen hier lösen müssen, ist die Ermittlung der Wahrscheinlichkeit einer Paarung (bzw. anders ausgedrückt die Wahrscheinlichkeit, eine Partnerzelle zu finden) und eine dementsprechende Investition von zellulären Ressourcen in die Vorbereitung auf das Paarungsereignis. Die Lösung dieses Problems, die die Zellen des Paarungstypes $MAT\mathbf{a}$ entwickelt haben, ist die fraktionelle Perzeption, d.h. die Fähigkeit, in einer gemischten Population den relativen Anteil von Partnerzellen festzustellen. Der Mechanismus, der dieses Verhaltensmuster ermöglicht, basiert auf der Degradation des Pheromonsignals der Partnerzellen (Sender) durch ein von den Empfängerzellen sekretiertes Enzym. Ich zeige mathematisch, dass das Ergebnis dieses Mechanismus ein Umskalieren der Signalstärke proportional zum Anteil der Partnerzellen, im Gegensatz zu ihrer absoluten Menge, ist. Das mathematische Model kann zudem den experimentell beobachtbaren Unterschied zwischen Wildtypzellen mit fraktioneller Perzeption und Mutanten ohne Signaldämpfungsmechanismus, welche die absolute Menge der Partnerzellen wahrnehmen, erklären. Weiterhin zeige ich, dass die Strategie von fraktioneller Perzeption und dazu proportionaler Investition von Ressourcen optimal ist im Vergleich zur Perzeption der absoluten Menge von Partnerzellen.

Im zweiten Fall untersuche ich die am häufigsten vorkommenden bakteriellen Signaltransduktionswege, sogenannte Zweikomponentensysteme, und ihre Kapazität zur Ausbildung von Bistabilität bzw., anders ausgedrückt, Erinnerungsvermögen. Im Fall von

Zweikomponentensystemen, die Entwicklungsprozesse kontrollieren, müssen individuelle Zellen einen irreversibelen Übergang durchlaufen: wenn das System "angeschaltet" ist, soll es im Fall einer Absenkung des Eingangssignals (zumindest innerhalb eines bestimmten Bereichs) nicht in seinen Ausgangszustand zurückkehren. Auf Populationsebene führt solch ein bistabiles Kontrollsystem wegen Stochastizitäten der chemischen Reaktionen und interzellulären Unterschieden in der Genexpression zu bimodalen Verteilungen mit einigen Zellen im Aus- und anderen im Ein-Zustand. In einer schwankenden und unvorhersehbaren Umwelt ist diese Strategie von "bet-hedging" (ein Absichern nach allen Seiten) ein zusätzlicher Vorteil von Bistabilität. Erstens beschreibe ich in der vorliegenden Arbeit posttranslationale Mechanismen, die zu Bistabilität führen können, und analysiere die Parametereigenschaften der bistabilen Systeme. Zweitens demonstriere ich, dass transkriptionelle Autoinduktion von Komponenten des Signaltransduktionswegs im "kanonischen" Zweikomponentensystem mit einer bifunktionellen Kinase ebenfalls zu Bistabilität führen kann.

Im dritten Fall analysiere ich die Motilitätmuster des marinen Bakteriums *Shewanella putrefaciens*. Neben einem polaren Flagellensystem exprimieren *Shewanella*-Zellen ein zweites, laterales Flagellensystem, was zu einer Verringerung des Durschnittswinkels bei Änderungen der Bewegungsrichtung führt. Diese Tatsache führt zu einer höheren Effizienz von Ausbreitung und Chemotaxis, was die Fitness der Bakterien erhöht, da dies eine bessere Erkundung und Ausbeutung der Umweltressourcen ermöglicht. Mithilfe analytischer Ableitungen als auch stochastischer Simulationen reproduziere ich die experimentellen Beobachtungen. Weiterhin demonstriere ich, dass in flachen Gradienten der durch das zusätzliche Flagellensystem bewirkte geringere durchschnittliche Umkehrwinkel und eine damit einhergehende ausgeprägtere direktionale Persistenz zu besserer Chemotaxis führt.

Mithilfe mathematischer Analyse war ich imstande, die den evolutionär selektierten Verhaltensmustern zugrunde liegenden Mechanismen zu identifizieren. Im Fall der Analyse des Paarungssystems von Hefezellen konnte ich zudem demonstrieren, dass das beobachtete Verhalten der fraktionellen Perzeption unter Kosten/Nutzen-Gesichtspunkten optimal ist. Im Fall der transkriptionell induzierten Bistabilität in bakteriellen Zweikomponentensystemen wurden durch die Analyse parametrische Bedingungen identifiziert, die potentiell dazu verwendet werden können, ein monostabiles System experimentell in ein bistabiles System umzuwandeln.

Project aims

In my dissertation I present the quantitative analysis of three cases of microbial sensing and/or motility. I summarize below the main aims of the three projects contained in the dissertation.

Section 1: **Microbial sensing and decision making: yeast mating**

The sexually reproducing unicellular eukaryote *Saccharomyces cerevisiae* has evolved a pheromone-based communication system to regulate its mating behavior in accordance with the availability of mating partners. In this project I quantitatively analyzed this regulatory behavior, both in mechanistic and cost-benefit terms. Specifically, my first aim was to analyze mathematically the mechanism behind the fractional sensing behavior that $MAT\mathbf{a}$ yeast cells show in their partner sensing. Second, I explored if the observed behavior of relative (fractional) sensing and pathway induction was an optimal strategy, compared to the absolute sensing behavior of mutants without a signal attenuation mechanism.

This work was done in collaboration with my colleagues Dr Alvaro Banderas and Dr Alexander Anders. The author of this dissertation performed all mathematical and computational analysis and wrote the corresponding sections of a manuscript ("*Sensory input attenuation allows predictive sexual response in yeast*"), at the time of writing under the second round of review. All experimental work was carried out by my co-workers.

Section 2: **Microbial memory: bistability in bacterial two-component systems**

Two-component systems are the most widespread environmental sensors in the bacterial kingdom, regulating diverse physiological processes in bacterial cells. The aim of the project was to systematically investigate the question whether two-component systems are capable of showing bistable behavior either due to post-translational or transcriptional mechanisms.

I used an algebraic method to analyze several topologies with different post-translational mechanisms for their capacity to be bistable. After identifying the topologies capable of bistability, I performed parameter sampling, made efficient by the algebraic simplification of the system, to find the parameters critical for bistable behavior.

In the second approximation, I performed the same analysis with the transcriptional auto-induction of pathway components included, to see if transcriptionally induced bistability is possible in the minimal two-component system with a bifunctional sensor kinase.

Section 3: **Microbial motility: increased directional persistence by lateral flagellation**

An organism's ability to actively move, and thereby better explore and exploit the resources of its environment is a basic evolutionary adaptation that is already present in bacteria. Movement in bacteria occurs both in the form of uniform spreading and biased movement along chemical gradients (chemotaxis), the efficiency of both kinds of movements depending on motility parameters such as speed or directional persistence.

The aim of this project was to explain the higher spreading efficiency of the laterally flagellated wild-type cells of the marine bacteria *Shewanella putrefaciens* compared to mutants having only a polar flagellar system. Experimental data showed that the laterally flagellated wild-type cells have a different turning angle distribution with a lower mean. I performed analytical calculations to explore the effect of the lower mean turning angle on the efficiency of spreading, while also using more detailed stochastic simulations including the backtracking behavior of cells. Moreover, I also investigated the effects of the turning angle distribution on chemotactic efficiency.

This work was done in collaboration with the group of Professor Dr Kai Thormann. The results were published in the article *Secondary bacterial flagellar system improves bacterial spreading by increasing the directional persistence of swimming*, in *Proceedings of the National Academy of Sciences (2014), 111, 31, 11485-11490* [27], with the author of this dissertation as an equal first contributor. All computational work was performed by the author of this dissertation, along with writing the corresponding sections of the manuscript. All experimental work was carried out by Dr Sebastian Bubendorfer and Florian Rossmann.

Contents

1 Microbial sensing and decision making: yeast mating

1.1 Introduction: mating in *Saccharomyces cerevisiae*

In a sexually reproducing microbe such as the yeast species *Saccharomyces cerevisiae*, one essential form of sensing and decision-making is the detection of available sexual partners and, as a function of this information, the initiation of cellular processes required for mating. In *S. cerevisiae*, the two haploid mating types, $MAT\boldsymbol{a}$ and $MAT\alpha$ cells, rely on mutual pheromone-based communication to sense each others' presence.

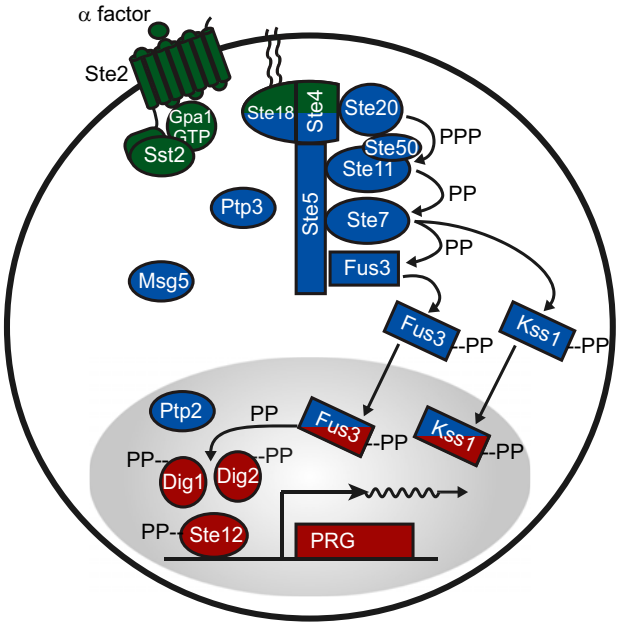

Figure 1. Components of the yeast mating pathway. In $MAT\mathbf{a}$ cells the input ligand is α-factor that binds to the G protein-coupled receptor $Ste2$. The dimer $Ste4-Ste18$ is then released from the inhibitory $G\alpha$ subunit $Gpa1$. The scaffold protein $Ste5$ is recruited to the cell membrane and docks downstream kinases. $Ste11$, $Ste7$ and $Fus3$ are the sequentially activated kinases of the MAPK cascade. The activated MAPK $Fus3$ phosphorylates the transcriptional regulators $Ste12$, $Dig1$, and $Dig2$, leading to the activation of pheromone-associated genes. Activated $Fus3$ also phosphorylates other substrates causing morphological changes and the arrest of the cell cycle. The phosphatases $Msg5$, $Ptp2$, and $Ptp3$ interact with the kinases as negative regulators. Image from [154].

A specialized signaling pathway, the *mating pathway* has evolved in yeast to detect these pheromone signals and convey the information from the membrane-bound receptor Ste2 to the nucleus, as shown in Figure 1. The molecular details and quantitative properties of the mating pathway have been extensively studied in recent decades, both experimentally and theoretically [12, 41, 74, 80, 98, 112, 119]. Expression of genes associated with the mating pathway is a *cost*ly

decision (Figure 18), slowing down growth, potentially inducing cell-cycle arrest and leading to mating-specific morphological changes. At the same time, induction of the mating pathway is required for mating, to have the *benefits* of sexual reproduction [8, 20, 37, 69, 93, 137].

Therefore, sensing the availability of partner cells, or more generally, the likelihood of mating, and initiating the required cellular processes is crucial and can be described as an optimization task [10, 25, 38, 54, 116] of the fitness trade-off between the costs and benefits of mating response induction.

In most studies of yeast mating, cells are immobilized on a solid surface with respect to each other (Figure 2*a*). In this case, it is the distance between mates and their ability to grow mating projections towards each other that primarily determines the likelihood of mating [9]. In such a situation, pheromone gradients can allow the cells to determine the direction toward, and under some circumstances, the distance from their mating partners. Only in the case of close proximity of a partner cell would a mating attempt be triggered, because only then would the pheromone concentration be sufficiently high. Several studies hypothesized that the barrier peptidase Bar1 [96] secreted by *MAT**a*** cells, responsible for degrading α-pheromone, enhances the precision of directional sensing [13, 104, 128]. The correct orientation of mating projections is necessary for mating. But this already presupposes that cells are immobilized and in immediate proximity of each other. Mating of haploid yeast cells often occurs within the ascus containing the spores [79], but haploid cells can also be released by ascus degradation (e.g. in the gut of fruit-flies [36]).

In this case, unlike in the spore, there can be significant variation in the ratio of the two mating types and proximity is achieved by specific sexual aggregation via α/a-agglutinins, expressed on the cell surface of the respective mating types [92, 124, 171]. This ecologically also relevant scenario of mating can occur in a suspension of cells mixed in liquid or following the detachment and mixing of cells that have been growing on a liquid covered surface (e.g. leaves). If cells are in a suspension, aggregation is a precondition of mating (Figure 2) and mating efficiency is determined by the probability of random encounters of cells. This in turn is a function of *global population parameters*, namely the total density (concentration of cells) ρ_T and the composition of the population, which can be defined by the fraction of one of the mating types. From here on, I denote the fraction of *MAT*α-cells as θ_α.

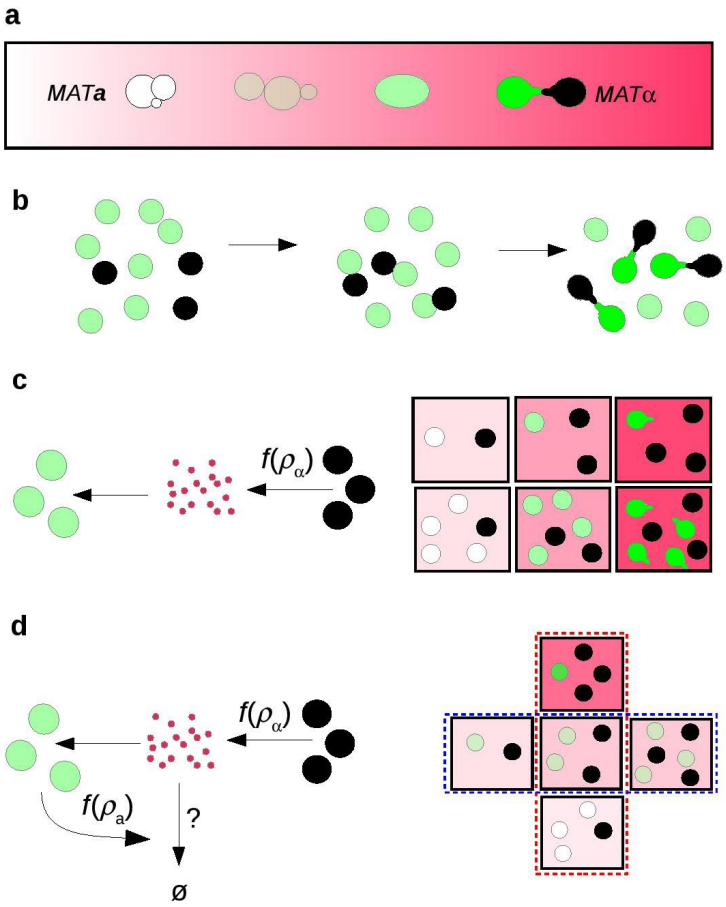

Figure 2. Partner sensing in yeast mating. **a.** For yeast mating on a surface, pheromone levels can convey spatial information. *MAT**a*** cells (white/green) can use of α-factor concentration (pink) as a signal for the distance of potential mating partners (*MAT*α cells; black), inducing transcriptional response (green), cell-cycle arrest and morphological changes. Formation of the mating protrusion (shmoo; right) only occurs at high levels of the α-factor. The pheromone gradient can guide the orientation of the shmoo. **b.** For yeast mating in suspension, the first step of mating is sexual aggregation following random collisions of cells. The probability for a given *MAT**a*** cell to mate is determined by the abundance of both cell types. **c.** Pheromone communication without signal attenuation, α-factor denoted with pink circles. Higher numbers of *MAT*α cells results in higher α-factor concentration (upper row). The α-factor concentration would be the same however with a larger number of recipient *MAT**a*** cells (lower row), although the mating probability for a *MAT**a*** cell is different in this case. Also, overstimulation of recipient cells may occur (rightmost panel). **d.** A signal attenuation mechanism dependent on *MAT**a*** density (ρ_a) can align the response to the mating likelihood by separating the two population parameters, the absolute emitter density (blue box; fraction of emitters constant, while the total density changes) and the relative emitter density (red box; total population density constant, while population composition changes). By this mechanism overstimulation and premature shmooing can also be avoided. Figure from joint manuscript, figure created by Dr Alvaro Banderas.

In this context, where mating is a mass-action-like process driven by global population parameters, we hypothesized that pheromone signaling and the signal attenuation mechanism through Bar1 can have a different - though not contradictory or exclusive - function than local

sensing. Namely, it could function as a system for detecting the global population parameters in such a way that cells can estimate the *likelihood of mating*, so they invest cellular resources accordingly.

1.2 Fractional sensing by signal degradation

1.2.1 Analytical investigation of fractional sensing for a linearly responding pathway

The starting point of our analysis of pheromone communication in sexually reproducing *S. cerevisiae* was the observed response pattern of *MAT**a*** cells in experiments where population parameters were systematically varied, as shown in Figure 3. To monitor the induction of the mating pathway, the P_{FUS1}-GFP transcriptional reporter was used as a readout.

When the total density of cells, ρ_T, is fixed but the composition of the population is varied, increasing the fraction of *MAT*α-cells from 0.1 to 0.9, cells with (3*b*) and without (3*d*) the diffusible peptidase Bar1 (that degrades α-pheromone) show very different patterns. The wild-type (*wt*) cells producing the enzyme exhibit a nearly linear response to the fraction of partner cells. Moreover, at higher total densities, the total density ρ_T loses its effect, with responses at the same θ_α value, but different ρ_T values becoming nearly identical (compare the green and purple lines in panel *b*) of Figure 3).

In other words, we see *density-independent sensing of the fraction of partner cells*, if the total density is above a certain level. In contrast, *bar*1Δ cells are highly sensitive to total cell density. Additionally, at high densities their response is saturated over almost the entire range of θ_α values.

In another experiment (panels *a* and *c*), the control variable was the absolute amount of *MAT*α-cells, ρ_α, which was increased while keeping the fraction of *MAT*α-cells, θ_α, fixed. This means that the number of *MAT**a***-cells was also increased here to keep the population composition constant. The response of *wt* cells to ρ_α, the absolute amount of partner cells, becomes flat after some level, and the response is instead defined by the partner cell fraction (θ_α) again.

In contrast, the response of *bar*1Δ cells essentially follows ρ_α, the absolute amount of partner cells. thus, *bar*1Δ cells are unable to distinguish between situations where the absolute amount of partner cells is identical, but their fraction in the total population is different.

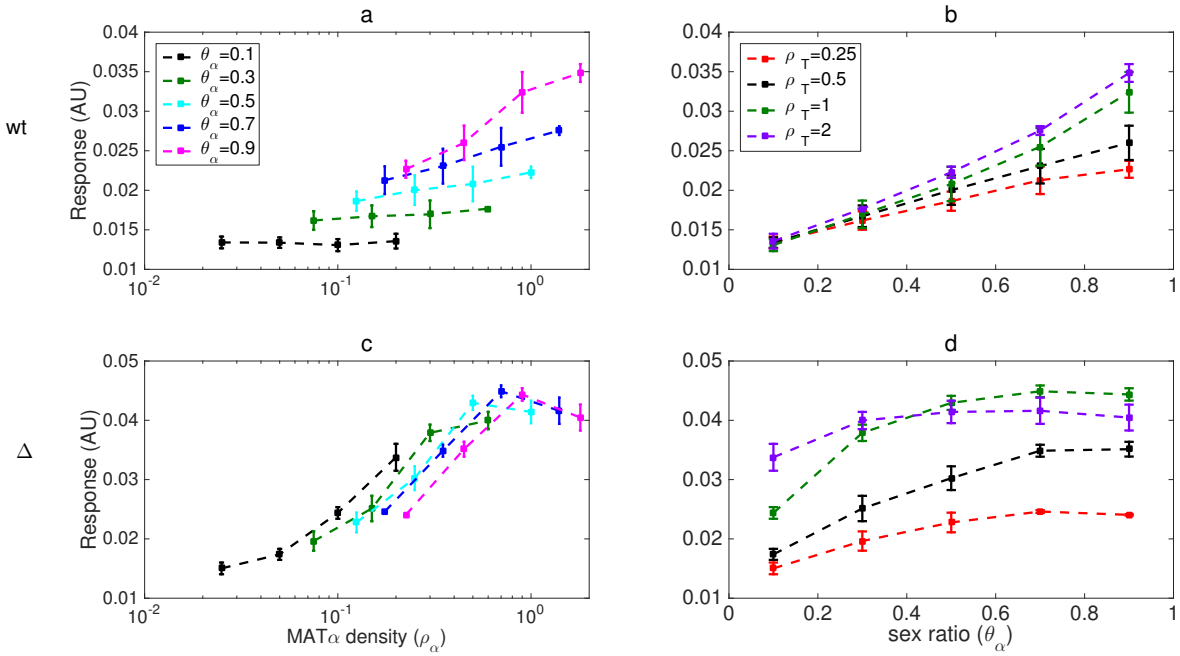

Figure 3. Mean responses of *MATa* cells from mixing experiments. Data is from flow cytometry experiment measuring the P_{FUS1}-GFP transcriptional reporter as a readout, the first row showing the responses of wild-type, the second *bar*1Δ cells. Error bars show standard errors of the mean for three biological replicates. Experiment by Dr Alvaro Banderas.

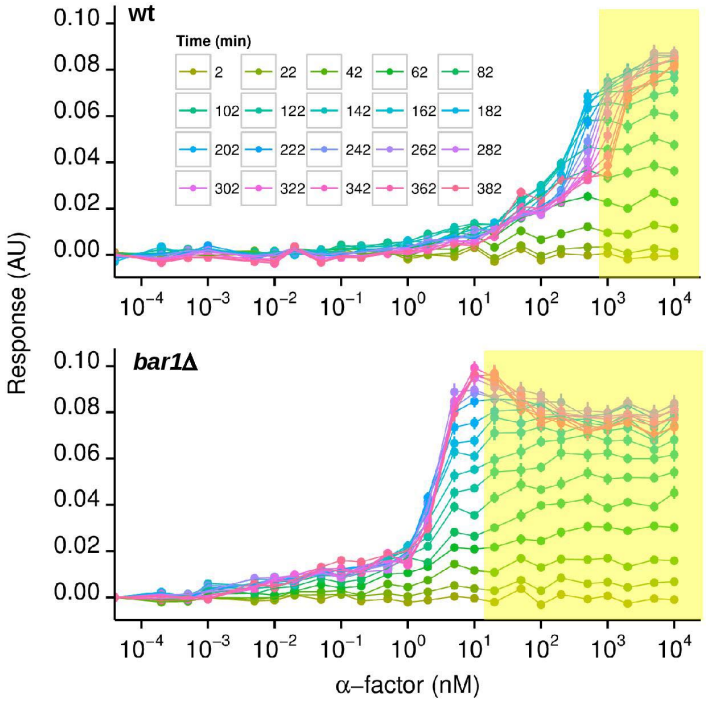

Figure 4. Dynamic response of the P_{FUS1}-GFP reporter to purified α-factor in wild-type and Bar1 knockout (bar1Δ) *MATa* cells. In the wild-type, pathway induction is strongly shifted to the right compared to the bar1Δ strain, showing the signal attenuation effect of Bar1. Experiment and figure by Dr Alvaro Banderas.

These results can be explained by a mathematical model capturing the main features of the pheromone signalling system in a mixed population of yeast cells. In a detailed biochemical study [106] the K_M of the enzyme Bar1 was determined to be 30 μM, which is far higher than the sensitive range of the pheromone response (Figure 4), which is the biologically relevant concentration range. Therefore, instead of a non-linear Michelian term for the rate of degradation, we can use simple first-order kinetics with respect to the substrate, α-pheromone.

I will first write down the equations without any rate constants for simplicity. The concentration dynamics of α-factor and the enzyme Bar1 in a homogeneous mixed population of $MAT\alpha$ and $MAT\boldsymbol{a}$ cells can be described by the following ordinary differential equations (ODE):

$$\frac{d\alpha(t)}{dt} = \rho_\alpha - \alpha(t)b(t) \tag{1}$$

$$\frac{db(t)}{dt} = \rho_a - b(t) \tag{2}$$

Where $\alpha(t)$ and $b(t)$ are the concentrations of α-factor and Bar1, respectively; ρ_α and ρ_a are the number of $MAT\alpha$ and $MAT\boldsymbol{a}$ cells per unit of volume. Using the initial values $\alpha(t=0) = \alpha_0$, $b(t=0) = b_0$, and substituting the solution for Bar1 into Equation 1 we get:

$$\frac{d\alpha(t)}{dt} = \rho_\alpha - \alpha(t)(e^{-t}\,(b_0 - \rho_a) + \rho_a) \tag{3}$$

The analytical solution for the differential equation for $\alpha(t)$ is then:

$$\alpha(t) = \alpha_0 e^{e^{-t}(b_0-\rho_a)+(1-t)\rho_a - b_0} + \rho_\alpha e^{e^{-t}(b_0-\rho_a)-t\rho_a}\left(\int_0^t e^{e^{-z}(\rho_a-b_0)+z\rho_a}\,dz\right) \tag{4}$$

Or, if $\alpha(t=0) = b(t=0) = 0$, this simplifies to:

$$\alpha(t) = \rho_\alpha e^{-\left(t+e^{-t}\right)\rho_a}\int_0^t e^{\left(z+e^{-z}\right)\rho_a}\,dz \tag{5}$$

In the limit of $t >> 1$, the exponents simplify to:

$$\alpha(t) = \rho_\alpha e^{-t\rho_a}\int_0^t e^{z\rho_a}\,dz = \frac{\rho_\alpha\,(1 - e^{-t\rho_a})}{\rho_a} \tag{6}$$

Which for $t >> 1$ converges to the steady state concentration $[\alpha^*]$:

$$\alpha^* = \frac{\rho_\alpha}{\rho_a} \tag{7}$$

That is, the steady-state concentration of the signal, α-pheromone, is exactly the ratio of $MAT\alpha$ to $MAT\boldsymbol{a}$ cells, r_α. Rate constants for production and degradation would simply scale the ratio by a constant (see below).

Our initial observation was a linear dependence of the *cellular response* of wild-type $MAT\boldsymbol{a}$-cells on the *fraction* of $MAT\alpha$-cells, θ_α (Figure 3*b*), and not on the ratio, r_α. The relationship between fraction and ratio is:

$$r_\alpha = \frac{\theta_\alpha}{1-\theta_\alpha} \tag{8}$$

It is however the *cellular response* to the signal (α-pheromone) that scales linearly with θ_α, not the signal strength itself. Converting the signal $[\alpha]$, that scales as $[\alpha] \propto \frac{\theta_\alpha}{1-\theta_\alpha}$, to a response that scales linearly with θ_α can be achieved by the classical saturation curve that many signaling pathways follow (note that the EC_{50} is set to 1 here):

$$response \propto \frac{[\alpha]}{[\alpha]+1} \propto \frac{r_\alpha}{r_\alpha+1} = \frac{\frac{\theta_\alpha}{1-\theta_\alpha}}{\frac{\theta_\alpha}{1-\theta_\alpha}+1} = \theta_\alpha \tag{9}$$

So far I have established two basic features of this system. First, the simple signaling system that yeast cells use, in which the recipient ($MAT\boldsymbol{a}$) cells produce an enzyme that degrades the signal of their partner ($MAT\alpha$) cells, makes the steady state signal scale as the *ratio* of emitter to recipient cells, if the enzyme operates (far) below saturation, so the rate of degradation is linear with the substrate. Second, if the readout of this signal by recipient cells is through a signaling pathway with a saturating dose response curve, this leads to a response that is a linear function of the $fraction$ of partner (emitter) cells within the total population, in our case θ_α.

Going into more detail, we have to consider the fact that Bar1 is very stable on the timescale of mating and is not degraded to any substantial extent by the time that the steady state response patterns emerge (Figure 3, responses plotted at t=140min). We can investigate the effect of Bar1's stability by assigning a rate constant k to the first-order degradation (or any kind of loss) of the enzyme itself, so that the ODE for Bar1, Equation 2, is:

$$\frac{db(t)}{dt} = \rho_a - k\ b(t) \tag{10}$$

and the equation for α-factor dynamics, with the analytical solution of Bar1 substituted in, is:

$$\frac{d\alpha(t)}{dt} = \rho_\alpha - \alpha(t)\frac{\rho_a\left(1-e^{-kt}\right)}{k} \tag{11}$$

The solution for $\alpha(t)$ is then (using again the initial values $\alpha(t=0) = b(t=0) = 0$):

$$\alpha(t) = \rho_\alpha e^{-\frac{\rho_a\left(kt+e^{-kt}\right)}{k^2}} \int_0^t e^{\frac{\rho_a\left(kz+e^{-kz}\right)}{k^2}} dz \tag{12}$$

Which in the limit of $t >> 1$ is:

$$\alpha(t >> 1) = \rho_\alpha e^{-\frac{t\rho_a}{k}} \int_0^t e^{\frac{z\rho_a}{k}} dz = k\frac{\rho_\alpha}{\rho_a}\left(1 - e^{-\frac{t\rho_a}{k}}\right) \tag{13}$$

So that the steady state is:

$$\alpha^* = k\frac{\rho_\alpha}{\rho_a} \tag{14}$$

While the steady state concentration of α is only a function of the ratio (r_α) and the rate constant of the loss of Bar1 (k), in the dynamics there are differences as a function of total density ρ_T as well, as shown in Figure 5.

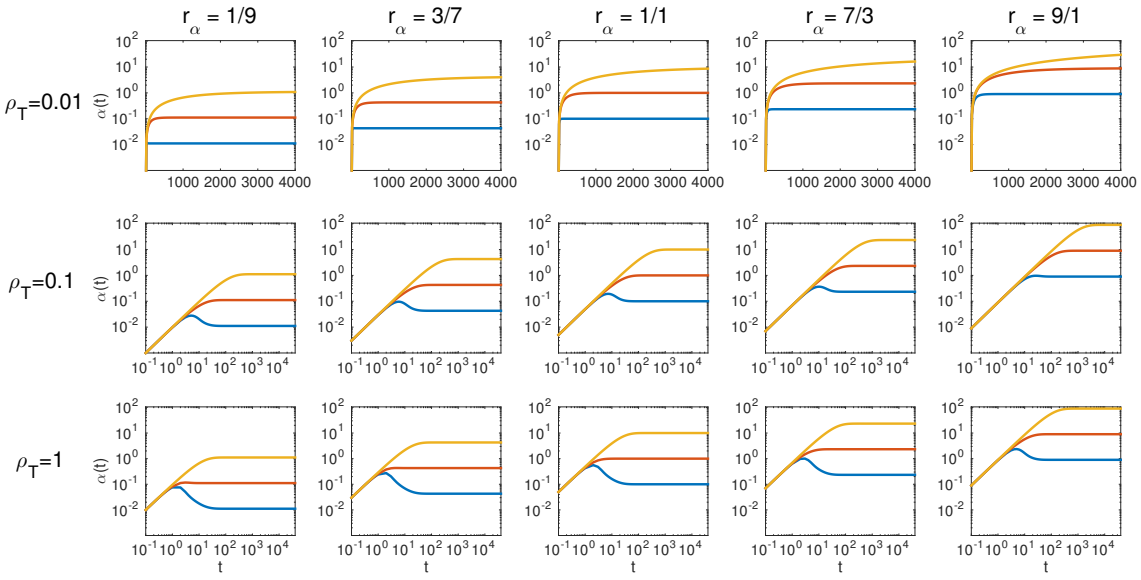

Figure 5. Dynamics of α-pheromone as a function of population parameters and the stability of Bar1. Analytical solution of α-pheromone dynamics from Equation 12. The x axis (time) is logarithmic in the lower two rows to show the peaking behavior. The different colors stand for different values of Bar1's degradation rate constant, $k = 0.1$ (blue), $k = 1$ (red), $k = 10$ (orange).

These dependencies are analyzed in Figure 6. As we know from Equations 12-14, the steady state itself is independent of ρ_T, shown in Figure 6*a*. The time required to get to 90% of a given steady state value (Figure 6*b*) decreases with higher total cell densities, ρ_T. Finally, if Bar1 is stable, the dynamics of α-pheromone is non-monotonic, with the peak value a function of both the ratio (r_α) and, with a weaker dependence, total cell density (ρ_T), as shown in Figure 6*c*.

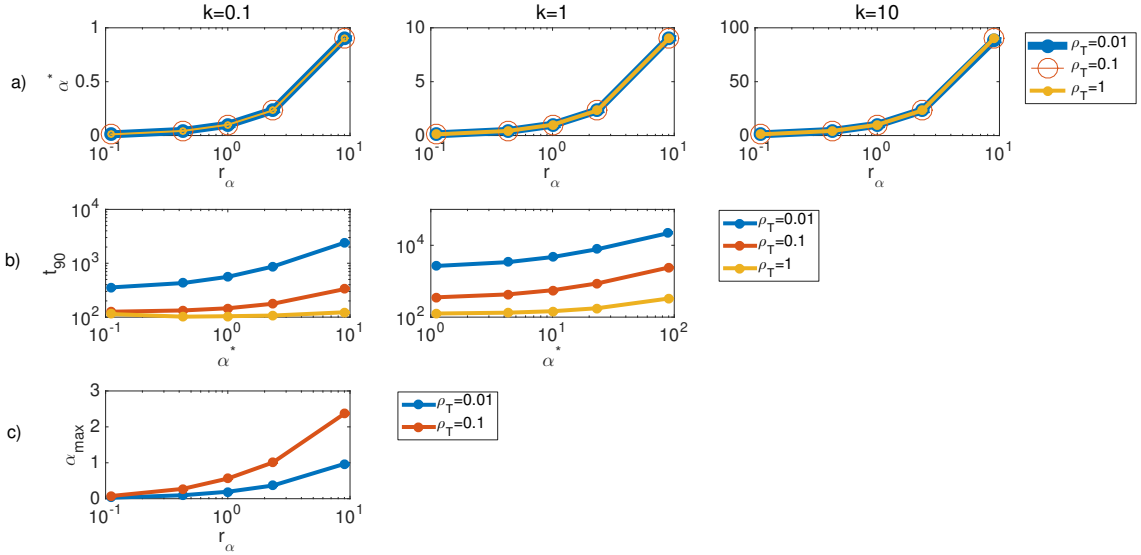

Figure 6. Key properties of α-pheromone dynamics as a function of population parameters and the stability of Bar1. The first row shows the steady state α-pheromone concentrations at different values of Bar1's degradation constant, k. The second row shows the time required to reach 90% of the steady state values (x axis). The third row shows the peak value of α-pheromone, at the lowest value of k, where the dynamics shows non-monotonic behavior.

In the limiting case of no Bar1 degradation at all, the analytical solution for $\alpha(t)$ becomes:

$$\alpha(t) = \frac{\rho_\alpha}{\sqrt{\rho_a}}\sqrt{\frac{\pi}{2}}\ erfi\left(t\sqrt{\frac{\rho_a}{2}})\right)\ exp\left(-\left(t\sqrt{\frac{\rho_a}{2}}\right)^2\right) \tag{15}$$

$\frac{\sqrt{\pi}}{2}exp(-x^2)erfi(x) = exp(-x^2)\int_0^x exp(t^2)dt$ is the so-callad Dawson integral $F(x)$, therefore we can also re-write the equation as

$$\alpha(t) = \frac{\rho_\alpha}{\sqrt{\rho_a}}\sqrt{2}F\left(\sqrt{\frac{\rho_a}{2}}t\right) \tag{16}$$

The Dawson integral $F(x)$ has a maximum at $F'(x) = 0$, or $1 - \sqrt{\pi}\ exp(-x^2)\ x\ erfi(x) = 0$, numerically at $F(0.9241) = 0.541$. In our case, with $F\left(\sqrt{\frac{\rho_a}{2}}t\right)$, the value of t where $\alpha(t)$ reaches its maximum scales as $\frac{1.30693}{\sqrt{\rho_a}}$.

I analyze three properties of the α-pheromone dynamics: the maximal concentration that the pheromone reaches (α_{max}), the time to reach the maximum (t_{max}) and the integral of the pheromone concentration up to the timepoint it falls back to 10% of its peak value.

A mixed population can be defined with two population parameters, either by ρ_a and ρ_α, or ρ_T and θ_α (or r_α). I look at how these three measures of the signal dynamics depend on either the densitities of the two cell types (ρ_a and ρ_α), or of the total cell density ρ_T and the composition of the population, defined by r_α or θ_α.

The maximal concentration reached by alpha pheromone is algebraically defined as

$$\alpha_{max} = max\left(\frac{\rho_\alpha}{\sqrt{\rho_a}}\sqrt{2}F\left(\sqrt{\frac{\rho_a}{2}}t\right)\right) = max\left(\frac{\rho_\alpha}{\sqrt{\rho_a}}\sqrt{2}F\left(t\right)\right) = \sqrt{2}\ 0.541\frac{\rho_\alpha}{\sqrt{\rho_a}} = 0.767\frac{\rho_\alpha}{\sqrt{\rho_a}} \quad (17)$$

Which can be rewritten as:

$$0.767\frac{\rho_\alpha}{\sqrt{\rho_a}} = 0.767\sqrt{\rho_T}\frac{\theta_\alpha}{\sqrt{1-\theta_\alpha}} = 0.767\sqrt{\rho_T}\frac{r_\alpha}{\sqrt{1+r_\alpha}} \quad (18)$$

The linear scaling of α_{max} with $\frac{\theta_\alpha}{\sqrt{1-\theta_\alpha}}$ and $\sqrt{\rho_T}$, is shown in panel 3 of the first and second rows of Figure 8, respectively. The time to reach the maximal concentration only depends on the density of recipient cells, that is:

$$t_{max} = \frac{1.30693}{\sqrt{\rho_a}} = \frac{1.30693}{\sqrt{(1-\theta_\alpha)\rho_T}} = 1.30693\sqrt{\frac{1+r_\alpha}{\rho_T}} \quad (19)$$

shown in the panels 1 (first and second rows) of Figure 8.

We can see that the maximal α-pheromone concentration and the time point it is reached has an inverse dependence on the total density ρ_T: $t_{max} \propto \frac{1}{\sqrt{\rho_T}}$, $\alpha_{max} \propto \sqrt{\rho_T}$.

If we take the integral of the α-pheromone dynamics from 0 to a time point where $\alpha(t)$ falls back to a given (smaller or equal to 100%) percentage of the maximal α-pheromone value, we find that this measure is *invariant* of ρ_T, as shown in panels 4 and 5 of the second row of Figure 8. This is due to the mathematical properties of the function $\alpha(t)$. At a constant fraction θ_α we can rewrite the equation $\alpha(t) = \sqrt{\rho_T}\frac{\theta\alpha}{\sqrt{1-\theta_\alpha}}\sqrt{2}F\left(\sqrt{\frac{\rho_T(1-\theta_\alpha)}{2}}t\right)$ as

$$\alpha(t) \propto \sqrt{\rho_T}\ exp(-(\sqrt{\rho_T}t)^2)\ erfi(\sqrt{\rho_T}t) \quad (20)$$

the other terms omitted being constants. The time point of the maximum concentration reached, t_{max}, scales as $t_{max} \propto \frac{0.924139}{\sqrt{\rho_T}}$. Similarly, the timepoint t_c ($t_c \geq t_{max}$) the pheromone concentration falls back to a fraction c ($0 < c \leq 1$) of its peak concentration α_{max} also scales as $t_c \propto \frac{1}{\sqrt{\rho_T}}$.

To take a concrete example, in the case of $c = 0.1$, $t_{0.1} = \frac{9.29582}{\sqrt{\rho_T}}$.

Integrating the α-pheromone concentration up to the point t_c we get:

$$\int_0^{\frac{\tau}{\sqrt{\rho_T}}} \sqrt{\rho_T}\ \mathrm{erfi}(\sqrt{\rho_T}t)\exp\left(-(\sqrt{\rho_T}t)^2\right)\ dt = \frac{\tau^2\ {}_2F_2\left(1,1;\frac{3}{2},2;-\tau^2\right)}{\sqrt{\pi}} \quad (21)$$

This definite integral is *independent* of total density $\sqrt{\rho_T}$. ${}_2F_2$ is the generalized hypergeometric

function. In the integration limit, τ is a constant that depends on what percentage of the peak concentration we define for the α-pheromone concentration to fall back, for example for 10%, it is $\tau = 9.29582$.

Calculations of $\alpha(t)$ with two values of ρ_T and their integrals from $t = 0$ to $\alpha(t_{0.1}) = 0.1\alpha_{max}$ ($t_{0.1} > t_{max}$) are shown in Figure 7.

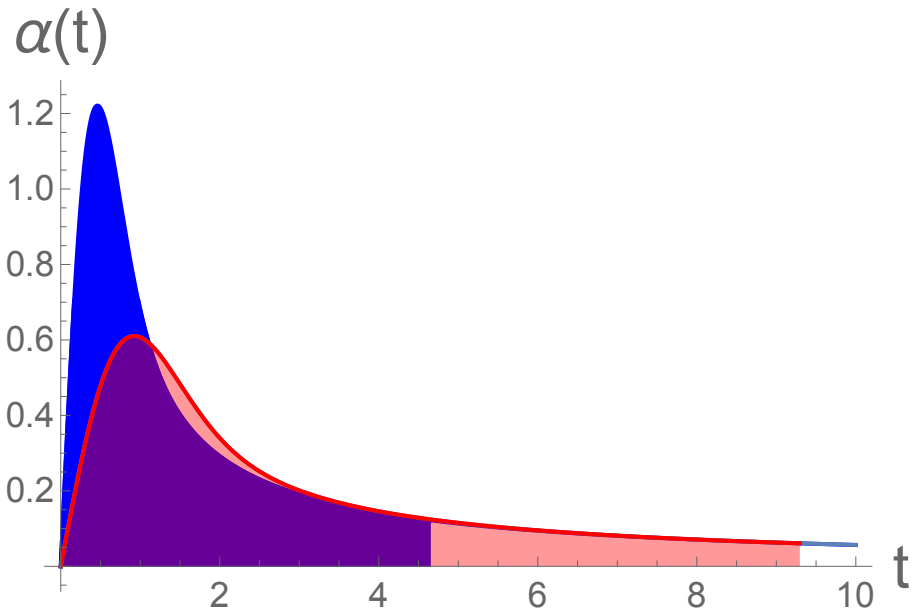

Figure 7. α-pheromone dynamics at two different ρ_T values, with the ratio r_α fixed, when Bar1 is stable. The shaded areas show the definite integral of the pheromone concentrations from $t = 0$ to the time point $t_{0.1}$ when $\alpha(t_{0.1}) = c\ \alpha_{max}$ ($t_{0.1} > t_{max}, c = 0.1$). This measure is invariant of ρ_T for any value of $0 < c \leq 1$.

To turn to the effect of the partner cell fraction, θ_α, we can see that at a fixed total density $\alpha(t)$ scales with θ_α as:

$$\alpha(t) \propto \frac{\theta_\alpha}{\sqrt{1-\theta_\alpha}} F\left(t\sqrt{1-\theta_\alpha}\right) \tag{22}$$

Again, the timepoint t_c ($t_c \geq t_{max}$) where the pheromone concentration falls back to a fraction c ($0 < c \leq 1$) of its peak concentration α_{max} scales as $t_c \propto \frac{1}{\sqrt{1-\theta_\alpha}}$, as shown in Figure 8 (first row, panels 1 and 2). If we look at the dependence of this integral on the fraction θ_α we get:

$$\int_0^{\frac{\tau}{\sqrt{1-\theta_\alpha}}} \frac{\theta_\alpha}{\sqrt{1-\theta_\alpha}} F\left(t\sqrt{1-\theta_\alpha}\right) dt = \frac{\theta_\alpha}{1-\theta_\alpha} \frac{\tau^2\, {}_2F_2\left(1,1;\frac{3}{2},2;-\tau^2\right)}{2} = r_\alpha \frac{\tau^2\, {}_2F_2\left(1,1;\frac{3}{2},2;-\tau^2\right)}{2} \tag{23}$$

${}_2F_2$ is the generalized hypergeometric function. That is, the integral of $\alpha(t)$ from $t = 0$ until the timepoint t_c, where $\alpha(t)$ falls back to a defined fraction of α_{max} scales linearly with the ratio of $MAT\alpha$ to $MAT\mathbf{a}$ cells, r_α, as shown in Figure 8 (first row, panels 4 and 5).

To summarize, in a simple production-degradation system with two cell types, where the signal produced by one cell type ($MAT\alpha$) is detected by the other ($MAT\mathbf{a}$), while also being degraded by a stable enzyme secreted by recipient cells, the *integral of the signal molecule concentration up to its maximal value, or the timepoint where it falls back to a defined level of its maximum, is independent of the total density of cells and scales linearly with the ratio of emitter to recipient cells.* The signaling dynamics of this system is therefore eminently capable of robustly carrying information of the *relative* abundance of partner cells at different total densities of the population.

Next, I investigated how the *cellular response* behaves as a function of the stimulation (α-pheromone dynamics). We know from dose-response experiments with purified α-factor that pathway induction is, in some (lower) range of the input concentration $[\alpha]$, roughly linear with $[\alpha]$. I first investigate pathway behavior in this linear range to make it more tractable mathematically. In this case, the ordinary differential equation for the pathway output (P_{FUS1}-GFP, denoted as $GFP(t)$ in mathematical expressions) is:

$$\frac{dGFP(t)}{dt} = \alpha(t) - k_{deg}GFP(t) = \frac{\theta_\alpha}{\sqrt{1-\theta_\alpha}}\sqrt{\rho_T}\sqrt{2}F\left(\sqrt{\frac{\rho_T(1-\theta_\alpha)}{2}}\ t\right) - k_{deg}GFP(t) \qquad (24)$$

with F being the Dawson-integral. We want to see how the GFP-dynamic depends on the population parameters θ_α and ρ_T, respectively.

In the case of a constant fraction θ_α, $GFP(t)$ scales with ρ_T as (also neglecting the degradation rate constant k_{deg}):

$$\frac{dGFP(t)}{dt} \propto \sqrt{\rho_T}F\left(\sqrt{\rho_T}t\right) - GFP(t) \qquad (25)$$

The analytical solution (for the initial condition $GFP(t) = 0$) is then, as a function of ρ_T (and time):

$$GFP(t) \propto e^{-t}\int_0^t e^z\ \sqrt{\rho_T}F(\sqrt{\rho_T}z)\,dz \qquad (26)$$

and with the fraction, θ_α:

$$GFP(t) \propto e^{-t}\int_0^t e^z\ \frac{\theta_\alpha}{\sqrt{1-\theta_\alpha}}F\left(\sqrt{1-\theta_\alpha}\ z\right)\,dz \qquad (27)$$

We cannot integrate this function in closed form like for the signal dynamics, but by numerical calculations we can investigate the same dynamical properties as for α-factor, as a function of the two population parameters, θ_α and ρ_T.

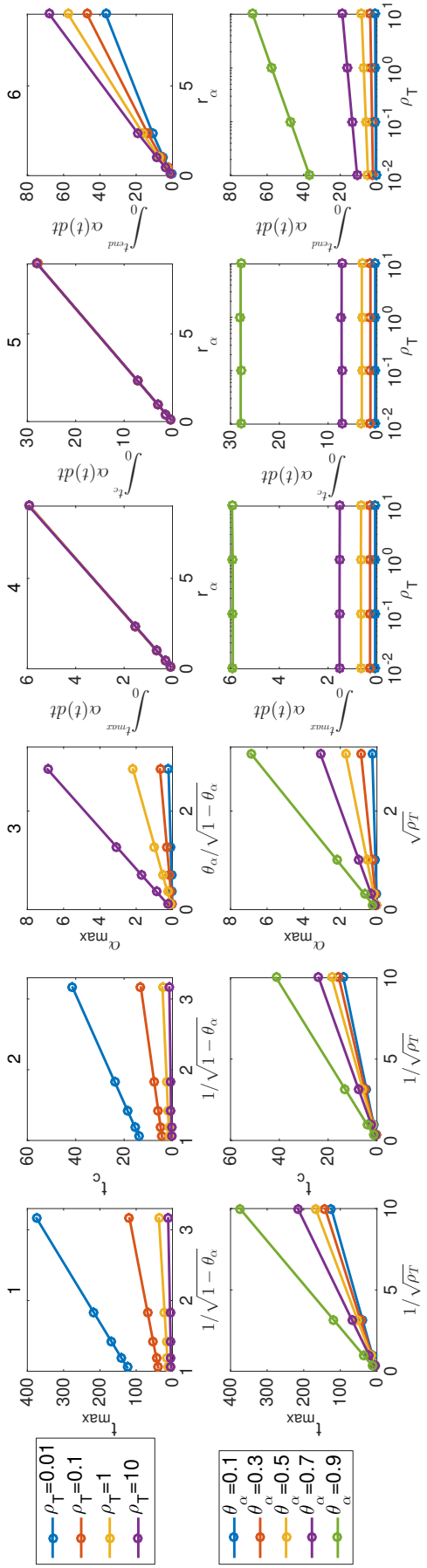

Figure 8. Dynamical properties of α-factor as a function of partner cell fraction θ_α and total cell densityρ_T. t_c is the timepoint that $\alpha(t)$ falls back to 10% of its maximal concentration α_{max}. The last panel shows the integral up to the latest timepoint, t_{end}, which is $t = 10^4$ in these calculations. All trajectories are at a value smaller than 5% of their previous maxima.

I performed numerical calculations at three different values of the degradation rate constant of GFP, k_{deg} (10^{-3}, 10^{-2}, 10^{-1}, 10^{0}), to see the effect of the separation of the timescales of signal and pathway dynamics. The scaling properties of GFP with θ_α and ρ_T are shown in Figures 9 and 10, respectively.

When $k_{deg} = 1$ and pathway output tracks signal dynamics closely, its scaling properties with the population parameters are nearly identical to those of signal dynamics $\alpha(t)$. The integral under the GFP curve can be regarded as the cumulative transcriptional output [101].

The integral up to t_{max}, the timepoint of the maximal pathway output GFP_{max}, scales linearly with the ratio r_α ($= \frac{\theta_\alpha}{1-\theta_\alpha}$), as shown in the fourth and fifth panels of the first row in Figure 9. This measure, the integral of pathway output, is nearly independent of ρ_T (fourth and fifth panels of the first row in Figure 10).

If k_{deg} is lower, making pathway dynamics slower, the integrals $\int_0^{t_{max}} GFP(t)dt$ and $\int_0^{t_c} GFP(t)dt$ start to show some density dependence, which can be seen in the fourth and fifth columns of Figure 9 and 10, as we move downward. When integrating the different (in terms of the input population parameter θ_α and ρ_T) trajectories to the same absolute timepoint ($t = 10^4$ on the plot), we see the same pattern as with $\alpha(t)$ (compare Figure 8 panel 6 in the first row), namely, a linear dependence with r_α and a much weaker linear dependence on the *logarithm* of ρ_T.

In summary, in the linear range (of pathway induction) pathway dynamics scale nearly identically with signal dynamics with regard to the population parameters θ_α and ρ_T. Specifically, the integral under the curve up to its maximal value, GFP_{max}, or to a given fraction of the maximum at a later timepoint scales linearly with r_α, the ratio of emitter to recipient cells, while being largely independent of the total density of cells, ρ_T.

In other words, the cumulative pathway output reflects the fraction of partner cells as well, showing that the signaling system we have in yeast is robustly 'designed' for fractional sensing. In the next section I use a more detailed non-linear model to explain the experimental results directly.

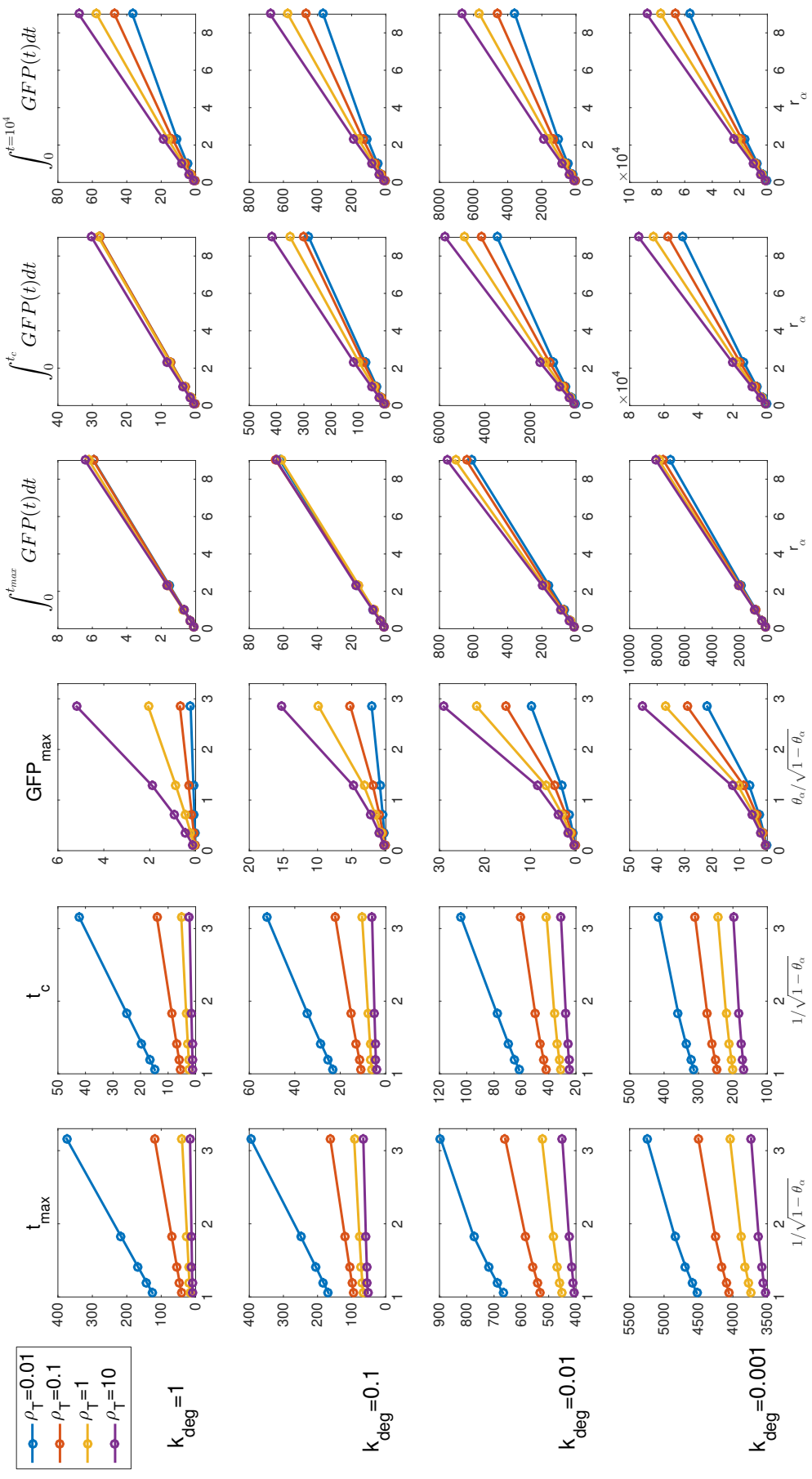

Figure 9. Different dynamical properties of GFP dynamics, as a function of the partner cell fraction θ_α, at different values of the rate constant for GFP degradation, k_{degr} (rows). At each θ_α, the calculation was performed for four different values of the total cell density ρ_T (different colors).

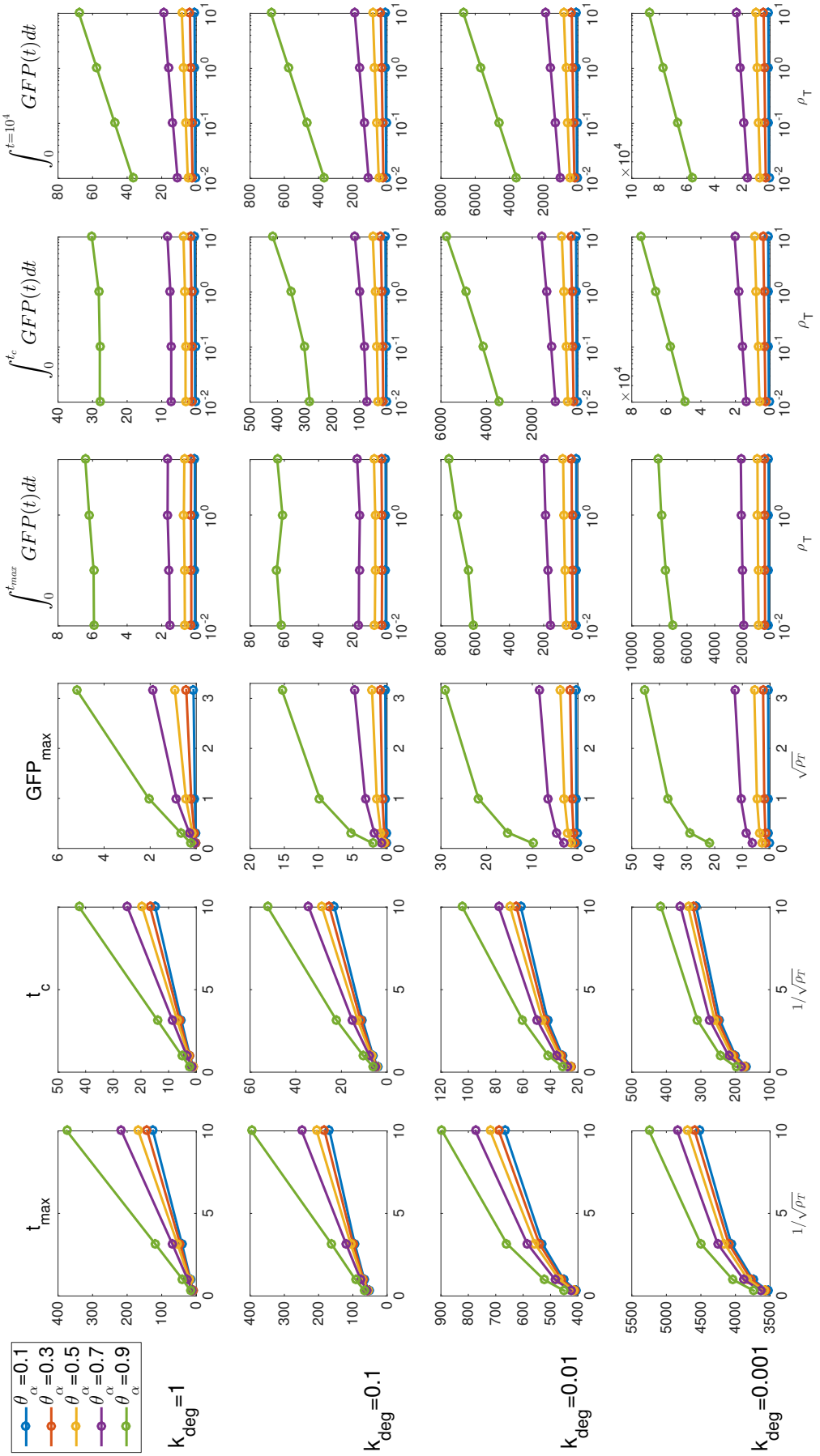

Figure 10. Different dynamical properties of GFP dynamics (columns), as a function of total cell density ρ_T, at different values of the rate constant for GFP degradation, k_{degr} (rows).

1.2.2 Parameter fitting of the non-linear pathway model

I. Basic model: constant production rate of pheromones

The experimental data in Figure 3 showed an approximately linear response (level of pathway induction at a given timepoint) to partner cell fraction θ_α, whereas in the previous subchapter 1.2.1 the cumulative output scaled linearly with the *ratio* $r_\alpha = \theta_\alpha/(1-\theta_\alpha)$. As shown in Equations 8-9, a signal scaling linearly with r_α can be converted to a response scaling linearly with θ_α by a saturating pathway profile. We know from our experimental data, shown in Figure 4, that the mating pathway response indeed saturates with α-factor concentration. In the previous section 1.2.1 I investigated the properties of the pathway response in the linear range to highlight its fundamental properties as clearly as possible

To capture the non-linearity in the pathway response, I used a standard saturation curve [125] for the production rate of our reporter P_{FUS1}-GFP. I did not model the molecular details of the mating pathway. I am primarily interested in the input-output relation of the system (what we also have empirically, shown on Figure 4), not the intra-pathway molecular events. Therefore I used a model that directly connects the output to the level of stimulation detected by the receptors, $\alpha(t)$:

$$\frac{dGFP(t)}{dt} = V_0 + V_{max}\frac{\alpha(t)^H}{\alpha(t)^H + EC_{50}^H} - \delta_{GFP}GFP(t) \tag{28}$$

V_0 is the basal production rate, V_{max} the maximal production rate, H is a Hill-coefficient for response cooperativity, EC_{50} the level of stimulation that produces a half-maximal production rate and δ_{GFP} the rate constant for the first-order degradation/dilution of GFP. This equation cannot be solved analytically, and my aim instead was fitting its parameters to explain the experimental results.

The concentration dynamics of α-factor and the enzyme Bar1 in a homogeneous mixed population of $MAT\alpha$ and $MAT\mathbf{a}$ cells can be described by the following ordinary differential equations:

$$\frac{d\alpha(t)}{dt} = \rho_\alpha\nu_1 - \kappa\ \alpha(t)b(t) - k_{deg}^\alpha\alpha(t) \tag{29}$$

$$\frac{db(t)}{dt} = \rho_a\nu_2 - k_{deg}^b b(t) \tag{30}$$

where $\alpha(t)$ and $b(t)$ are the concentrations of α-factor and Bar1, respectively; ρ_α and ρ_a are the number of $MAT\alpha$ and $MAT\mathbf{a}$ cells per unit of volume; ν_1 and ν_2 are per cell production rates of α-factor and Bar1, respectively; and κ is the rate constant of Bar1-dependent α-factor

degradation. The enzymatic α-factor degradation has linear kinetics (no saturation) here, which is justified because the K_M of Bar1(30 μM) is much higher [106] than the concentrations within the sensitive range of the pheromone response. I further neglected spontaneous degradation of Bar1 and of α-factor, as both are negligible on the time-scale of the experiment. This simplifies the two equations above to

$$\frac{d\alpha(t)}{dt} = \rho_\alpha \nu_1 - \kappa\ \alpha(t) b(t) \tag{31}$$

$$\frac{db(t)}{dt} = \rho_a \nu_2 \tag{32}$$

The system of Equations 31 and 32 has the exact solution, for the initial conditions $b(t=0) = 0, \alpha(t=0) = 0$:

$$\alpha(t) = c_1 \frac{\rho_\alpha}{\sqrt{\rho_a}} exp\left(-(t\ c_2)^2\right) erfi(t\ c_2) \tag{33}$$

where $c_1 = 1.253\ \nu_2 \frac{1}{\kappa\ \nu_2}$, $c_2 = 0.707\sqrt{\kappa\ \nu_2\ \rho_a}$ and $erfi$ is the imaginary error function.

As discussed in the previous section, the solution has non-monotonic time dependence, falling to zero after reaching a maximum $\alpha_{max} = c\frac{\rho_\alpha}{\sqrt{\rho_a}}$, where c is a combination of kinetic constants, $c = 1.253\nu_1\sqrt{\frac{1}{\kappa\ \nu_2}}0.6105$ (irrespective of the value of c_2).

The ODE for GFP was already described above, in Equation 28. When fitting the model, some of the parameters were fixed or constrained by experimental data:

- δ_{GFP} is the parameter for first-order GFP degradation (and dilution), experimentally estimated as $\delta_{GFP} \approx 0.02/min$ (unpublished data, Alvaro Banderas). This parameter is allowed to vary in a narrow range [0.01; 0.03] around the experimentally determined value.

- The EC_{50} value is fixed to $2nM$, derived from the experimentally measured dose-dependence of reporter induction upon stimulation with synthetic α-factor (Figure 4).

- The value of the Hill-coefficient, H, was allowed to vary between 1 and 3 because of the mild sigmoidality observed in dose-response experiments (Figure 4).

- The maximal GFP production rate V_{max} and the basal rate V_0 are allowed to vary within $10^{-4} \leq V_{max} \leq 10^{-3}(AU/min)$. The ratio $(V_0 + V_{max})/\delta_{GFP}$ is fixed to the maximal (steady state) fluorescence value measured in flow cytometry (0.044 AU).

- The parameters ν_1 and the product $\nu_2\kappa$ (Equations 31 - 32) are allowed to vary within the constraints $10^{-9} \leq \nu_1 \leq 10^{-5}$ (pmol/min) and $10^{-16} \leq \nu_2\kappa \leq 10^{-10}$ (L/min^2), respectively.

The objective function to be minimized to fit these parameters is the weighted sum of squared residuals between the data points (GFP^{data}, mean of the 3 replicas of the mixed cells experiments) and the model outputs (GFP^{mod}), normalized by the value of data points, fitting the model predictions simultaneously to the wt and $bar1\Delta$ responses:

$$F = \sum_{i=1}^{M}\sum_{j=1}^{N}\sum_{k=1}^{K}\left(\frac{GFP_{WT}^{data}(\theta_i,\rho_j,t_k) - GFP_{WT}^{mod}(\theta_i,\rho_j,t_k)}{GFP_{WT}^{data}(\theta_i,\rho_j,t_k)}\right)^2 + \left(\frac{GFP_{bar1\Delta}^{data}(\theta_i,\rho_j,t_k) - GFP_{bar1\Delta}^{mod}(\theta_i,\rho_j,t_k)}{GFP_{bar1\Delta}^{data}(\theta_i,\rho_j,t_k)}\right)^2 \tag{34}$$

$F = 1.1675$.

Normalizing by the standard deviation of the responses leads to a fit dominated by a few datapoints, since the standard deviation is in some cases very small.

The parameter values are from fitting to a total of 80 GFP values from flow cytometry experiments, as we fit the model to 20 pairs of values of the input parameters θ_α and ρ_T at two timepoints ($t = 135min$ and $t = 195min$) and to two samples (wild-type and $bar1\Delta$).

The parameter values we obtained are the following: ν_1 = 1e-08 pmol/min; $\nu_2\kappa$ = 1.14e-13 L/min^2; δ_{GFP} = 0.03/min, V_0 = 4.04e-04 AU/min, V_{max} = 9.39e-04 AU/min, H = 1.24. In Equation 34, M is equal to the number of θ_α values, N to the number of ρ_T values and K the number of timepoints, M=5, N=4, K=2. Fitting was performed by the local search algorithm $fmincon$ of $MATLAB$ sampling over initial values within the allowed range of values for all fit parameters.

The fit at $t = 195min$ shown in Figure 12 becomes poorer, as feedback effects within the mating pathway start to reshape the response in ways not explained by our minimal pathway model.

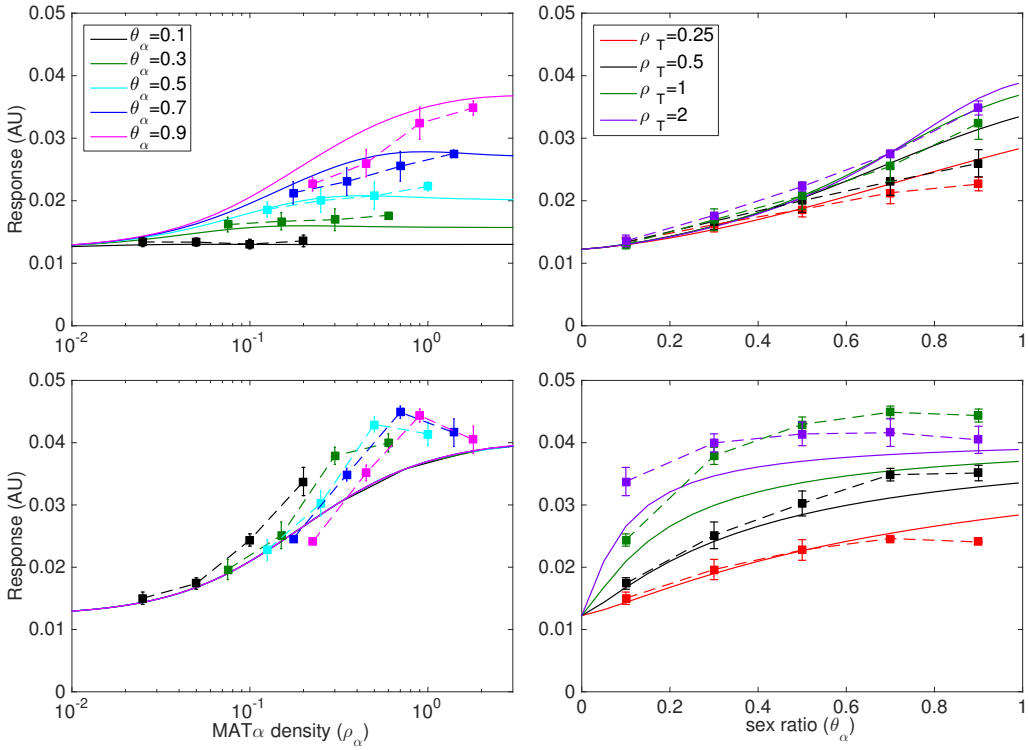

Figure 11. Mean responses in mixing experiments (squares) at t=135min, with error bars showing standard errors of the mean (SEM) for three biological replicates. Solid lines show fits to the data using the computational model of the mating pathway response. First row shows wild type responses, the second $bar1\Delta$. First row shows wild-type responses, second $bar1\Delta$.

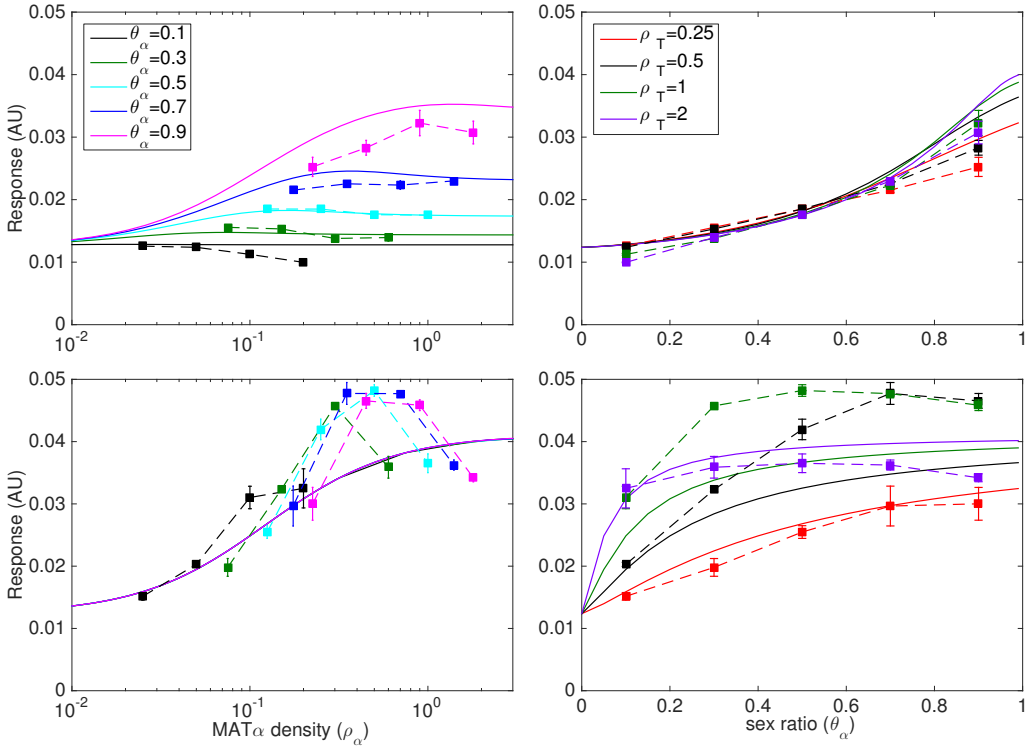

Figure 12. Mean responses in mixing experiments (squares) at t=195 min. First row shows wild-type responses, second $bar1\Delta$.

II. Model with mutual pheromone induction

One important property of the system that is not included in the basic model above is the fact that pheromone production by the cells is not constant, but inducible [107, 142]. Therefore, stimulation of $MAT\mathbf{a}$ cells by α-factor induces production of a-factor and *vice versa*. I described this induction with a deterministic model:

rate of pheromone production $\propto \nu \left(1 + \Phi \frac{\alpha(t)^{H_{MF}}}{\alpha(t)^{H_{MF}} + EC_{50}^{H_{MF}}}\right)$.

For simplicity and lack of the relevant parameters from experiments or the literature, I assumed that pheromone induction has similar dose-dependence as $P_{Fus1} - GFP$.

I therefore fixed the EC_{50} of pheromone induction to 2 nM, but let its Hill coefficient (H_{MF}), fold-change parameter (Φ) and the basal production rate (ν) vary. For simplicity, I also assumed that a- and α-factor induction follow identical dependence, except for the absolute level of ν (ν_1: α-factor basal production rate, ν_3: a-factor basal production rate).

The dynamics of the α- and a-factor induction can then be described as

$$\frac{d\alpha(t)}{dt} = \nu_1 \left(1 + \Phi \frac{a(t)^{H_{MF}}}{a(t)^{H_{MF}} + EC_{50}^{H_{MF}}}\right) - \kappa\alpha(t)b(t) \tag{35}$$

and

$$\frac{da(t)}{dt} = \nu_3 \left(1 + \Phi \frac{\alpha(t)^{H_{MF}}}{\alpha(t)^{H_{MF}} + EC_{50}^{H_{MF}}}\right) - k_{deg}^{a} a(t) \tag{36}$$

Since we focus on the early time points of the response, I further neglected spontaneous degradation of the a-factor (k_{deg}^{a}). The equations describing other variables (Bar1, GFP) are the same as above (Equations 31 and 32).

The resulting fit yields the parameter values: ν_1 = 5.3-09 pmol/min; $\nu_2\kappa$ = 1.3e-13 L/min^2; δ_{GFP} = 0.034/min, V_0 = 4.4e-04, $Vmax$ = 1e-03, H_{GFP} = 1.41, ν_3 = 2.96e-08 pmol/min, H_{MF} = 1.46, Φ = 1.36. This model produced only marginally better fits, at the cost of four further free parameters. The fits are shown in Figure 13.

One qualitative feature of the response that this model reproduces is the negative dependence of the $bar1\Delta$ responses on θ_α when they are plotted as a function of ρ_α. These curves are separate and the ones at higher θ_α values are to the left of those with lower θ_α values. To see whether this is indeed due to mutual pheromone induction would require experiments removing the mutual feedback.

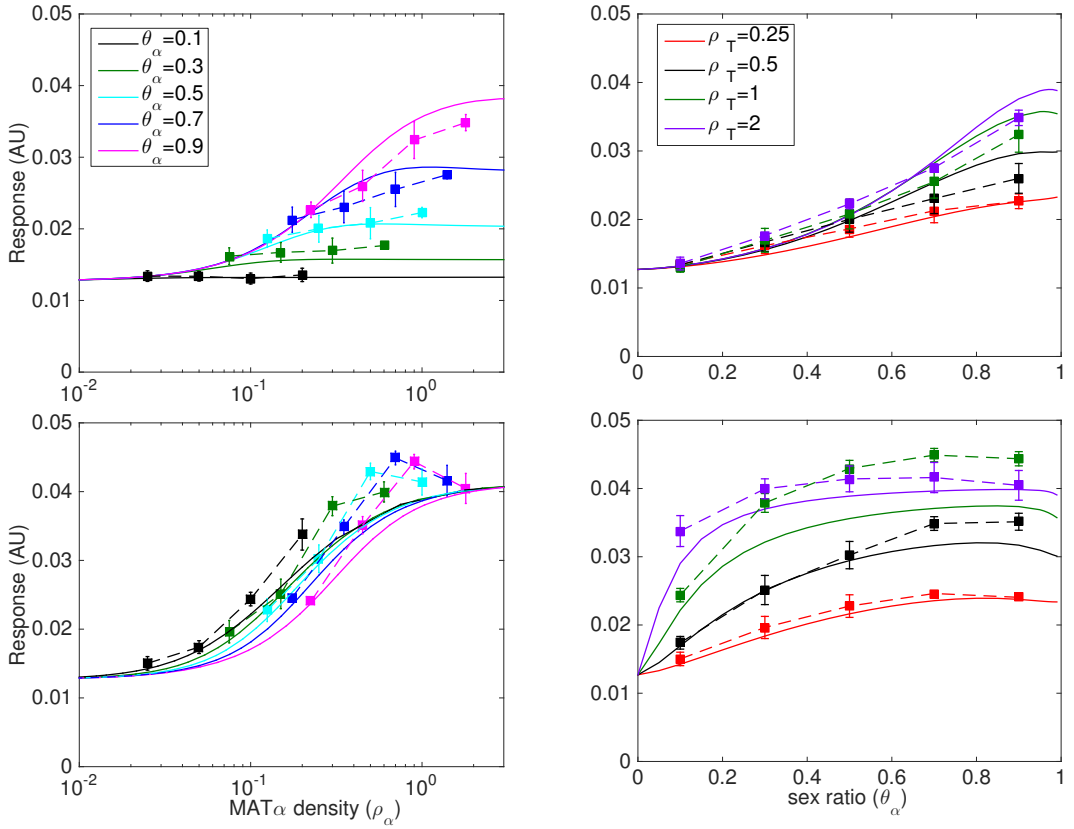

Figure 13. Mean responses in mixing experiments (squares) at t=135 min, with error bars showing standard errors of the mean (SEM) for three biological replicates. Solid lines show fits to the data using the computational model including mutual induction of pheromone production (Model II). First row shows wild type responses, the second *bar*1Δ.

In the previous section 1.2.1, I showed that the time integral of the signal (pheromone) concentration is a function of the fraction of partner cells (θ_α) only, completely independent of the total density of cells. Moreover, I also showed that in the case of a linear pathway, the integral of the pathway output, which is a measure of resource investment by the cell, behaves nearly identically, that is, it is primarily a function of the partner cell fraction and depends only very weakly on the absolute density of cells. The experimental data I used does not have the sufficient time resolution to calculate the time integral. Instead, I constructed a more detailed, non-linear pathway model to reproduce the responses at given time points.

In summary, we can see that signal degradation coupled with a non-linear, saturating signaling pathway produces the behavior observed in the experiments. Namely, for wild-type cells we see a linear response to the fraction of partner cells (θ_α) with a weak dependence on the total density of cells (ρ_T). In the case of *bar*1Δ cells we see that due to the absence of signal attenuation, the respose is simply a function of the density of partner cells (ρ_α). In the next section I provide statistical analysis of the experimental data as a function of population parameters, to show that

the difference between wild-type and $bar1\Delta$ responses is statistically significant.

1.2.3 Statistical analysis of cellular response in mixed population experiments

It is visually clear from Figure 3 *a* and *c* that in the case of wild type cells the response is determined primarily by θ_α, whereas for bar1Δ cells it is simply the amount of emitter ($MAT\alpha$) cells that determines the response. At a fixed ρ_α, moving up the value of θ_α means decreasing the amount of recipient cells as $\theta_\alpha = \frac{\rho_\alpha}{\rho_\alpha+\rho_a}$. According to the model without induction of pheromone (or Bar1) production, the bar1Δ responses at the same value of ρ_α, but different amounts of recipient cells (ρ_a) should be identical. However in the experimental data we see some variation with θ_α as well.

To test the significance of the variation of the response with population parameters, I used a generalized linear model (GLM, [107]). The test has to be performed with two population parameters that define both cell populations, and which are independent of each other. Therefore, I tested the mean responses as a function of ρ_α and ρ_a, which is in effect testing for absolute density sensing versus relative density sensing. In the first case (absolute density sensing, $bar1\Delta$) the response is only a function of ρ_α, and the amount of recipient cells (ρ_a) has no statistically significant effect. In the second case (relative density sensing, shown by wild-type cells) both population sizes, ρ_α and ρ_a, have an effect.

Using a linear model $Y \sim x_1 + x_2$, with Y being the response, the predictor x_1 standing for ρ_α and x_2 for ρ_a; and a normal distribution of the responses at a given value of the predictor, I used $MATLAB$'s $fitglm$ function to perform the statistical analysis. Although using a linear model and a normal distribution can produce negative values for the response (if using the model for predictions), in the range of predictor values I used, this does not pose a problem.

The results obtained are:

Table 1. Statistical test of bar1Δ responses

	estimate	SE	tstat	pvalue
Intercept	0.02	0.002	12.1	8e-19
x_1 (ρ_α)	0.02	0.002	9.1	2e-13
x_2 (ρ_a)	-1e-04	0.002	-0.05	0.96

72 observations, 69 error degrees of freedom. Estimated Dispersion: 6.99e-05.
F-statistic vs. constant model: 42.2, p-value = 1.07e-12.

Table 2. Statistical test of wt responses

	estimate	SE	tstat	pvalue
Intercept	0.02	0.001	23.1	3e-34
x_1 (ρ_α)	0.01	0.001	14	8e-22
x_2 (ρ_a)	-0.006	0.001	-7.23	5e-10

72 observations, 69 error degrees of freedom. Estimated Dispersion: 1.25e-05.
F-statistic vs. constant model: 136, p-value = 1.16e-24.

As expected, statistical analysis shows that for the bar1Δ response the sole significant predictor is ρ_α (the p-value for ρ_a is 0.96). In contrast, for the wild-type response both population parameters, ρ_α and ρ_a, have a significant effect. In the experiments it is the parameters θ_α and ρ_T that have fixed values ($\theta_\alpha = \{0; 0.1; 0.3; 0.5; 0.7; 0.9\}$, $\rho_T = \{0.25; 0.5; 1; 2\}$), so we do not have a plot where responses are grouped by fixed ρ_a values, but instead only by fixed ρ_T values, shown below in Figure 14. Performing a significance test by a GLM for ρ_α and ρ_T leads to the same result, that is, for the *wt* response both variables are significant, whereas for *bar*1Δ only ρ_α is significant.

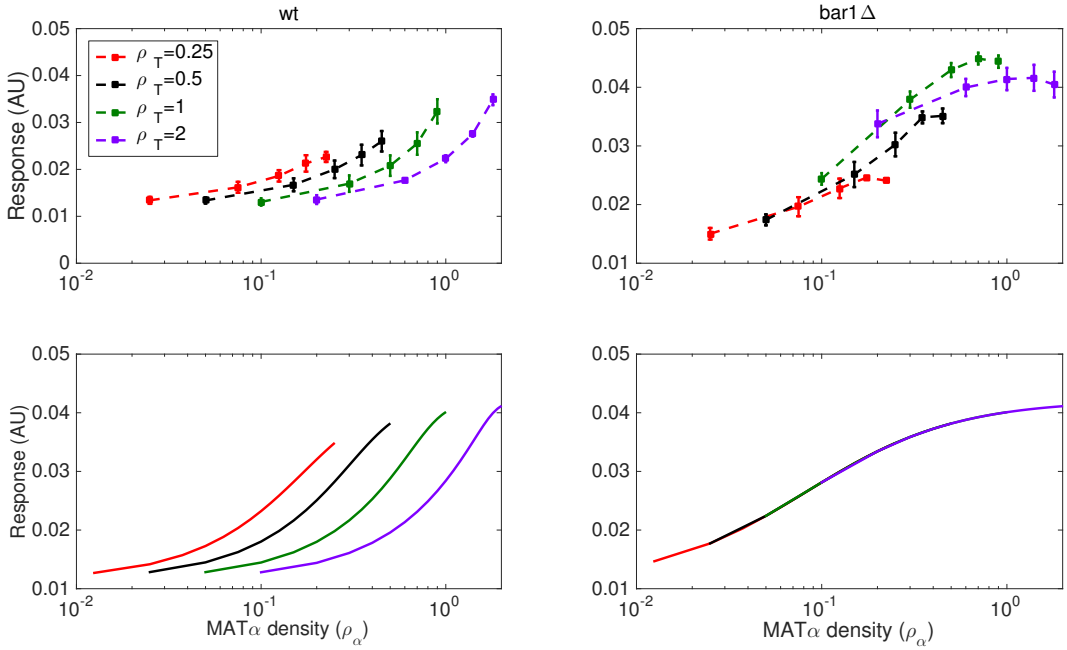

Figure 14. Mean responses in mixing experiments to density of partner cells ρ_α, for *wt* and *bar*1Δ cells, at fixed total cell densities ρ_T. The two panels in the lower row show the corresponding simulations.

With simulations however, I created a $\rho_\alpha - \rho_a$ plot, shown in Figure 15, where the findings of the statistical analysis shown in Table 1 - 2 are visually illustrated.

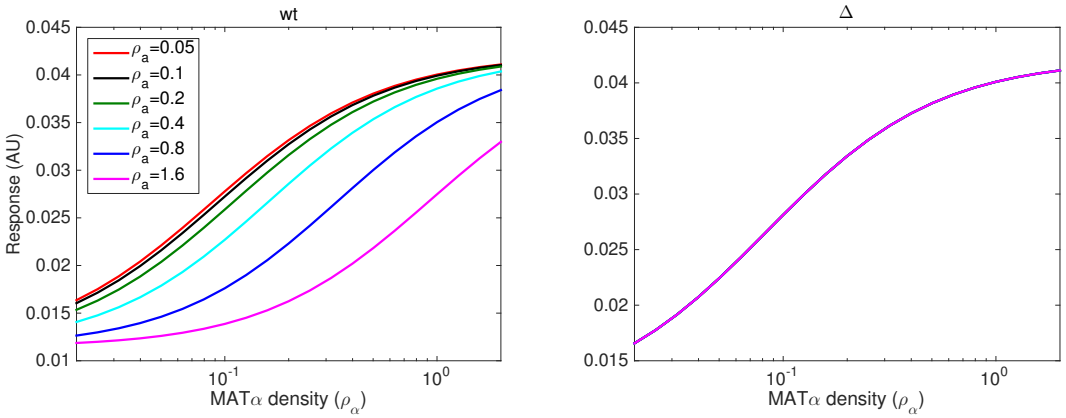

Figure 15. Simulated mean responses in mixing experiments to density of partner cells ρ_α, for *wt* and *bar*1Δ cells, at fixed densities of receiver cells (ρ_a).

To summarize, statistical analysis of the responses by a GLM confirmed what the ODE model predicts, and the experimental results visually suggest. Namely, *wt* cells using signal attenuation carry out relative density sensing, whereas *bar*1Δ $MAT\mathbf{a}$ cells detect only the absolute density of their partners, with their own density (ρ_a) not having a statistically significant effect on their response.

1.3 Optimality of fractional sensing compared to density sensing

1.3.1 Alignment of pathway induction with mating probability

The mechanism described in the previous section represents a new type of population sensing in microorganisms, enabling them to measure the ratio of the two cell types, instead of absolute population density as in the case of conventional quorum sensing. The hypothesis was that the observed dependence of pathway induction on population parameters have a physiological meaning, in coupling the mating response to the likelihood of successful mating.

Formation of mating pairs in a mixed suspension is primarily determined by random cell encounters, with both the sex ratio and population density are determinants of the likelihood of pair formation. If the duration of mating reactions is limited, the probability for a $MAT\mathbf{a}$ cell to collide with a $MAT\alpha$ cell and to form a mating pair will increase both with the population density and with the fraction of the $MAT\alpha$ cells at low population densities. However, it is solely determined by the sex ratio of the population at higher densities, and/or if the reaction is given enough time to reach its steady state.

Describing the probability of mating mathematically, I assumed a simple scenario where collision of cells leads to the irreversible formation of a mating pair. This process can be described by mass action kinetics, without any parameters (rate constants), as:

$$\frac{d\rho_\alpha(t)}{dt} = \frac{d\rho_a(t)}{dt} = -\rho_\alpha \rho_a \tag{37}$$

$$\frac{d\rho_m(t)}{dt} = \rho_\alpha \rho_a \tag{38}$$

where ρ_m is the concentration of mating pairs. I used the conservation relation $\rho_\alpha(t=0) + \rho_a(t=0) = \rho_a(t) + \rho_\alpha(t) + 2\rho_m(t)$ to obtain the analytical solution for the *fraction* of mated $MAT\mathbf{a}$ cells:

$$\tilde{\rho}_m(t) = \frac{1 - exp\,(2(\theta_\alpha - 0.5)\rho_T t)}{\frac{1-\theta_\alpha}{\theta_\alpha} - exp\,(2(\theta_\alpha - 0.5)\rho_T t)} \tag{39}$$

The stationary solution of this equation is

$$\tilde{\rho}_m^{ss} = \begin{cases} \frac{1-\theta_\alpha}{\theta_\alpha}, & \text{if } \theta_\alpha < 0.5. \\ 1, & \text{if } \theta_\alpha \geq 0.5. \end{cases} \tag{40}$$

The steady-state fraction of mated $MAT\mathbf{a}$-cells is completely independent of total density and depends only on the partner cell fraction θ_α. At time points before reaching the steady state there is a dependence on ρ_T as well, as shown in Figure 16.

The $\tilde{\rho}_m^{ss} \propto f(\theta_\alpha)$ relation in Figure 16 at later timepoints is similar, but not identical to the *wt* response at higher densities (Figure 3b, largely independent of ρ_T). Namely, the fraction of mated a-cells reaches 1 and saturates at $\theta_\alpha = 0.5$, whereas the *wt* response spans the entire range of partner cell fractions linearly.

However, we also had experimental data directly testing the dependence of mating pair formation (in a mixed suspension) on the sex ratio. In this experiment wild-type $MAT\mathbf{a}$ and $MAT\alpha$ cells were co-incubated and the free and aggregated fractions of haploid cells were distinguished by flow cytometry. As a negative control, aga2Δ $MAT\mathbf{a}$ strains were used, showing no significant aggregation. This experiment showed a linear dependence of mating pair formation on the sex ratio, shown in Figure 17, akin to the *wt* response in Figure 3.

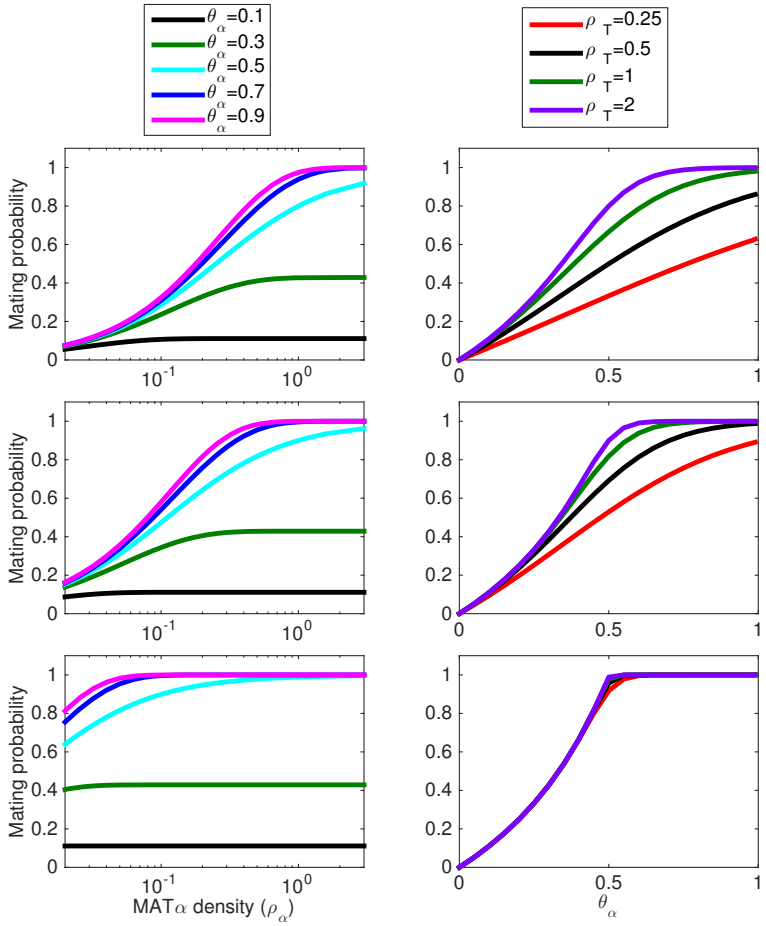

Figure 16. Mating encounter probability simulated using an irreversible mass-action model of cell collisions as a function of ρ_α at fixed values of θ_α (left panel) or as a function of θ_α at fixed values of ρ_T (right panel), at three different timepoints.

The relation $\rho^{ss}_{aggr} = \theta_\alpha$, that is, the fraction of aggregated $MAT\mathbf{a}$ cells equal to partner cell fraction θ_α, persisted over time and did not saturate at $\theta_\alpha = 0.5$ even at later time points. Therefore, at a 1:1 ratio, not all cells can find a partner, showing the sub-optimal aggregation/mating efficiencies already observed in [131]. In short, the wild-type response (Figure 3) follows the empirical probability of mating in a regime of random encounters in a mixed population (Figure 17).

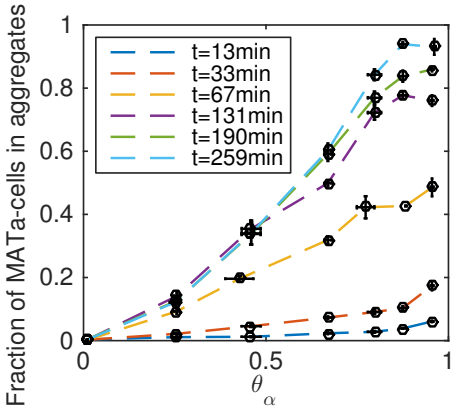

Figure 17. Fraction of aggregated wild-type $MAT\mathbf{a}$ cells as a function of the initial fraction of $MAT\alpha$ cells (θ_α) at a fixed $\rho_T = 0.3$ and at indicated time points. The aggregated fraction was determined as the number of $MAT\mathbf{a}$ cells in aggregates divided by the total number of $MAT\mathbf{a}$ cells. Fitting the results at the last timepoint ($t = 259min$) as a linear function of θ_α (no intercept) yields a R^2 value of $R^2 = 0.95$. Figure from manuscript. Experiment by Dr Alvaro Banderas.

1.3.2 The fitness trade-off of pathway induction: cost and benefit

The alignment of the mating likelihood with the wild-type cellular response pattern implies that yeast cells have evolved to sense the sex ratio, thereby effectively detecting the probability of mating, and inducing the mating pathway in line with this likelihood. This also suggests that pathway induction imposes a fitness burden that is on the other hand counterbalanced by the advantage of a higher mating efficiency. Our experimental data confirms these predictions.

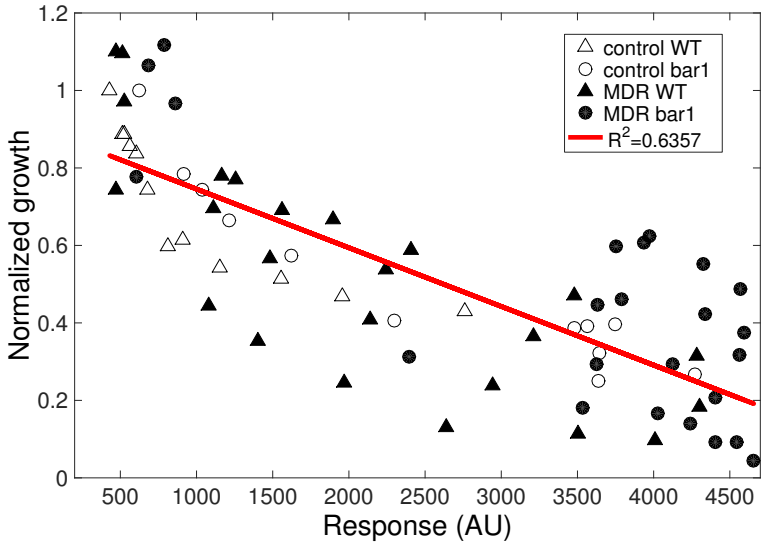

Figure 18. Population growth for the wild-type (triangles) or $bar1\Delta$ (circles) $MAT\mathbf{a}$ cells as a function of the P_{FUS1}-GFP response under stimulation with varying concentrations of purified α-factor (open symbols) or varying density and sex ratio in coincubation experiments (closed symbols). For each sample, the values were normalized to the growth rate of the unstimulated $MAT\mathbf{a}$ populations at equivalent starting ρ_a values. Experiment by Dr Alvaro Banderas.

First, as Figure 18 shows, pathway induction reduces growth linearly. This represents a fitness cost for haploid cells that induce the mating pathway but do not succeed in mating.

On the side of benefits, sexual reproduction is known to have a fitness advantage [111, 137] in many cases, a topic with an extensive literature in evolutionary biology. Specifically, in the case of *S. cerevisiae*, experiments have shown fitness advantages of diploidy under stress conditions such as the presence of antifungal drugs [5], or the presence of mutagenizing agents [95]. Diploids also show a cryptic fitness advantage invading haploid populations and overgrowing them, although showing no clear growth advantage when measured separately in standard fitness assays [60]. Moreover, diploidy also confers the ability to sporulate.

This is the benefit of the formation of diploids, the (potential) *outcome* of pathway induction. More directly, pathway induction should have a (positive) effect on the efficiency of mating itself, in facilitating this beneficial outcome. This hypothesis is confirmed again by experimental observations showing that mating pathway induction in $MAT\mathbf{a}$ cells allows them to outcompete non-stimulated $MAT\mathbf{a}$ cells for access to $MAT\alpha$ partners both in sexual aggregation (Figure 19a) and in mating (Figure 19b) assays. These experiments show that pathway induction has a well-defined benefit (facilitating mating, that is itself beneficial in evolutionary terms) and a cost (reducing the growth rate of haploid cells). Therefore, the response pattern of *wt* cells indeed represents the balancing of a fitness trade-off.

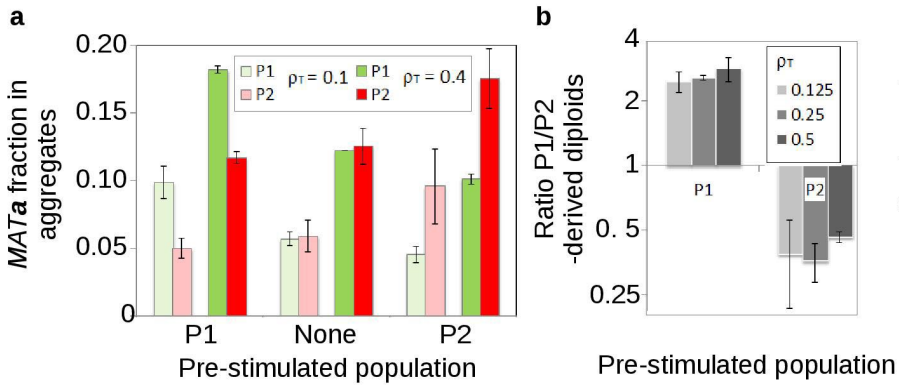

Figure 19. Pre-induction of $MAT\mathbf{a}$ cells with α-factor increases sexual aggregation (a) and mating efficiency (b). Two competing populations ("P1" and "P2") were mixed at a 1:1 ratio and then incubated with $MAT\alpha$ cells at indicated total cell densities (ρ_T). Either of the two differentially labelled populations (indicated on the x axis) was pre-treated with 20 nM pheromone. Plots show the mean and standard deviation of two independent experiments for the fraction of each $MAT\mathbf{a}$ population found in aggregates (a) or the ratios between diploids originating from either $MAT\mathbf{a}$ population (b). Experiment and figure by Dr Alexander Anders.

It is intuitive that in the case of a costly decision that facilitates the attainment of a beneficial outcome, but also has a cost, it is a good strategy to set the relative level of investment equal to

the likelihood of the outcome. The fractional sensing pattern of *wt* cells that I explained by signal degradation in 1.2.1, achieves this alignment.

Below I show quantitatively that this intuition is correct and the investment of cellular resources proportional to mating likelihood is a superior strategy in cost-benefit terms, compared to pathway induction as a function of the absolute amount (density) of partner cells.

1.3.3 Comparison of fractional and absolute sensing strategies

To define the conditions under which sex ratio sensing may confer a selective advantage over partner density sensing for mating induction, I constructed a schematic model that recapitulates the basic features of the two strategies.

To perform this schematic cost-benefit comparison between the wild-type strategy of fractional (sex ratio) sensing and the *bar*1Δ strategy of absolute sensing (or density sensing) of mating partners, I consider the fitness effect of these two regulation strategies on an initial population of haploid $MAT\mathbf{a}$ cells encountering different amounts of partner ($MAT\alpha$) cells (Figure 20*a*).

A fraction of the $MAT\mathbf{a}$ population will mate (benefit), whereas the fitness of $MAT\mathbf{a}$ cells that are stimulated and induce the mating response, but do *not* mate is reduced, e.g. due to a transient cell-cycle arrest (cost, f). The cellular response f is a schematic representation of our experimental data: for the sex-ratio sensor (wild type), the response becomes invariant to total density over a reference value (defined as ρ_T=1), and simply equals the partner cell fraction θ_α (Equation 41). In contrast, the density sensor (*bar*1Δ) simply follows the absolute abundance of partner cells (the product $\theta_\alpha\rho_T$), going into saturation for $\theta_\alpha\rho_T \geq 1$ (Equation 42).

I assume that the efficiency of mating, g, which is the fraction of the initial $MAT\mathbf{a}$ population that forms diploid cells, is proportional to the level of response induction in $MAT\mathbf{a}$ cells, physically limited however by the abundance of $MAT\alpha$ cells as observed experimentally (Figure 17). The resulting model for the wild-type and *bar*1Δ $MAT\mathbf{a}$ cells is the following.

Wild type (fractional sensor)

$$\begin{aligned} f_{WT}(\theta_\alpha, \rho_T) &= \begin{cases} \theta_\alpha\rho_T, & \text{if } \rho_T \leq 1. \\ \theta_\alpha, & \text{if } \rho_T > 1. \end{cases} \\ g_{WT}(\theta_\alpha, \rho_T) &= \begin{cases} \theta_\alpha\rho_T, & \text{if } \rho_T \leq 1. \\ \theta_\alpha, & \text{if } \rho_T > 1. \end{cases} \end{aligned} \tag{41}$$

Bar1Δ density sensor

$$f_\Delta(\theta_\alpha, \rho_T) = \begin{cases} \theta_\alpha \rho_T, & \text{if } \theta_\alpha \rho_T \leq 1. \\ 1, & \text{if } \theta_\alpha \rho_T > 1. \end{cases}$$
$$g_\Delta(\theta_\alpha, \rho_T) = \begin{cases} \theta_\alpha \rho_T, & \text{if } \rho_T \leq 1. \\ \theta_\alpha, & \text{if } \rho_T > 1. \end{cases} \tag{42}$$

where f(θ_α,ρ_T) is the relative response or cost, $f \epsilon [0,1]$; and g(θ_α,ρ_T) is the mating efficiency $g \epsilon [0,1]$. Here I do not consider regulation of $MAT\alpha$ cells, partner cells are treated as a 'resource'.

In general form, the fitness equation for the population is

$$W = \lambda g + (1-g)(1-f) \tag{43}$$

The contribution of diploid cells to the population fitness is the fraction of mated cells (g), scaled by a parameter λ, representing the relative advantage of diploidy [137]. The contribution of the remaining haploid cells to the population fitness is again their fraction in the total population $(1-g)$ times their fitness, which is proportionally reduced with the level of induction, $(1-f)$.

As in our model above $f_{WT}(\theta_\alpha, \rho_T) = g_{WT}(\theta_\alpha, \rho_T) = g_\Delta(\theta_\alpha, \rho_T)$, these functions can be simply replaced by $g(\theta_\alpha, \rho_T)$. The fitness of the population (W) for the wild type or $bar1\Delta$ strategy (at a particular total cell density and partner cell fraction) is, respectively

$$\begin{aligned} W_{WT} &= \lambda g + (1-g)^2 \\ W_\Delta &= \lambda g + (1-f_\Delta)(1-g) \end{aligned} \tag{44}$$

From Equation 42, we can see that $f_\Delta \geq g$, therefore $W_{WT} \geq W_\Delta$ is always true in the current model. Whatever distribution θ_α and ρ_T have, this will also be true for the mean fitness values over these distributions, i.e. $\langle W_{WT} \rangle \geq \langle W_\Delta \rangle$.

With the maximal mating efficiency g limited as above (based on our experimental data, Figure 17), the higher induction of $bar1\Delta$ cells at higher population densities cannot yield higher benefits, but will result in a higher cost. Therefore, the population fitness yielded by density sensing $bar1\Delta$ cells will always be lower.

To make a more general comparison, I consider that cells using the density sensing ($bar1\Delta$) strategy could adjust in an evolutionary sense their response sensitivity to achieve a higher fitness. Then the response, mating efficiency and fitness of the density sensor are

$$f_\Delta(\theta_\alpha, \rho_T) = \begin{cases} c\ \theta_\alpha \rho_T, & \text{if } c\ \theta_\alpha \rho_T \leq 1. \\ 1, & \text{if } c\ \theta_\alpha \rho_T > 1. \end{cases}$$
$$g_\Delta(\theta_\alpha, \rho_T) = \begin{cases} c\ \theta_\alpha \rho_T, & \text{if } c \rho_T \leq 1. \\ \theta_\alpha, & \text{if } c \rho_T > 1. \end{cases} \tag{45}$$
$$W_\Delta = \lambda g_\Delta + (1 - f_\Delta)(1 - g_\Delta)$$

Here the response of the density sensor cells is scaled by a parameter c that can be optimally adjusted to maximize the fitness of the density sensors, as illustrated in Figure 20 *b*.

I further consider that the population parameters θ_α and ρ_T could assume different probability distributions, and I therefore need to calculate a mean fitness value $\langle W \rangle$ over these distributions. I first explore the two limiting cases of no variation in the two parameters and a uniform distribution for both. I then consider the intermediate case of normal distributions of varying width.

1.3.3.1 No variation or uniform distributions for population parameters

In these two limiting cases analytical solutions for the mean fitness can be obtained. In the first limiting case, if there is no variation in θ_α and ρ_T ($\theta_\alpha = 0.5$ and $\rho_T = 1$), then

$$\langle W_{WT} \rangle = 0.5\lambda + 0.25$$
$$W_\Delta = \begin{cases} 0.5\lambda c + (1 - 0.5c)^2, & \text{if } c \leq 1 \\ 0.5\lambda + (1 - 0.5c)0.5, & \text{if } 1 < c < 2 \\ 0.5\lambda, & \text{if } c > 2 \end{cases} \tag{46}$$

In the second and third case (of $\langle W_\Delta \rangle$) it is easy to see that $\langle W_\Delta \rangle$ is smaller than $\langle W_{WT} \rangle$. In the first case of $c < 1$, for $\langle W_\Delta \rangle > 1$, $c + 2\lambda > 4$ has to be true, but for $\langle W_\Delta \rangle > \langle W_{WT} \rangle$ the condition is $c + 2\lambda < 3$, which cannot be both true. Consequently, the density sensing strategy is either identical ($c = 1$) to the wild type, or performs worse.

In the second limiting case, I assume that θ_α is uniformly distributed within the interval [0,1], whereas ρ_T is also uniformly but logarithmically distributed in the interval $[e^{-\gamma} e^{\gamma}]$.

The mean of a function $f(x)$ over an interval $[e^{-\gamma} e^{\gamma}]$, with logarithmically spaced x values (with uniform probability) is:

$$< f(x) >= \frac{1}{2\gamma} \int_{\gamma}^{-\gamma} f(e^x) dx, \tag{47}$$

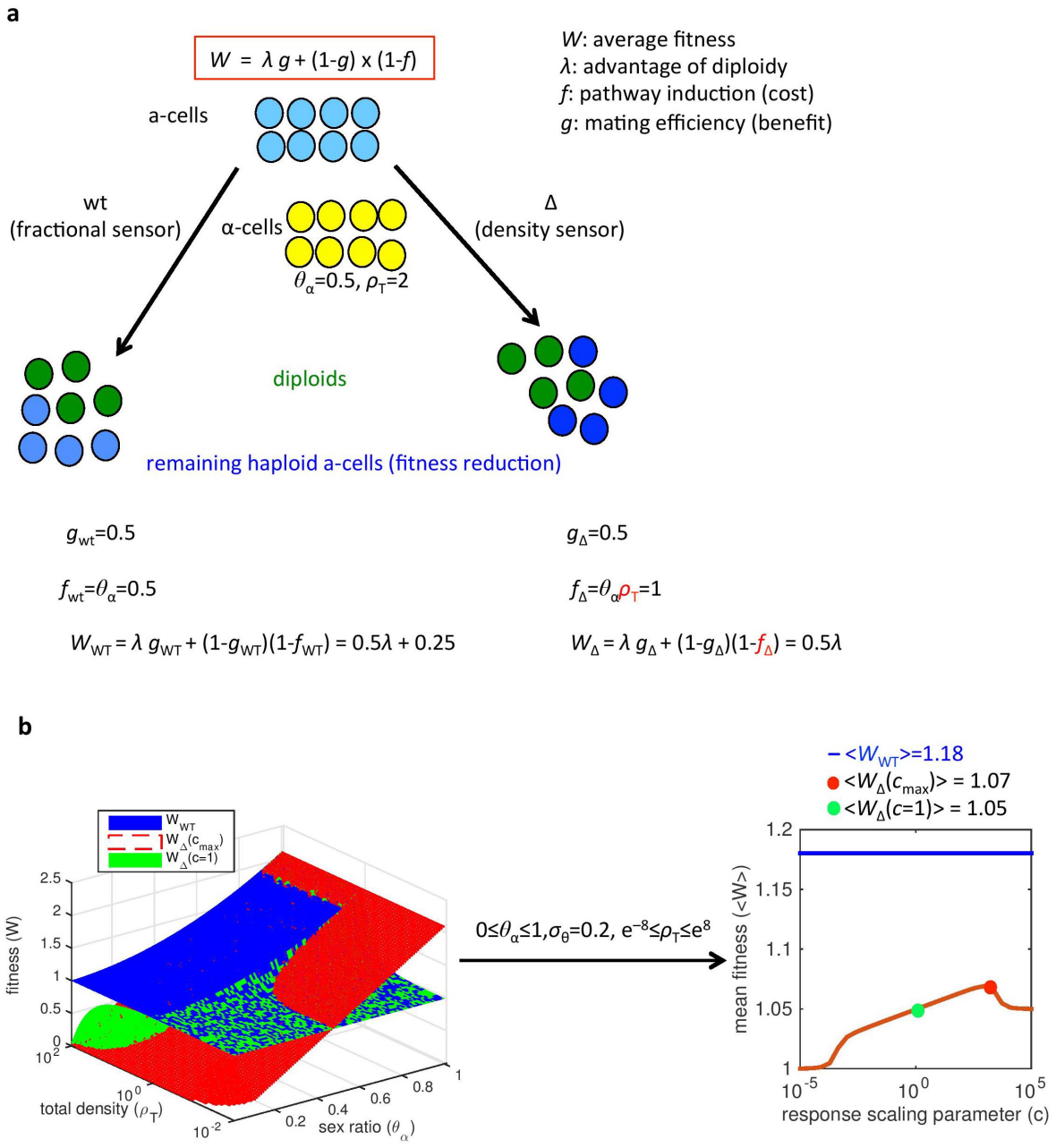

Figure 20. The fitness equation $W = \lambda g + (1-g)(1-f)$ summarizes the balancing of costs with benefits in a mating situation. I describe the benefit as the fraction of the original population forming diploids (set by the mating efficiency g), scaled by a parameter λ, standing for the relative advantage of diploidy. The cost is the fitness reduction $(1-f)$ of the remaining haploid population $(1-g)$. I describe a mating situation with a partner cell fraction $\theta_\alpha = 0.5$ with a total cell density ρ_T=2. In both cases the mating efficiency is $g = 0.5$, half of the original haploid population will mate. However, in the case of the *bar1*Δ (density-sensing) population strategy, the fitness reduction of the remaining haploid cells is heavier, resulting in a lower average fitness of the population. Figure from manuscript.

Integrating over the distributions, I obtained analytical solutions for the mean fitness, which are, respectively:

$$\langle W_{WT} \rangle = \frac{e^{-\gamma}\left(e^{\gamma}(3\gamma\lambda + 8\gamma + 3\lambda - 6) + 2\sinh(\gamma) - 3\lambda + 6\right)}{12\gamma}$$

$$< W_{\Delta} >= \begin{cases} \frac{c^2 \sinh(2\gamma) + 3c(\lambda-2)\sinh(\gamma) + 6\gamma}{6\gamma}, & \text{if } c < e^{-\gamma} \\ \frac{e^{-2\gamma}\left(-2c^4 - 6e^{\gamma}c^3(\lambda-2) + e^{2\gamma}c^2(6\gamma(\lambda+2) + 6\lambda - 5) + 6e^{2\gamma}c^2(\lambda-2)\log(c) - 6e^{\gamma}c + 1\right)}{24c^2\gamma}, & \text{if } e^{-\gamma} \leq c \leq e^{\gamma} \\ \frac{3\gamma c^2\lambda + 3c\sinh(\gamma) - \sinh(\gamma)\cosh(\gamma)}{6c^2\gamma}, & \text{if } c > e^{\gamma} \end{cases} \tag{48}$$

or in general form:

$$\langle W_{\Delta} \rangle = \frac{c^2\left(2e^{2r} - 2e^{-2\gamma}\right) + \frac{e^{-2\gamma} - e^{-2r}}{c^2} + 6\gamma(\lambda+2) + 6e^{-\gamma}c(\lambda-2)\left(e^{\gamma+r} - 1\right) + \frac{6e^{-r} - 6e^{-\gamma}}{c} - 6(\lambda-2)r}{24\gamma} \tag{49}$$

where $r = max(-\gamma, min(\gamma, -ln(c)))$.

For any value of γ (defining variability of total density values) and λ, I take the density sensor strain with the highest mean fitness (an optimal value of c) and compare it to the mean fitness of the wild-type by taking the ratio $\frac{\langle W_{WT} \rangle}{\max\limits_{c} \langle W_{\Delta} \rangle}$. This analysis shows that the fractional sensing strategy outperforms the density-sensing strategy, as long as γ (total density variation) exceeds a minimal value and the advantage of diploidy (λ) is moderate, as it is shown in Figure 21*a*.

1.3.3.2 Normal distribution for θ_{α} and log-uniform distribution for ρ_T

For the intermediate case, I assume that the mean of θ_{α} is 0.5 and the distribution is a truncated Gaussian, as values are only possible in the range [0,1].

$$p(\theta_{\alpha}) = \frac{exp\left(-\frac{1}{2}\left(\frac{\theta_{\alpha} - 0.5}{\sigma_{\theta}}\right)^2\right)}{\sqrt{2\pi}\ \sigma_{\theta}\ erf\left(\frac{1}{2\sqrt{2}\sigma_{\theta}}\right)} \tag{50}$$

The total densities are log-uniformly distributed as in the previous example (Equation 47). The mean fitness values are calculated by numerical integration. For any two distributions of the population parameters (defined by σ_{θ} and γ), I again take the density sensor strain with the highest mean fitness (an optimal value of c) and compare it to the mean fitness of the fractional sensor. As in the case of the uniform distributions (for both parameters) above, I observed that at intermediate values of λ the wild type strategy performs better (i.e., $\left\langle \frac{\langle W_{WT} \rangle}{\max\limits_{c} < W_{constant} >} \right\rangle > 1$) over a wide range of σ_{θ} and γ, with the difference generally growing with σ_{θ} and γ (Figure 21*b*).

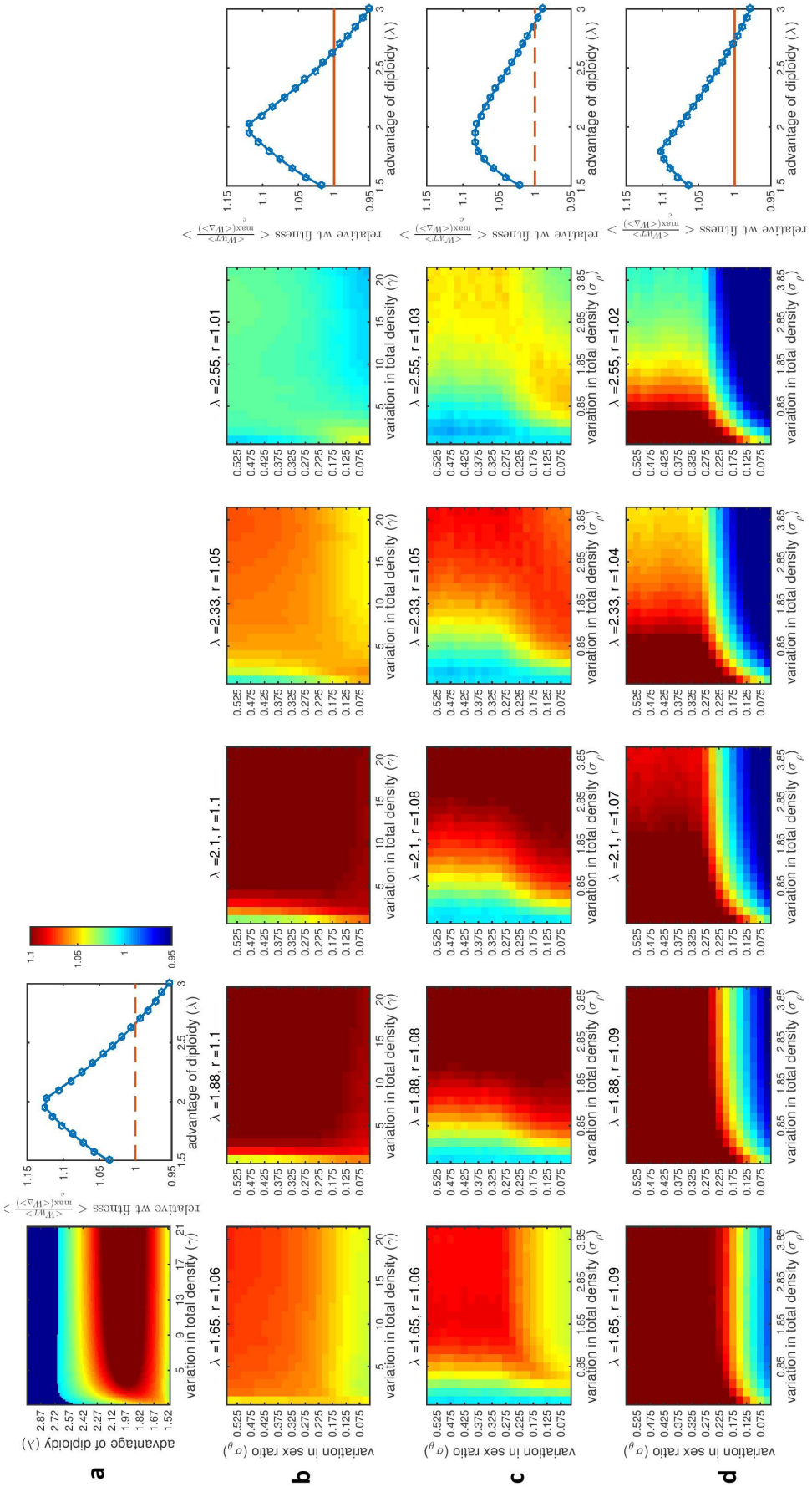

Figure 21. Cost-benefit analysis of mating strategies under different population parameter distributions. Legends on next page.

Figure 21 legends.

a. Cost-benefit model of wild type regulation compared to the density sensing strategy, assuming a uniform distribution of both population parameters θ_α and ρ_T. The ratio $\frac{\langle W_{WT}\rangle}{\max\limits_c\langle W_\Delta\rangle}$ at different levels of λ (value of diploidy) and γ (defining the interval of ρ_T values in which these are log-uniformly distributed). Values smaller than 1 are in blue and not colored gradually. On the right we have the mean of $\frac{\langle W_{WT}\rangle}{\max\limits_c\langle W_\Delta\rangle}$ values over the range of γ values ($1 \leq \gamma \leq 21$), $\left\langle \frac{\langle W_{WT}\rangle}{\max\limits_c\langle W_\Delta\rangle} \right\rangle$, plotted as a function of λ. **b.** The ratio $\frac{\langle W_{WT}\rangle}{\max\limits_c\langle W_\Delta\rangle}$ plotted at different levels of λ, comparing the *wt* fractional sensor strategy with the density sensor ($bar1\Delta$), in the case of a truncated Gaussian distribution for θ_α and a log-uniform distribution of ρ_T. The value r is the average of $\frac{\langle W_{WT}\rangle}{\max\limits_c\langle W_\Delta\rangle}$ values over the range of γ ($1 \leq \gamma \leq 21$) and σ_θ ($0.05 \leq \sigma_\theta \leq 0.55$) values used. On the rightmost panel we have this average, $\left\langle \frac{\langle W_{WT}\rangle}{\max\limits_c\langle W_\Delta\rangle} \right\rangle$, at different values of λ. **c.** The ratio $\frac{\langle W_{WT}\rangle}{\max\limits_c\langle W_\Delta\rangle}$ plotted at different levels of λ, comparing the wild type fractional sensor strategy with the density sensor ($bar1\Delta$), in the case of a truncated Gaussian distribution for θ_α and a log-normal distribution of ρ_T. The rightmost panel shows $\left\langle \frac{\langle W_{WT}\rangle}{\max\limits_c\langle W_\Delta\rangle} \right\rangle$ at different values of λ. **d.** The ratio $\frac{\langle W_{WT}\rangle}{\max\limits_c<W_{constant}>}$ plotted at different levels of λ, comparing the wild type fractional sensor strategy with one of constant investment (pathway induction). The rightmost panel shows $\left\langle \frac{\langle W_{WT}\rangle}{\max\limits_c<W_{constant}>} \right\rangle$ at different values of λ. Figure from manuscript.

1.3.3.3 Normal distribution for θ_α, log-normal distribution for ρ_T

Alternatively, for total densities one can also use a lognormal distribution with the median at $\rho_T = 1$:

$$p(\rho_T) = \frac{exp\left(-\frac{1}{2}\left(\frac{log(\rho_T)}{\sigma_\rho}\right)^2\right)}{\rho_T\sqrt{2\pi}\ \sigma_\rho} \tag{51}$$

I calculated the mean fitness of the population with given distributions of the two population parameters as:

$$< W >= \int_0^\infty \int_0^1 p(\theta_\alpha)p(\rho_T)W(\theta_\alpha,\rho_T)\ d\theta_\alpha\ d\rho_T \tag{52}$$

For any two distributions of the population parameters (defined by σ_θ and σ_ρ) I again take the density sensor strain with the highest mean fitness (an optimal value of c) and compare it to the mean fitness of the fractional sensor. As in the case of the uniform distribution above, I observed that at intermediate values of λ, the wild type strategy performs better, i.e. $\frac{\langle W_{WT}\rangle}{\max\limits_c\langle W_\Delta\rangle} > 1$ over a wide range of σ_θ and σ_ρ, as shown in Figure 21*c*.

1.3.4 Comparison of fractional sensing with a constant-investment strategy

One can also compare the fractional sensing strategy to one where the level of induction is constant and not regulated. In this case, the level of induction f is a constant, f_c, $0 \leq c \leq 1$, and mating efficiency g is $g_c = \begin{cases} c, & \text{if } c \leq \theta_\alpha \\ \theta_\alpha, & \text{if } c > \theta_\alpha \end{cases}$, which yields the fitness function:

$$W_{const} = \begin{cases} \lambda c + (1-c)^2, & \text{if } c \leq \theta_\alpha \\ \lambda\theta_\alpha + (1-c)(1-\theta_\alpha), & \text{if } c > \theta_\alpha \end{cases} \tag{53}$$

Calculating the mean fitness again the same way as before at a certain distribution of θ_α and ρ_T, we have (using a log-normal and a truncated Gaussian distribution):

$$\langle W_{const} \rangle = \int_0^\infty \int_0^1 p(\theta_\alpha) p(\rho_T) W_{const}(\theta_\alpha, \rho_T)\ d\theta_\alpha\ d\rho_T \tag{54}$$

I make two comparisons. In the first case, I compare the constant investment strategy to a fractional investment strategy that is completely independent of the total density. In the second case, I compare the constant investment strategy to our previous fractional investment model, which has density dependence for $\rho_T < 1$.

1.3.4.1 Comparison of density-*independent* fractional sensing (wt) strategy with a constant-investment strategy

Here I assume constant investment, irrespective of the total cell density. Therefore, I first make the comparison with a fractional sensing strategy that is also completely density-independent and has the fitness equation:

$$W_{WT} = \lambda\ \theta_\alpha + (1-\theta_\alpha)^2 \tag{55}$$

First I compare the two strategies in the limiting cases of no variation or a uniform distribution of θ_α. For a fixed θ_α=0.5, we obtain

$$W_{WT} = 0.5\lambda + 0.25$$
$$W_{const} = \begin{cases} \lambda c + (1-c)^2, & \text{if } c \leq 0.5 \\ 0.5\lambda + (1-c)(1-0.5), & \text{if } c > 0.5 \end{cases} \tag{56}$$

The fitness function W_{const} is evidently smaller than W_{WT} in the case of $c > 0.5$ and identical to W_{WT} if $c = 0.5$. In the case of $c < 0.5$, for $W_{const} > 1$ we need $\lambda > 1.5$. The roots of $W_{WT} - W_{const} = 0$ are $c = 0.5$ and $c = 0.5(3 - 2\lambda)$, and between these values of c, W_{WT} –

$W_{const} > 0$. Therefore, if there is no variation in θ_α, the constant investment strategy is identical to the wild type regulation if $c = 0.5$, or is worse if c has any other value.

If θ_α is uniformly distributed, the equations for mean fitness are

$$\begin{aligned} \langle W_{const} \rangle = \int_c^1 \left(\lambda c + (1-c)^2\right) d\theta_\alpha + \int_0^c (\lambda\theta_\alpha + (1-c)(1-\theta_\alpha))\, d\theta_\alpha = \\ = \frac{1}{2}\left(-c^3 - c^2(\lambda-3) + 2c(\lambda-2) + 2\right) \\ \langle W_{WT} \rangle = \int_0^1 \lambda\theta_\alpha + (1-\theta_\alpha)^2 d\theta_\alpha = \frac{1}{6}(3\lambda+2) \end{aligned} \tag{57}$$

For $\langle W_{const} \rangle > \langle W_{WT} \rangle$ to be true, $\lambda < \frac{-3c^3+9c^2-12c+4}{3(c-1)^2}$. But $\langle W_{const} \rangle$ also needs to be larger than 1 to be a viable strategy of investment of resources into mating, and the condition for this is $\lambda > \frac{c^2-3c+4}{2-c}$. But for $0 < c < 1$, these two conditions cannot be true at the same time, as $\lambda < \frac{-3c^3+9c^2-12c+4}{3(c-1)^2} < \frac{c^2-3c+4}{2-c}$. Therefore, the constant investment strategy always performs poorer than regulated fractional investment under a uniform distribution of the partner cell fraction.

1.3.4.2 Comparison of density-*dependent* fractional sensing (wt) strategy with a constant investment strategy

Alternatively, one can compare the fitness of the constant investment strategy to the density-*dependent* fractional (wild type) strategy by again taking the ratio $\frac{\langle W_{WT} \rangle}{\max_c \langle W_{const} \rangle}$ as a function of σ_θ and σ_ρ, and at different λ values. Again, at each value of σ_θ, σ_ρ and λ the best-performing 'constant investor' (highest $\langle W_{const} \rangle$) is compared to the fitness of the fractional sensor. A constant investment strategy performs poorer when the partner cell fraction has higher variation (Figure 21*d*). As in the other comparisons, at intermediate λ values the fractional sensor strategy outperforms the constant investment strategy (Figure 21*d*).

In summary, the cost-benefit analysis I performed demonstrates that sex ratio-modulated (fractional) mating induction leads to a higher population fitness than sensing the absolute density of partners, or the unregulated, constitutive activation of the pathway. This result holds even if the density sensor strategy is permitted to optimize the sensitivity of induction to the distribution of θ_α and ρ_T values, while the sex ratio sensor is not. Therefore, sex-ratio sensing should be selectively favoured as long as the benefits of diploidy are modest, which is upheld for yeast [172], and the composition of the population is variable.

1.4 Conclusions

In this section of my thesis, I mathematically analyzed the signaling and regulatory system that controls the commitment to mating in one of the two haploid types ($MAT\mathbf{a}$) of the sexually reproducing unicellular microbe, *Saccharomyces cerevisiae*.

I started the analysis by an experimental observation on the level of induction of the mating pathway reporter gene $P_{FUS1} - GFP$ in wild type $MAT\mathbf{a}$ cells as a function of population parameters. The mating pathway's function is to detect the availability of potential mates and control the process of mating, and its output can be interpreted as an indicator of a cell's commitment to mating. Any mixed population can be defined by two parameters: the composition of the population (defined by the fraction of $MAT\alpha$-cells, θ_α), and the total density of the population, ρ_T. The level of pathway induction in *wt* cells is a linear function of the fraction of partner ($MAT\alpha$) cells (θ_α) in the population, while showing sensitivity to the total cell density of the population (ρ_T) only at low levels, with the response becoming solely a function of the fraction if the total density is sufficiently high.

By mathematical analysis I showed that signal degradation by the recipient cell-secreted enzyme Bar1 can explain this response pattern. If the enzyme is unstable, the steady state level of α-pheromone is equal (up to a constant defined by the kinetic parameters of production and degradation) to the sex ratio, that is, the ratio of emitter ($MAT\alpha$) to recipient ($MAT\mathbf{a}$) cells. In reality however, Bar1 is stable on the timescale of the mating assays, therefore I modified the model accordingly. In this case, α-factor concentration has a non-monotonic dynamics, reaching a maximum before starting to fall to zero. The total stimulation over time, that is, the time integral of the signal up to its maximum (or to a time point where it falls back to a given fraction of its maximal concentration) is again equal (up to a constant) to the sex ratio. Moreover, if the signal induces a linear signaling pathway, the time integral of transcriptional output, a measure of the total resource investment of the cell associated with the mating pathway, is again equal (up to a constant) to the sex ratio, although showing a very weak dependence on total cell density as well.

By using a more detailed non-linear model of the pathway, this linear response with the sex ratio can be converted to a linear response to the fraction (θ_α) of partner cells, as it is observed experimentally. I numerically fitted this model at many different population parameter values (pairs of θ_α and ρ_T values) to our experiments with wild type and $bar1\Delta$ cells, the latter lacking signal attenuation. With the non-linear model, I recovered the observed patterns of fractional sensing in the case of wild type cells, and density sensing for $bar1\Delta$ cells.

As we are looking at yeast mating in suspension with large numbers of cells, one can consider

mating to be a mass action-like process, driven by population parameters and the interaction strength for aggregation. A simple calculation shows that if mating is modeled as an irreversible reaction, the steady state fraction of mated cells for one cell type ($MAT\mathbf{a}$) is determined only by the fraction of partner cells (θ_α), independently of the total density of the population, although at pre-steady state timepoints, total density also has an effect. Experimental evidence shows that the fraction of aggregated $MAT\mathbf{a}$ cells is in fact equal to the partner cell fraction θ_α, meaning that the response of fractional sensing wild type cells is aligned to mating probability.

This predictive allocation of cellular resources proportional to the mating likelihood suggests that there is a fitness trade-off to pathway induction. On the one hand, pathway induction has a benefit: it is necessary for and facilitates mating, leading to diploid formation, which is the evolutionarily favoured strategy of yeast. On the other hand, experiments show that pathway induction also has associated costs as the growth rate of induced (non-mated) haploid cells is proportionally reduced. I constructed a cost-benefit model incorporating this trade-off, comparing fractional sensing (shown by wild type yeast cells) to the strategy of sensing the absolute density of partners (shown by $bar1\Delta$ cells). I found that as long as the benefit of diploidy is below a certain level, the fractional sensing strategy of wild type cells is superior, yielding a higher mean population fitness, for various distributions of the population parameters.

In summary, I provided a mechanistic explanation of the fractional sensing pattern observed in yeast $MAT\mathbf{a}$ cells. In a mixed population of two cell types, a simple signal degradation mechanism through a secreted, non-saturated enzyme by recipient cells transforms the pheromone signal produced by emitter cells, so that the cumulative signal strength is equal (up to a constant) to the ratio of emitters to recipients. This mechanism applies generally for any biomolecular system with the same structure. A non-linear signaling pathway then converts the signal strength to a response that scales linearly with the fraction of emitter cells in the population, thereby aligning the response of recipient cells with their likelihood of finding a mate. Finally, because the response (pathway induction) has both a cost and a benefit for cells, this strategy of response alignment with the likelihood of mating was shown to be optimal in cost-benefit terms by a schematic fitness model.

Additionally, as described in section 4.1 of the Appendix, I used information theory to quantify the information transmission capacity of wt cells. Much of the variation we observe in the response of a population is due to variation in the expression capacity of cells. I wanted to have a measure of the fidelity of signaling by removing this source of variation in the population data. Using a linearization approximation for the noise components this correction can be performed and yields an improved estimate of signaling fidelity.

2 Microbial memory: bistability in bacterial two-component systems

2.1 Introduction: two-component systems

Two-component (TC) systems are the most prevalent signaling systems in bacteria, found in hundreds of bacterial species. Typically, in a bacterial cell we find a few dozen to a hundred separate TC pathways [29, 82], see Figure 22, consisting of a membrane-bound histidine sensor kinase (SK) and an intracellular response regulator (RR), functioning as a transcription factor. The number of TC systems scale approximately linearly with the genome size [29].

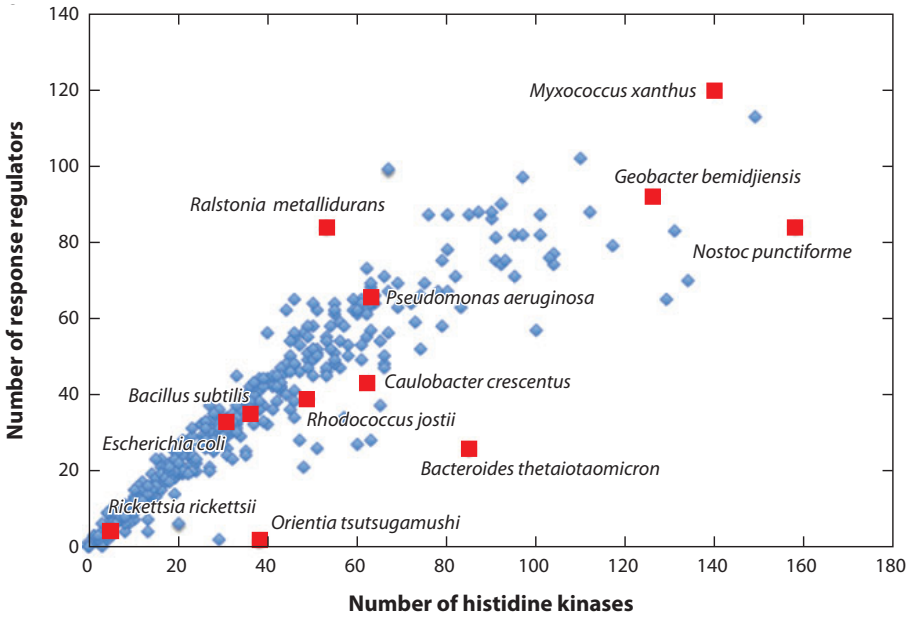

Figure 22. Number of histidine kinases and response regulators in different bacterial species. Most genomes contain equal numbers of kinases and regulators, as pathways typically consist of one kinase and one cognate response regulator. In the remaining cases, there are usually more kinases than regulators, making it possible for response regulators to integrate signals from multiple kinases. Figure from [29].

Besides the bacterial kingdom, TC systems are also present in some archaea, plants, and lower eukaryotes; however they were lost in metazoans. Throughout evolution, bacteria have expanded their spectrum of two-component signaling proteins via gene duplication and lateral gene transfer. In the evolution of TC signaling proteins, domain shuffling is ubiquitous, especially following gene duplication, leading to the rapid emergence of new sensory and regulatory functions. Moreover, the transcriptional outputs of TC signaling systems also show very high plasticity, with the gain and loss of cis-regulatory elements being very common. This can lead to diversification of the transcriptional repertoire of RRs. Co-evolution of cognate SKs and RRs have been widely reported

[29], a phenomenon required to avoid cross-talk, which is generally preferred to retain pathway specificity, although cross-talk between pathways also occurs [87, 135] and may represent a form of signal integration.

The structure of TC systems is simple, consisting of two components, the SK and its target, the intracellular RR. The sensor histidine kinase (SK), working in two steps, functions differently from eukaryotic kinases. First, in the presence of its input ligand, the SK phosphorylates itself by binding and hydrolyzing ATP. The rate constant of this autophosphorylation step (denoted c_0 later on) is a function of the ligand (input) concentration $[L]$. In the models below, I simply use the rate constant c_0 as the input parameter of a TC system. In reality, the rate of autophosphorylation might have a nonlinear relationship with the ligand concentration, but as I start the model at the rate constant itself, including this nonlinearity would not change our results. The auto-phosphorylated SK then transfers a phosphoryl group to the RR in a phospho-transfer step, thereby activating it. These two steps are universally found in almost all bacterial two-component systems.

Another crucial feature of TC systems that is not always present is the bifunctionality of the SK [2]. A bifunctional SK not only transfers its phoshphate group to the RR, but also, in its dephosphorylated state, *de*phosphorylates its cognate RR [72, 114, 115, 134]. Not all TC systems have a bifunctional SK, for instance the SK of the chemotaxis system in *E. coli*, CheA, is monofunctional and can only phosphorylate its cognate *RR*, CheY, but not dephosphorylate it (there is a separate phosphatase, CheZ). Once phosphorylated, the RRs undergo a conformational change and effect a physiological change by binding to the promoter region of the gene(s) that is (are) under their control. RRs in most cases homo-dimerize following phosphorylation and then bind to DNA, but there are also single-domain RRs [57, 58].

The inputs to TC systems are various. The SK often reacts to the concentration of an extracellular ligand, such as phosphate (PhoB/PhoR system, [31]) or nitrate (NarX/NarL, [170]). In other cases the input is an environmental parameter such as osmolarity (EnvZ/OmpR system [71]), oxygen limitation (ResE/ResD, [105]) or turgor pressure (PhoQ/PhoP, [103]). In some cases, the ligand is not known (e.g. in the YedV/YedW system [65]).

In terms of the physiological function of TC systems we can divide them into three groups.

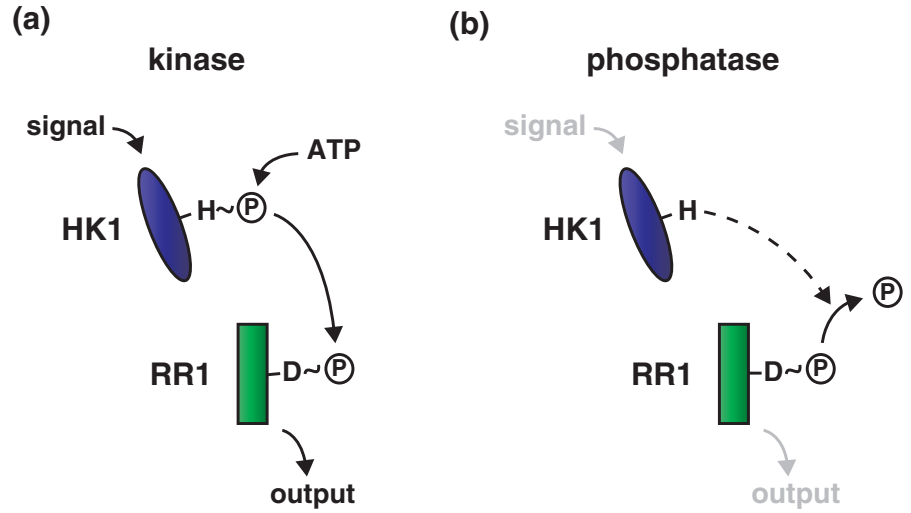

Figure 23. The canonical TC signal transduction system with a bifunctional SK. **a.** Activated by its ligand, a canonical SK uses ATP to autophosphorylate itself on a histidine residue, and then transfer its phosphoryl group to a conserved aspartate of its cognate RR, which can then activate gene expression. **b.** Most SKs are bifunctional and in the absence of their ligand, the unphosphorylated SK will dephosphorylate its cognate RR, deactivating the response. Figure from [118].

In the first group are some TC systems that are environmental sensors (e.g. PhoR/PhoP [64] in *B. subtilis*, BaeS/BaeR [11] in *E. coli*, and SphS/SphR [146] in *Synechocystis*), detecting some ligand or physico-chemical parameter of the environment and (usually) gradually inducing a corresponding transcriptional response.

In the second group we have TC systems that play a role in differentiation and cell cycle transitions. These are often processes that need switch-like or hysteretic control. Examples are developmental phospho-relays, such as DivJ/DivK [113] and PleC/PleD [1] in *B. subtilis* or the YycG/YycF [70] TC system in the same species.

Third, some TC systems control growth or virulence in a particular environment, such as CreC/CreB [86], NarX/NarL [170], and YehU/YehT [84] in *E. coli*, and PrrB/PrrA [44] in *Mycobacterium tuberculosis*.

For the latter two types of TC systems, a switch-like response, and hysteresis in switching can be advantegous: once a developmental, transition-like decision is made, at least in some range of the input variable, it should not be reversed even if the input falls back to its original level. In other words, the TC system in these cases might have multiple steady states in some range of their input parameter, a phenomenon called multistability, that I discuss in the next section.

2.2 Multistability (multi-stationarity) in the systems biology literature

The presence of multiple stable steady states as a function of a control parameter and the resulting hysteresis effect have been studied extensively in systems biology; indeed, it is one of the foundational themes of the field [51, 52, 66, 97, 109, 110, 121, 155].

In the systems biological literature two principal mechanisms have been identified that can lead to bi- or multistability. Some of the literature considered post-translational mechanisms only, typically phosphorylation-dephosphorylation systems, where the total concentrations are fixed, but enzymes (kinases) and their substrates can exist in several modification forms ('phospho-forms' [67, 153]). In such multi-site modification (phosphorylation) systems, multiple steady states are already possible. The first analysis that showed that bistability is possible in a two-site phosphorylation-dephosphorylation system was by Kholodenko and colleagues [97, 110]. Subsequently a large analytical literature has emerged on the algebraic analysis of the steady-states of such multi-site chemical modification systems, pioneered by Jeremy Gunawardena [32, 48, 49, 67, 68, 83, 121, 153]. These studies showed that with a growing number of modification sites (and therefore of chemical species in the system), the number of stable steady states can be more than one (and even more than two), especially if scaffolding mechanisms [14, 32, 145] and compartmentalization [19, 68] are also taken into account. In mechanistic terms, the bi- or multistability in these systems is due to enzyme sharing [48], i.e. that kinases and/or phosphatases catalyze multiple reactions, and therefore interact with many species. This results in competition between substrates for enzymes, creating implicit feedback effects that can lead to multi-stability.

The complexity of these systems is increased further in the case of phosphorylation-dephosphorylation cascades with multiple levels, when kinases are activated by other kinases. In this case, enzymes are also substrates and the interactions through the competing sequestration of components ("intrinsic feedbacks" [132]) can lead to not only multi-stability, but also oscillations, without any explicit feedback loops [47, 78, 121, 164, 165, 168, 173]. Importantly for our analysis on TC systems below, a study by Legewie and colleagues [89] showed that if enzymes can also bind to their substrate in their inactive form, forming (reversibly) so-called 'dead-end' complexes, this can extend the range of bistability in MAPK cascades. Such interactions are bound to occur as the selectivity of the enzymes is not perfect. Such post-translational mechanisms of intrinsic feedbacks leading to multi-stability have been analyzed extensively mathematically, but experimental data showing such 'purely' post-translational bi-/multistability has not yet been produced, although retroactive effects flowing from downstream to upstream components in multi-level signaling cascades have been

shown [78].

The second, more well-known and experimentally confirmed mechanism leading to bistability is the existence of explicit positive feedback loops, in particular transcriptional feedback loops [50, 51, 102]. Besides many eukaryotic examples, there are bacterial systems as well that are bistable because of transcriptional auto-induction [42, 156], such as the system regulating genetic competence [138, 143, 161] or the sporulation network [30, 161] in *Bacillus subtilis*. Bistable genetic control systems that are based on double inhibition have also been described in bacteria [59], but as TC systems are auto-inducing through a direct positive transcriptional feedback loop, I will not analyze them. Moreover, 'growth bistability' has also become the focus of attention lately: the expression of a protein is a burden on the growth rate, slowing down the protein's dilution, working as an additional positive feedback loop that can lead to bistability, as shown experimentally [39, 148].

Turning to TC systems, I asked the question if these simple sensory systems that microbes use to explore and react to their environment are capable of generating bistability.

On the one hand these systems are extremely simple, so in terms of post-translational interactions they lack the complexity of eukaryotic phosphorlyation cascades with several phospho-sites and/or multi-level cascades. An article by Igoshin and co-authors [72] however showed by numerical calculations that interaction between inactive SKs and RRs (i.e. if the RR can dock and reversibly bind to the SK when both are unphosphorylated, forming a 'dead-end' complex) can lead to bistability under some conditions. The conditions for bistability were not analytically investigated in this study, and the analysis was carried out for one network topology. In another study [4], so-called 'split' histidine kinases were shown to have the capacity of bistability, along with systems with a 'phosphate sink', where a single SK phosphotransfers to two separate RRs [3].

On the other hand, the fact that most TC systems are self-inducing, that is, the activated RR induces the production of the system's own components raises a plausible question if they are capable of transcriptionally induced bistability. In a number of studies the possibility of such feedback-induced bistability was investigated [61, 144, 156, 157, 158], mainly through numerical simulations. These models included additional features however, for example the system described in [156, 157] includes multiple transcriptional feedback loops.

Our aim was to explore systematically the potential for bistability in a number of experimentally described and/or biochemically plausible TC system topologies with different post-translational mechanisms, if possible analytically, to prove conclusively if a certain topology is capable of

bistability or not.

In the case of transcriptional induction I wanted to see if the 'core' TC topology of a bifunctional SK and auto-induction of both components is sufficient for bistability, without additional components.

Besides the existence of bistability for a given topology, I also identified the key parameters in bistable behavior, made possible by the algebraic method described below. The existence of bistability itself can also be ascertained by using the so-called deficiency-theory (from chemical reaction network theory) developed by Feinberg and others [45, 46], provided the kinetic system only has elementary mass action terms, but no rational functions such as Hill-functions.

There a number of reasons why bistable behavior in a TC system can be advantageous. First, as already mentioned above, in the case of a TC system controlling a developmental event, an abrupt transition is needed, provided by the bifurcation that a bistable response generates at a certain value of the input parameter. Second, in the case of a transition activating a complex expression program with many genes and therefore having high costs, shifting to the 'on' state often has to be irreversible either completely or to some extent. Once the bifurcation happens, lowering the input parameter should not make the system move back to the lower branch of steady states (Figure 24 *a*). The reverse bifurcation, with the system moving back to the lower branch of steady states, happens only at a lower value of the input parameter, or never, if the upper branch extends back to the lowest value of the input parameter.

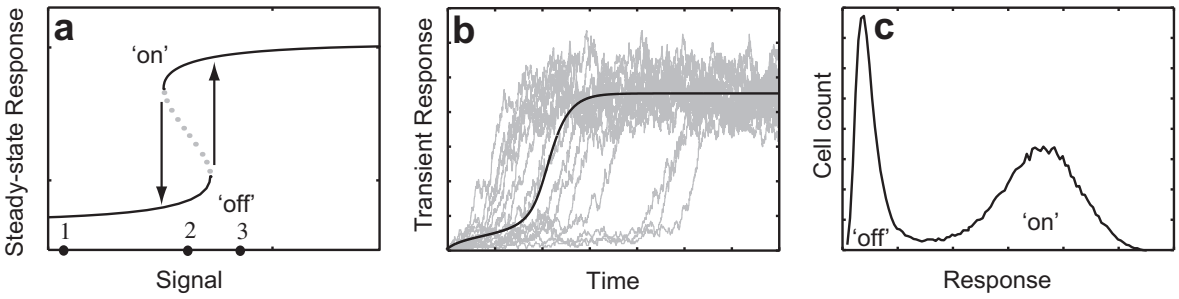

Figure 24. Properties of bistable systems in a deterministic and stochastic framework. **a.** A bifurcation diagram showing the steady-state response of a bistable system at different values of the input paramater. Solid curves show the stables steady states. At the black arrows, the response jumps to the higher steady state (saddlenode bifurcation). **b.** Deterministic (solid line) and stochastic trajectories when the input is increased from point 1 to 3 (panel *a*). Grey curves show stochastic simulations with large heterogeneity in response times. **c.** The population distribution when the input parameter is at point 2 (panel *a*) shows bimodality, in stochastic simulations [62]. The two peaks correspond to the high and low steady states at point 2. Figure from [158].

This means, that the system has *memory* in some range of the input signal: which steady state it assumes depends on its history, and once it adapts to one of the branches of steady states it will stay there, even if the input changes (within some range). This is often a required property for cell fate decisions, where minor fluctuations in the input should not shift the system back to its initial 'off' state. With regard to the dynamical behavior of bistable systems, in the vicinity of the bifurcation points there is a slow-down effect, so that the stimulation needs to be more sustained [100, 126], working as a filtering mechanism against transient fluctuations in the input.

Biological signaling systems, especially in bacterial cells, operate with a relatively small number of interacting molecules, in bacteria typically from a few dozen to a few thousand copies of a given protein. Therefore a deterministic description does not capture all properties of the system, and stochastic effects play an important role. In the case of bistable systems, as shown in Figure 24*b* and *c*, if the input parameter is in the range of two stable steady states, the noise-induced, stochastic switching of cells results in a bimodal distribution of the response, when looking at the population in stochastic simulations or experiments with single-cell resolution (e.g. flow cytometry) [42, 143, 148, 162, 163]. This phenomenon of two distinct sub-populations is called 'bet-hedging' and was shown to be a strategy employed by bacteria in the case of developmental switches, the most well-studied example being sporulation in *B. subtilis* [55, 56]. Bet-hedging, that is, a clonal population of (bacterial) cells under the same conditions showing phenotypic variability, was shown to increase the fitness of a population (compared to a homogeneous population) under some conditions [163]. However a bimodal distribution on the population level is *not* always the sign of an underlying bistable control system, as expression noise and a monostable, but strongly nonlinear (ultrasensitive) input-output relation can generate a bimodal response distribution on the population level without multiple steady states and hysteresis being present [22, 160].

The emergence of two distinct subpopulations under identical conditions can be advantageous as a form of risk spreading: at least some of the cells will fit the (future) environment and survive. This strategy might not be an ideal strategy in a stable environment, but in a variable environment a heterogenous population can have a fitness advantage and outcompete a homogenous population, as theoretical studies have shown [85, 150]. I now turn to the algebraic method used to identify topologies capable of bistability and the analysis of individual topologies.

2.3 Post-translational mechanisms leading to bistability in TC systems

TC systems in the deterministic limit can be described as systems of coupled ordinary differential equations. I use elementary step mass action kinetics, avoiding approximations such as linear or Michaelis-Menten kinetics, as these often do not apply to signaling systems where the

concentrations of enzymes and substrates are comparable [24, 99]. In the case of looking at post-translational mechanisms only, I abstract from production and degradation of the chemical species of the reaction network and ask if post-translational mechanisms can lead to bistable behavior on their own. These post-translational mechanisms include autophosphorylation, phosphotransfer and dephosphorylation reactions, and the formation of complexes between molecules.

The algebraic method to determine the possibility of multistability is the following, already used in [48]. In each case, our system is described as a dynamical system $\dot{x}_i = f(x_i)$, with i = 1...n. These n polynomial differential equations are complemented by k conservation laws of the form $\overline{Y_j} = g_j(x)$, with $\overline{Y_j}$ the total concentration of RR or SK (or some other species), and $g_j(x)$ the different modification forms of a molecule that sum up to a conservation constraint. As I am looking at the steady state properties of the system only, the left side of all ODEs are set to 0, transforming the system into one of coupled (nonlinear) algebraic equations.

By successive elimination of variables we arrive at an algebraic relation $\overline{Y_j} = \varphi(x_i)$, that is, an equality between a conserved quantity of the system (a total concentration) and a rational function φ in one of the variables, x_i. The variable x_i is the steady state concentration of one of the species of the system. The terms in φ will contain parameters, including other total concentrations than $\overline{Y_j}$.

For example, we end up with an equation $RR_T = \varphi(RRP)$, with $\varphi(RRP)$ a sum of all species containing RR (in phosphorylated or unphosphorylated form, free or bound to other species), each of them expressed as functions of RRP (typically ratios of polynomials in RRP), the phosphorylated form of RR.

Because all concentrations are non-negative, RR_T is restricted to a set Γ of possible values. Moreover, for any $RR_T \geq 0$ there is at least one (biologically meaningful) steady state, i.e. a relation $RR_T = \varphi(RRP)$.

I have found no examples of more than three (two stable) steady states, so from here on will discuss bistability only. Whether bistability is possible can be seen from the analysis of φ. If the function is strictly decreasing or increasing then for any given total amount of RR_T there is a unique RRP steady state value, and therefore bistability cannot occur. If on the other hand, φ has increasing and decreasing parts (or Γ is not connected, but I have not found examples of that, see below), then multiple steady states might exist at some RR_T, such that $RR_T = \varphi(RRP_1) = \varphi(RRP_2) = \varphi(RRP_3)$ and $RRP_1 \neq RRP_2 \neq RRP_3$. This means that at some total concentration there are three steady state concentrations of RRP that satisfy the conservation relation. Once it is found that a topology is capable of bistability, I further analyze

the function φ to try to identify parametric conditions for bistability.

Post-translational mechanisms that I review below are:

- bifunctional and monofunctional SK
- spontaneous dephosphorylation of SKP and/or RRP
- 'dead-end' complex formation between SK and RR
- the existence of a separate phosphatase that dephosphorylates RRP
- binding of the SK or RR to some other cellular species, e.g. the SK or RR of another TC system, as an example of crosstalk between TC systems [63, 166]

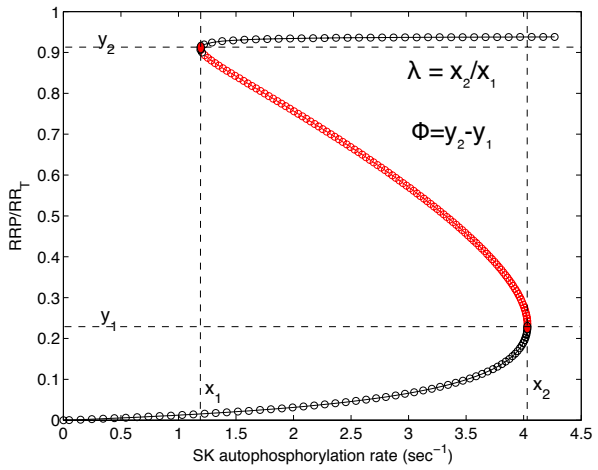

Figure 25. Metrics of a bistable response. The bistability output range Φ is the difference in the normalized response (RRP/RR_T) between the bifurcation points y_1 and y_2, whereas the input range λ is the ratio of the input values between which we have multiple steady states.

The standard topology of a TC system, with a bifunctional SK, no spontaneous dephosphorylation of either RRP or SKP, and no interaction between the inactive species was described in [134], and I do not reproduce it here. In this case the only dephosphorylation process of the RRP is the enzymatic dephosphorylation by the SK. As was shown by Shinar *et al* [134], the steady state RRP concentration, that can be considered as the output of the system, is invariant of the total RR_T and SK_T concentration, as long as these are not limiting. Variations of this topology including spontaneous dephosphorylation were also analyzed in [134] and show no bistability.

For all topologies below I take the autophosphorylation rate c_0 to be the input parameter of the system, that is the function of the ligand concentration. I define two metrics for bistability, the output range Φ and the input range λ, shown in Figure 25.

The units and median values of parameters for the numerical sampling are shown in Table 3.

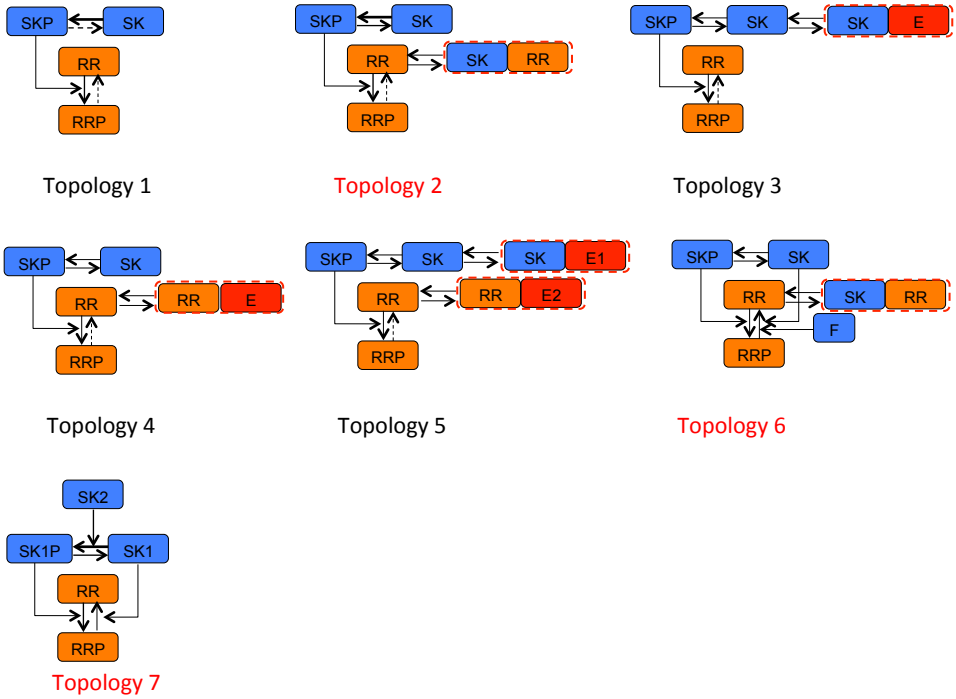

Figure 26. Topologies with post-translational mechanisms only (fixed total concentrations) analyzed for bistability. Index of topologies capable of bistability written in red.

Table 3. Unit and median of the randomly generated parameter values for topologies with post-translational mechanisms only. Every parameter is generated from a lognormal distribution with a standard deviation of 2.

Parameters	Unit	Logarithm of median
a_1, a_2, a_γ	$(\mu M min)^{-1}$	1
d_1, d_2, d_γ	min^{-1}	1
c_1, c_2, c_α, c_β	min^{-1}	1
SK_T	μM	1
RR_T	μM	1
$SK1_T$, $SK2_T$	μM	1
E_T	μM	1
F_T	μM	1

2.3.1 Topology 1 (monofunctional SK, spontaneous dephosphorylation)

This topology has a monofunctional SK, and spontaneous dephosphorylation of both SKP and RRP. The *SKP-RR* complex is denoted as X_1.

The ordinary differential equations are:

$$\begin{aligned}
\dot{SK} &= -c_0 SK + c_\alpha SKP + c_1 X_1 \ (1)\\
\dot{SKP} &= c_0 SK - c_\alpha SKP + d_1 X_1 - a_1 SKP\ RR \ (2)\\
\dot{RRP} &= c_1 X_1 - c_\beta RRP \ (3)\\
\dot{RR} &= d_1 X_1 + c_\beta RRP - a_1 SKP\ RR \ (4)\\
\dot{X_1} &= a_1 SKP\ RR - (d_1 + c_1) X_1 \ (5)
\end{aligned} \tag{58}$$

The conservation laws:

$$\begin{aligned}
SK_T &= SK + SKP + X_1\\
RR_T &= RR + RRP + X_1
\end{aligned} \tag{59}$$

After setting the derivates to 0 for steady state, and variable elimination, I end up with the rational function φ:

$$SK_T = \varphi(X_1) = \frac{c_\alpha}{c_0}\frac{(c_1+d_1)X_1}{a_1(RR_T - X_1(1+\frac{c_1}{c_\beta}))} + \frac{c_1}{c_0}X_1 + \frac{(c_1+d_1)X_1}{a_1(RR_T - X_1(1+\frac{c_1}{c_\beta}))} + X_1 \tag{60}$$

As all terms are monotonically increasing in X_1, therefore **bistability is excluded**.

2.3.2 Topology 2 (monofunctional SK, spontaneous dephosphorylation, dead-end complex)

This topology has a monofunctional SK, and spontaneous dephosphorylation of both SKP and RRP. Moreover, dead-end complex formation between SK and RR is allowed. The *SKP-RR* complex is denoted as X_1, the dead-end complex *SK-RR* as X_2.

The ordinary differential equations are:

$$\begin{aligned}
\dot{SK} &= -c_0 SK + c_\alpha SKP + c_1 X_1 - a_\gamma SK\ RR + d_\gamma X_2 \ (1)\\
\dot{SKP} &= c_0 SK - c_\alpha SKP + d_1 X_1 - a_1 SKP\ RR \ (2)\\
\dot{RRP} &= c_1 X_1 - c_\beta RRP \ (3)\\
\dot{RR} &= d_1 X_1 + c_\beta RRP - a_1 SKP\ RR - a_\gamma SK\ RR + d_\gamma X_2 \ (4)\\
\dot{X_1} &= a_1 SKP\ RR - (d_1 + c_1) X_1 \ (5)\\
\dot{X_2} &= a_\gamma SK\ RR - d_\gamma X_2 \ (6)
\end{aligned} \tag{61}$$

The conservation laws:

$$\begin{aligned} SK_T &= SK + SKP + X_1 + X_2 \\ RR_T &= RR + RRP + X_1 + X_2 \end{aligned} \tag{62}$$

After setting the derivates to 0 for steady state, and variable elimination, I end up with the rational function φ:

$$SK_T = \varphi(X_1) = \alpha X_1 + \beta \frac{(p_1 + p_2 X_1)X_1}{p_3 - p_4 X_1} + \gamma \frac{(p_5 - p_6 X_1)X_1}{p_1 + p_2 X_1} \tag{63}$$

Where $\alpha = (1 + \frac{c_1}{c_0})$, $\beta = (1 + \frac{c_\alpha}{c_0})$ and $\gamma = K_A$, $p_1 = c_\beta c_0$, $p_2 = c_\beta c_1 K_A$, $p_3 = c_0 c_\beta \kappa_1 RR_T$, $p_4 = K_A c_\alpha c_\beta + c_0 \kappa_1 (c_1 + c_\beta)$, $p_5 = \frac{c_\alpha c_\beta}{\kappa_1} + c_1 c_\beta RR_T$, $p_6 = c_1(c_1 + c_\beta)$.

As shown in the Appendix 4.2.1, the first two terms are strictly increasing in X_1, but the last one can have both increasing and decreasing parts, therefore this topology is **capable of bistability**.

I took the derivative of the equation $SK_T = \varphi(X_1)$ (with respect to X_1), which is a rational function, and solved for the roots of the numerator, a (quartic) polynomial equation, and performed parameter sampling in MATLAB. I took those parameter sets where there are more than one roots in the biologically meaningful range, that is, all parameters and total concentrations are positive and the solution for X_1 obeys the conservation laws. For each parameter set, the equation is solved by MATLAB's polynomial solver, the *roots* algorithm. For 10^5 parameter sets, this takes approximately 10 seconds (on a personal computer with a 2.5 GHz processor), several orders of magnitudes faster than solving the initial ODEs in Equation 61. All parameters are generated from lognormal distributions with MATLAB's *lognrnd* algorithm. Numerical parameter sampling confirmed the existence of bistability. I show the relation $SK_T = \varphi(X_1)$ for 30 bistable parameter sets in Figure 27.

These are not traditional bifurcation plots yet, but show the SK_T values where we have bistability. However, from these plots, where SK_T is a dependent variable, we cannot see either the bistability input range λ, or the output range Φ (Figure 25).

One can convert these into 'traditional' bifurcation diagrams (the input parameter c_0 on the x axis and the steady state(s) on the y axis), by choosing a SK_T value where we have three steady states (dotted red lines in Figure 27, drawn at the midpoint of SK_T values with three steady states). I then convert Equation 63 to a polynomial in X_1 and start finding real and positive roots from the initial c_0 value, now c_0 being the independent variable, while all other parameters are fixed, including SK_T. Conservation constraints and the positivity of each species is checked simultaneously.

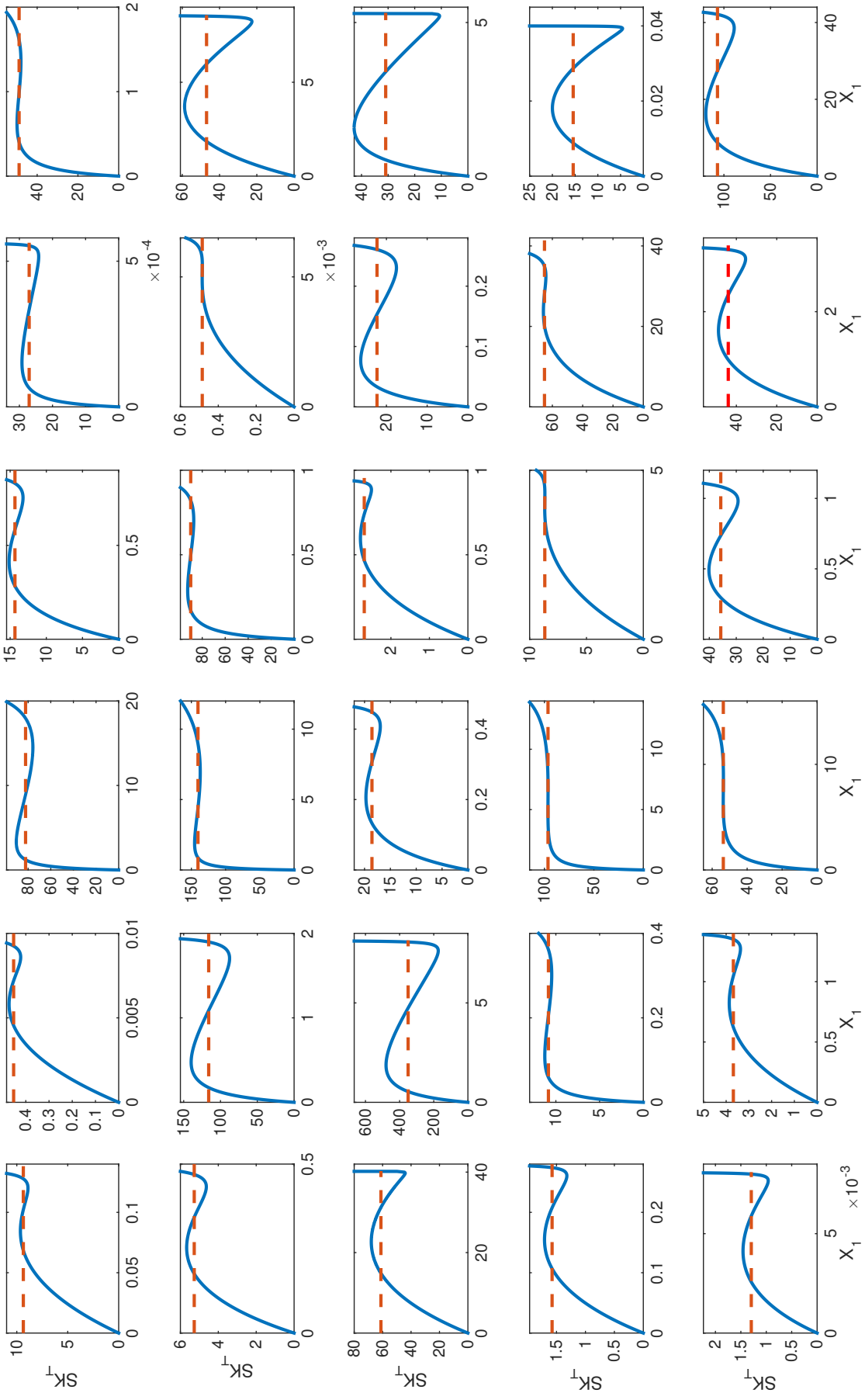

Figure 27. $SK_T = \varphi(X_1)$ relations for 30 randomly chosen parameter sets, for topology 2 (Section 2.3.2).

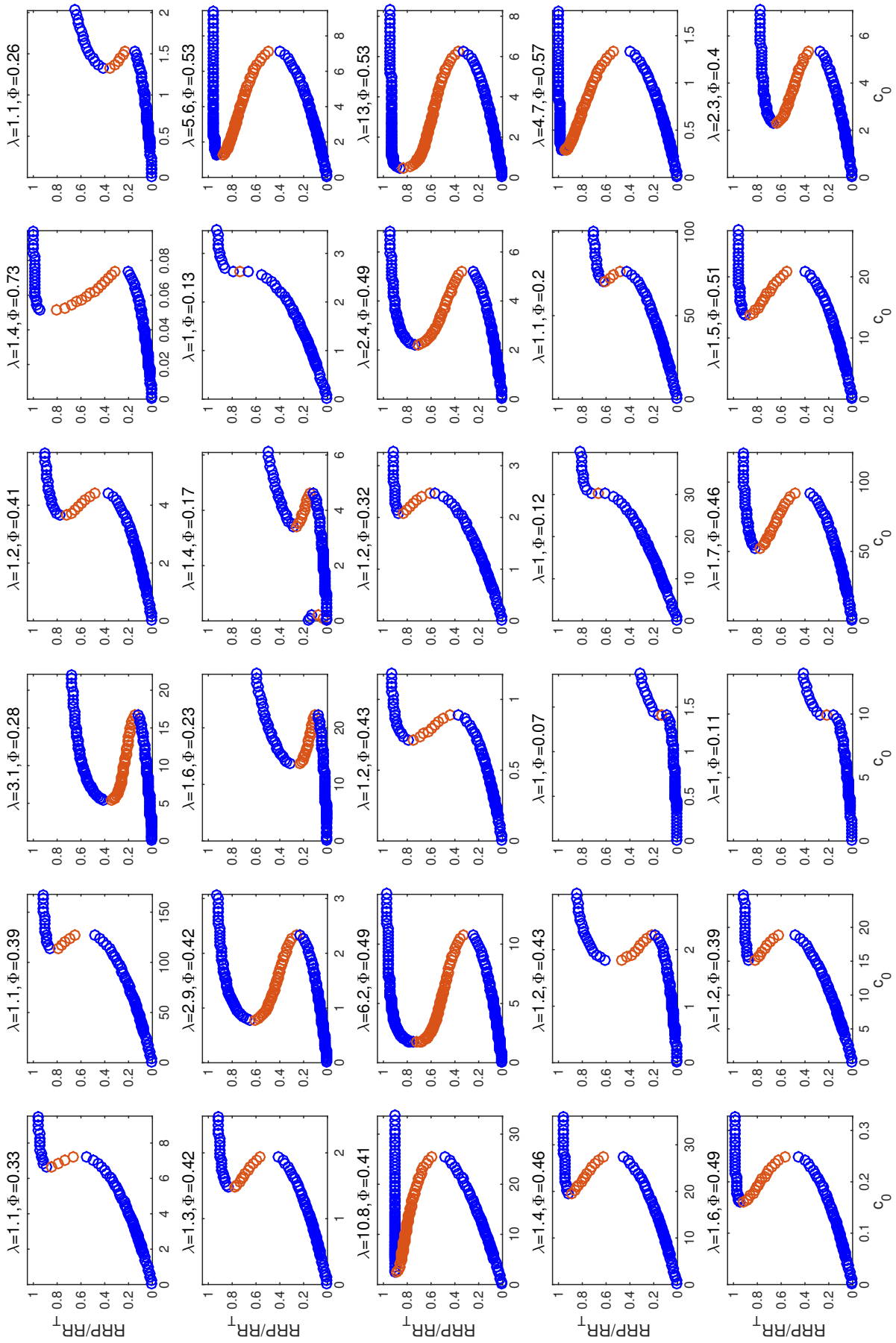

Figure 28. Bifurcation diagrams showing steady states of RRP as a function of c_0, for the same 30 randomly chosen parameter sets as in Figure 27 for Topology 2. Unstable steady states are depicted with red circles. Each plot has its bistability metrics above it, λ and Φ, see Figure 25.

From the derivation we have the output variable RRP expressed as a function of X_1, $RRP = \frac{c_1}{c_\beta} X_1$, and in Figure 28, I plot the solutions for RRP as a function of the input parameter c_0.

I analyzed the distributions of the parameter values for bistable and monostable parameter sets, and calculated the correlation between parameter values and the bistability metrics Φ (bistable output range) and λ (bistable input range), shown in Table 4.

Table 4. Pearson correlation coefficients between parameters and bistability metrics. Asterisk shows if correlation has a p-value larger than 0.01. Sample size: 25523 parameter sets. Strongest correlations in bold.

	K_M	c_α	c_β	SK_T	RR_T	SK_T/RR_T	K_A
λ	-0.01*	-0.01	-0.05	0.05	0.09	-0.04	0.02
Φ	-0.02*	-0.04	**-0.18**	-0.06	-0.01*	**-0.38**	-0.11

I also plotted the distributions of parameter values for mono- and bistable parameter sets in Figure 29. The parameters where the difference is the most marked are again the binding affinity of complex formation K_A, the total RR concentration RR_T and the rate constant for the spontaneous dephosphorylation of RRP.

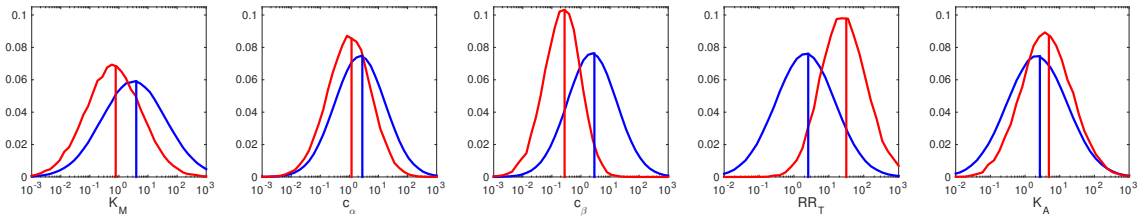

Figure 29. Distributions of parameter values for mono- (blue) and bistable (red) parameter sets, for Topology 2. Vertical line shows the median.

In summary, dead-end complex formation between the unphosphorylated RR and SK and spontaneous dephosphorylation of RRP can already lead to bistable behavior, with the interaction strength for the dead-end complex, the dephosphorylation of RRP and the level and ratio of total concentrations SK_T and RR_T being the key parameters.

2.3.3 Topology 3 (sequestration of SK)

This topology has again a monofunctional SK, spontaneous dephosphorylation of both RRP and SKP. I ask if the reversible binding interaction (sequestration) of the SK with a cellular component external to the TC pathway (denoted E; most plausibly the SK of another TC pathway) can lead to bistability. The inactive complex is denoted as X_2.

The ODEs are:

$$
\begin{aligned}
\dot{SK} &= -c_0 SK + c_\alpha SKP + c_1 X_1 - a_\gamma SK\ E + d_\gamma X_2 \ (1)\\
\dot{SKP} &= c_0 SK - c_\alpha SKP + d_1 X_1 - a_1 SKP\ RR \ (2)\\
R\dot{R}P &= c_1 X_1 - c_\beta RRP \ (3)\\
\dot{RR} &= d_1 X_1 + c_\beta RRP - a_1 SKP\ RR \ (4)\\
\dot{X_1} &= a_1 SKP\ RR - \ (d_1 + c_1) X_1 \ (5)\\
\dot{X_2} &= a_\gamma\ SK\ E - d_\gamma X_2 \ (6)\\
\dot{E} &= -a_\gamma\ SK\ E + d_\gamma X_2 \ (7)
\end{aligned}
\tag{64}
$$

The conservation laws:

$$
\begin{aligned}
SK_T &= SK + SKP + X_1 + X_2\\
RR_T &= RR + RRP + X_1\\
E_T &= E + X_2
\end{aligned}
\tag{65}
$$

After setting the left-hand side of the ODEs to 0, and variable elimination we end up with the rational function φ:

$$
\begin{aligned}
SK_T = \varphi(X_1) = \\
X_1\left(\frac{c_1}{c_0} + \frac{c_\alpha}{c_0\kappa_1[RR_T - X_1(1+\frac{c_1}{c_\beta})]}\right) + \frac{X_1}{\kappa_1[RR_T - X_1(1+\frac{c_1}{c_\beta})]} + X_1 + \\
\frac{E_T K_A X_1[p_1(p_2X_1 - p_3) - p_4]}{p_5(p_2X_1 - p_3) + K_A X_1[p_1(p_2X_1 - p_3) - p_4]}
\end{aligned}
\tag{66}
$$

where $p_1 = c_1\kappa_1, p_2 = c_1 + c_\beta, p_3 = c_\beta RR_T, p_4 = c_\alpha c_\beta, p_5 = c_0\kappa_1$.

The first three terms are increasing in X_1, the more difficult one is the last term, X_2 expressed as a function of X_1 and parameters, written as $f(X_1)$.

Taking the derivative, we get $f'(X_1) = \frac{E_T K_A p_5 p_1 p_2^2 X_1^2 - 2p_1p_2p_3X_1 + p_1p_3^2 + p_3p_4)}{(-K_A p_1 p_2 X_1^2 + K_A p_1 p_3 X_1 + K_A p_4 X_1 - p_2 p_5 X_1 + p_3 p_5)^2}$.

As the denominator is always positive, we have to find the roots of the numerator, which are $S_{+/-} = \frac{p_1p_3 \pm \sqrt{-p_1p_3p_4}}{p_1p_2}$, that is, both roots are complex. At $X_1 = 0$ the value of the function in the numerator is positive, and since the first coefficient is positive as well, the parabola opens upward, therefore the value of the function is always positive.

Since both the denominator and the numerator are positive, $f'(X_1)$ is also always positive. Therefore the last term, $f(X_1)$, in the rational function φ is always increasing and multistationarity is excluded if the function is continuous.

Three (physically possible) steady states at some SK_T value would also be possible if the function has discontinuities in the interval $X_1 \epsilon [0; \frac{p_3}{p_2})$. The first three terms are continuous in this interval, it is only the last one that could have discontinuities, if its denominator equals 0. To have

3 steady states (as in the case of the simplest multistationarity, bistability) in the relevant interval, the denominator has to be zero twice in this interval.

Let us denote the last term as $f(X_1) = \frac{f_1(X_1)}{f_2(X_1)}$, then the denominator $f_2(X_1)$, has to obey $f_2(X_1) = 0$, $X_1 \epsilon [0; \frac{p_3}{p_2})$. But at $X_1 = 0$, $f_2(X_1) = -\frac{p_5}{p_3}$. Moreover for any value $X_1 < \frac{p_3}{p_2}$, the denominator $f_2(X_1) < 0$. That is, $f_2(X_1)$ is always negative and does not have any roots in the interval, therefore the function φ cannot have discontinuities in this interval either. Therefore, **bistability is excluded for this topology**.

2.3.4 Topology 4 (sequestration of RR)

Here I assume the same mechanisms as in Topology 3, but this time it is the RR in its unphosphorylated form that is sequestered by an external component. Notations are analogous to those for Topology 3.

The ODEs are:

$$\begin{aligned}
\dot{SK} &= -c_0 SK + c_\alpha SKP + c_1 X_1 \ (1)\\
\dot{SKP} &= c_0 SK - c_\alpha SKP + d_1 X_1 - a_1 SKP\ RR \ (2)\\
\dot{RRP} &= c_1 X_1 - c_\beta RRP \ (3)\\
\dot{RR} &= d_1 X_1 + c_\beta RRP - a_1 SKP\ RR - a_\gamma RR\ E + d_\gamma X_2 \ (4)\\
\dot{X_1} &= a_1 SKP\ RR - \ (d_1 + c_1) X_1 \ (5)\\
\dot{X_2} &= a_\gamma\ RR\ E - d_\gamma X_2 \ (6)\\
\dot{E} &= -a_\gamma\ RR\ E + d_\gamma X_2 \ (7)
\end{aligned} \tag{67}$$

The conservation laws are:

$$\begin{aligned}
SK_T &= SK + SKP + X_1\\
RR_T &= RR + RRP + X_1 + X_2\\
E_T &= E + X_2
\end{aligned} \tag{68}$$

After setting the left-hand side of the ODEs to 0, and variable elimination we end up with the rational function φ:

$$\begin{aligned}
RR_T = RR + RRP + X_1 + X_2 =\\
\frac{(c_0 + c_\alpha)X_1}{\kappa_1(SK_T - (c_0 + c_1)X_1)} + \frac{c_1}{c_\beta}X_1 + X_1 + \frac{(c_0 + c_\alpha)E_T K_A X_1}{[(c_0 + c_\alpha)K_A - (c_0 + c_1)\kappa_1]X_1 + \kappa_1 SK_T}
\end{aligned} \tag{69}$$

Each term is strictly increasing in X_1, therefore bistability is not possible if the function is

continuous. $X_1 \epsilon [0; \frac{SK_T}{c_0+c_1})$ has to be true for all variables to be positive. In this physically admissible range $X_1 \epsilon [0; \frac{SK_T}{c_0+c_1})$ none of the terms have a discontinuity, as the last term's denominator is linearly increasing with X_1 and has a positive value at both $X_1 = 0$ and $X_1 = \frac{SK_T}{c_0+c_1}$. Therefore, **bistability is excluded for this topology**.

2.3.5 Topology 5 (sequestration of both SK and RR)

For this topology, I assume both the inactive response regulator, RR and the sensor kinase, SK are sequestered by (separate) external components, E_1 and E_2, forming the inactive complexes X_2 and X_3. Notations are analogous to those for Topology 3.

The ODEs are:

$$\begin{aligned}
\dot{SK} &= -c_0 SK + c_\alpha SKP + c_1 X_1 - a_{\gamma 2}\ SK\ E + d_{\gamma 2} X_3 \ (1)\\
\dot{SKP} &= c_0 SK - c_\alpha SKP + d_1 X_1 - a_1 SKP\ RR \ (2)\\
\dot{RRP} &= c_1 X_1 - c_\beta RRP \ (3)\\
\dot{RR} &= d_1 X_1 + c_\beta RRP - a_1 SKP\ RR - a_\gamma RR\ E + d_\gamma X_2 \ (4)\\
\dot{X_1} &= a_1 SKP\ RR - (d_1 + c_1) X_1 \ (5)\\
\dot{X_2} &= a_{\gamma_1}\ RR\ E1 - d_{\gamma_1} X_2 \ (6)\\
\dot{X_3} &= a_{\gamma 2}\ SK\ E2 - d_{\gamma 2} X_3 \ (7)\\
\dot{E1} &= -a_{\gamma_1}\ RR\ E + d_{\gamma_1} X_2 \ (8)\\
\dot{E2} &= -a_{\gamma 2}\ SK\ E + d_{\gamma 2} X_3 \ (9)
\end{aligned} \tag{70}$$

The conservation laws are:

$$\begin{aligned}
SK_T &= SK + SKP + X_1 + X_3\\
RR_T &= RR + RRP + X_1 + X_2\\
E1_T &= E1 + X_2\\
E2_T &= E2 + X_3
\end{aligned} \tag{71}$$

After setting the left-hand side of the ODEs to 0, and variable elimination we end up with the

rational function φ:

$$\begin{aligned} SK_T = \varphi(RR) = SK + SKP + X_1 + X_3 = \\ \frac{1}{1+c_1/c_\beta}\left(\frac{c_1}{c_0}+\frac{c_\alpha}{c_0\kappa_1 RR}\right)\left[RR_T - \frac{RR(1+E1_T K_{a_1}+K_{a_1}RR)}{1+K_{a_1}RR}\right] \\ +\frac{1}{(1+c_1/c_\beta)\kappa_1 RR}\left[RR_T - \frac{RR(1+E1_T K_{a_1}+K_{a_1}RR)}{1+K_{a_1}RR}\right] \\ +\frac{1}{1+c_1/c_\beta}\left[RR_T - \frac{RR(1+E1_T K_{a_1}+K_{a_1}RR)}{1+K_{a_1}RR}\right] \\ +K_{A3}\frac{E2_T}{1/\phi(RR)+K_{A3}} \end{aligned} \tag{72}$$

Where $\phi(RR) = SK = \frac{1}{1+c_1/c_\beta}\left(\frac{c_1}{c_0}+\frac{c_\alpha}{c_0\kappa_1 RR}\right)\left[RR_T - \frac{RR(1+E1_T K_{a_1}+K_{a_1}RR)}{1+K_{a_1}RR}\right]$.

All terms are strictly decreasing in RR, as shown in the Appendix, therefore **bistability is excluded for this topology**. The function does not have discontinuities if $RR > 0$, because there are no negative terms in the denominators.

2.3.6 Topology 6 (dead-end complex, independent phosphatase)

Here I assume, that besides spontaneous dephosphorylation of RRP molecules, there is an independent phosphatase (as in some phosphorelays) dephosphorylating them and that the inactive SK and RR can form a dead-end complex X_2. This topology has already been analyzed and demonstrated to exhibit bistability numerically [72]. Here, I simplify the system to one equation and explore it further.

The ODEs are:

$$\begin{aligned} \dot{SK} &= -c_0 SK + c_\alpha SKP + c_1 X_1 - a_\gamma\ SK\ RR + d_\gamma X_2 \ (1) \\ \dot{SKP} &= c_0 SK - c_\alpha SKP + d_1 X_1 - a_1 SKP\ RR \ (2) \\ \dot{RRP} &= c_1 X_1 - c_\beta RRP - a_2\ RRP\ F + d_2 X_3 \ (3) \\ \dot{RR} &= d_1 X_1 + c_\beta RRP - a_1 SKP\ RR - a_\gamma RR\ SK + d_\gamma X_2 + c_2 X_3 \ (4) \\ \dot{X_1} &= a_1 SKP\ RR - \ (d_1+c_1)X_1 \ (5) \\ \dot{X_2} &= a_\gamma\ RR\ SK - d_\gamma X_2 \ (6) \\ \dot{X_3} &= a_2\ RRP\ F - \ (d_2+c_2)X_3 \ (7) \\ \dot{F} &= -a_2\ RRP\ F + \ (d_2+c_2)X_3 \ (8) \end{aligned} \tag{73}$$

The conservation laws are:

$$\begin{aligned} SK_T &= SK + SKP + X_1 + X_2 \\ RR_T &= RR + RRP + X_1 + X_2 + X_3 \\ F_T &= F + X_3 \end{aligned} \tag{74}$$

After setting the left-hand side of the ODEs to 0, and variable elimination we end up with the rational function φ:

$$\begin{aligned} SK_T = \varphi(RRP) = SK + SKP + X_1 + X_2 = \\ -RRP\frac{\mathrm{RRP}^3\kappa_2^2 K_A c_\beta^2 + \mathrm{RRP}^2 p_8 + \mathrm{RRP} p_9 + c_0\left(c_\beta + c_2\kappa_2 F_T\right)}{p_1\mathrm{RRP}^3 + p_2\mathrm{RRP}^2 + p_3\mathrm{RRP} - c_0 c_1\kappa_1\mathrm{RR}_T} \\ +RRP\frac{p_4\mathrm{RRP}^3 + p_5\mathrm{RRP}^2 + p_6\mathrm{RRP} - p_7}{p_1\mathrm{RRP}^3 + p_2\mathrm{RRP}^2 + p_3\mathrm{RRP} - c_0 c_1\kappa_1\mathrm{RRT}} \\ +\frac{\mathrm{RRP}}{c_1}\left(c_\beta + \frac{\left(c_2\kappa_2\right)F_T}{\kappa_2\mathrm{RRP}+1}\right) \\ +\left(-K_A\mathrm{RRP}\frac{\left(p_4\mathrm{RRP}^3 + p_5\mathrm{RRP}^2 + p_6\mathrm{RRP} - p_7\right)}{c_1\kappa_1[\mathrm{RRP}^3\kappa_2^2 K_A c_\beta + \mathrm{RRP}^2 p_{10} + \mathrm{RRP} p_{11} + c_0]}\right) \end{aligned} \tag{75}$$

These rational functions have high order polynomials in both their denominator and numerator, and their sum can have both increasing and decreasing parts, making **this topology capable of bistability**, as shown in the Appendix. $p_i, i = 1..11$ are lumped parameters of kinetic constants and total concentrations.

To generate bistable parameter sets, I performed numerical sampling for the parameters c_0, c_α, a_1, d_1, c_1, a_γ, d_γ, a_2, d_2, c_2 and RR_T and solved the equation $\varphi(RRP)' = 0$ numerically. If the equation has multiple solutions $RRP \in [0, RR_T]$, then in some range of SK_T values the given parameter set exhibits multistationarity, because the function has critical points in that range. Taking these parameter sets we can, as for Topology 2, calculate the $SK_T = \varphi(RRP)$ curve (compare the curves in Figure 27), and select a SK_T value. At this value of SK_T, the bifurcation diagram showing RRP steady states as a function of the input parameter c_0 can be generated.

I analyzed the distributions of the parameter values for bistable and monostable parameter sets, and the correlations between parameter values and the bistability metrics Φ (bistable output range) and λ (bistable input range), the results shown in Table 5, and some sample bifurcation diagrams in Figure 30.

Table 5. Pearson correlation coefficients between parameters and bistability metrics. Asterisk shows if correlation has a p-value larger than 0.01. Sample size: 13200 bistable parameter sets. Strongest correlations in bold.

	K_{M1}	K_{M2}	c_α	c_β	RR_T	SK_T	SK_T/RR_T	F_T	K_A
λ	-0.04	-0.06	**0.16**	-0.01	0.01	0.06	**0.22**	0	-0.03
Φ	-0.1	**-0.15**	-0.01	0	-0.06	**-0.15**	0.2	-0.01	-0.01

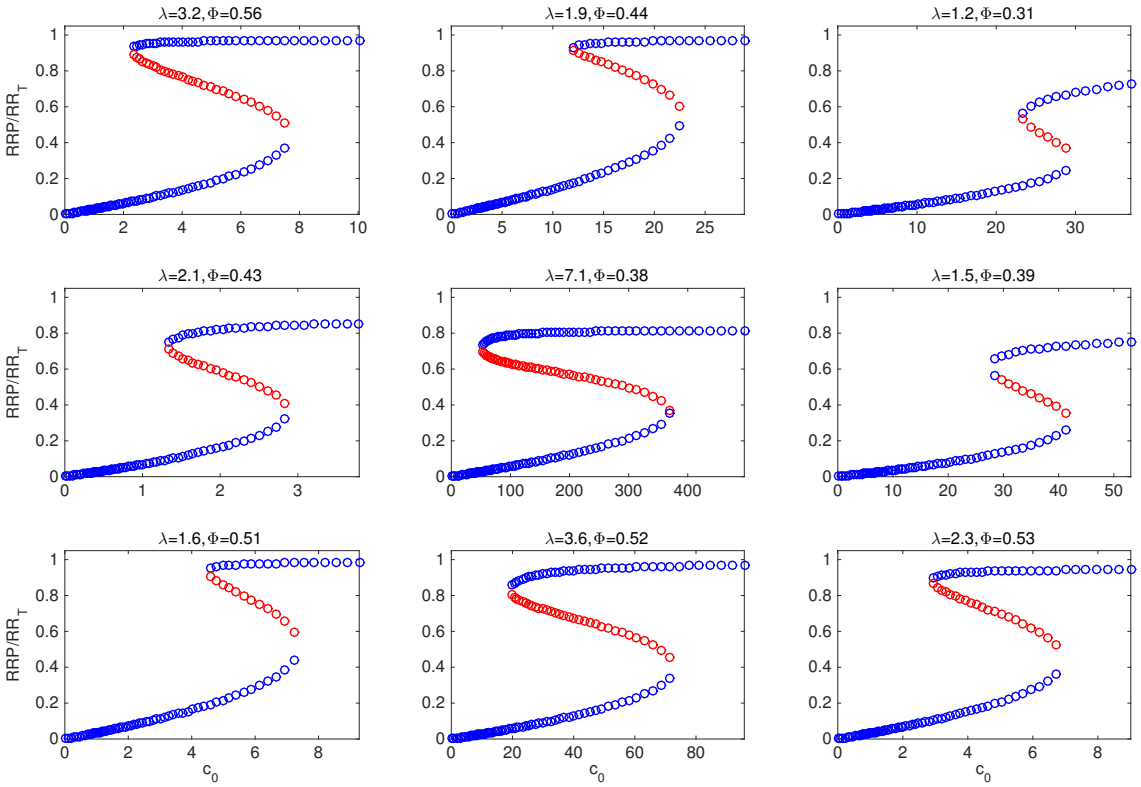

Figure 30. Bifurcation diagrams showing steady states of RRP as a function of c_0, for 9 randomly chosen parameter sets of Topology 6 (2.3.6). Unstable steady states are depicted with red circles. Each plot has its bistability metrics above it, λ and Φ.

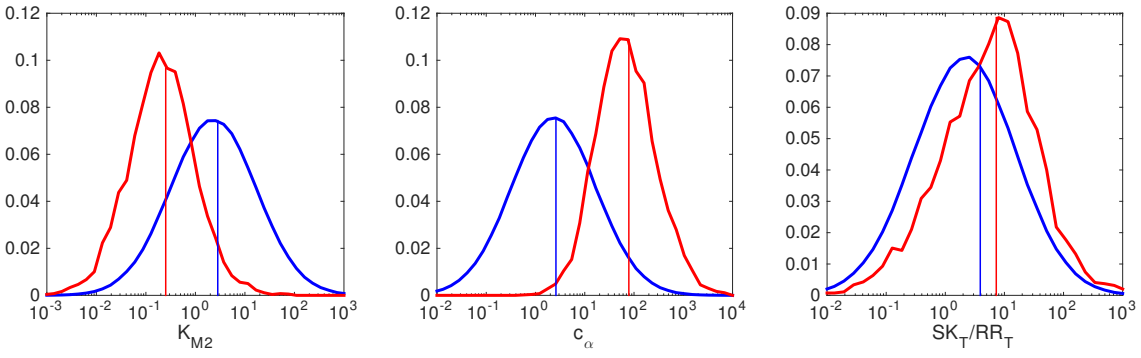

Figure 31. Distributions of parameter values for mono- (blue) and bistable (red) parameter sets, for Topology 6. Vertical line shows the median.

The rate constant of spontaneous dephosphorylation of SKP, the K_M of phosphatase-driven

dephosphorylation and the ratio of total concentrations SK_T to RR_T show the strongest correlations with the bistability metrics. In particular, a higher SK_T/RR_T ratio expands the input and output range of bistability as well. The different distributions of these parameters for mono- and bistable parameter sets, respectively, are shown in Figure 31.

2.3.7 Topology 7 (split kinase)

As analyzed in [4], in some bacterial TC systems there is a secondary SK ($SK2$) binding to the main SK ($SK1$), that is necessary for the autophosphorylation of SK1. As this kinase-kinase complex is not capable of dephosphorylating response regulators, strong nonlinearities can arise due to competition effects. The output species of the topology, RRP, is dephosphorylated by the main SK, $SK1$. In the case of this TC system, we can treat the catalytic constant c_3 of the (auto)phoshorylation rate of the $SK1.SK2$ complex as the input parameter that changes as a function of ligand concentration. The intermediate complexes are: $X_1 = SK1P.RR$, $X_2 = SK1.RRP$, $X_3 = SK1.SK2$.

The ODEs describing this topology are:

$$\begin{aligned}
\dot{SK1} &= c_\alpha SK1P - a_3 SK1\ SK2 + d_3 X_3 + c_1 X_1 - a_2 SK1\ RRP + (d_2 + c_2) X_2 \quad (1)\\
\dot{SK1P} &= -c_\alpha SK1P + c_3 X_3 - a_1 SK1P\ RR + d_1 X_1 \quad (2)\\
\dot{RR} &= -a_1 SK1P\ RR + d_1 X_1 + c_2 X_2 + c_\beta RRP \quad (3)\\
\dot{RRP} &= c_1 X_1 - a_2 SK1\ RRP + d_2 X_2 - c_\beta RRP \quad (4)\\
\dot{X_1} &= a_1 SK1P\ RR - (d_1 + c_1) X_1 \quad (5)\\
\dot{X_2} &= a_2 SK1\ RRP - (d_2 + c_2) X_2 \quad (6)\\
\dot{SK2} &= -a_3 SK1\ SK2 + (d_3 + c_3) X_3 \quad (7)\\
\dot{X_3} &= a_3 SK1\ SK2 - (d_3 + c_3) X_3 \quad (8)
\end{aligned} \tag{76}$$

The conservation laws are:

$$\begin{aligned}
SK1_T &= SK1 + SK1P + X_1 + X_2 + X_3\\
RR_T &= RR + RRP + X_1 + X_2\\
SK2_T &= SK2 + X_3
\end{aligned} \tag{77}$$

After setting the left-hand side of ODEs to 0, and variable elimination we can express all variables as functions of $SK1$:

$RRP = \frac{c_1 \kappa_3 c_\alpha SK1^2 + p_1 SK1 - c_1 c_\alpha \mathrm{SK1}_T}{p_2 SK1^2 + p_3 SK1 + p_4}$

$$RR = \frac{-c_2\kappa_2\kappa_3 c_\alpha SK1^3 + p_5 SK1^2 + p_6 SK1 + c_\alpha c_\beta SK1_T}{c_1 c_2 \kappa_1 \kappa_2 \kappa_3 SK1^3 + p_7 SK1^2 + p_8 SK1 - c_1\kappa_1 c_\beta SK1_T}$$

$$X_1 = \frac{c_2\kappa_2\kappa_3 c_\alpha SK1^3 - p_5 SK1^2 - p_6 SK1 - c_\alpha c_\beta SK1_T}{p_2 SK1^2 + p_3 SK1 + p_4}$$

$$X_2 = \kappa_2 \mathrm{SK}_1 \frac{c_1\kappa_3 c_\alpha \mathrm{SK}_1^2 + p_1 \mathrm{SK}_1 - c_1 c_\alpha \mathrm{SK1}_T}{p_2 \mathrm{SK}_1^2 + p_3 \mathrm{SK}_1 + p_4}$$

and the rational function φ is a sum of these:

$$RR_T = \varphi(SK1) = RR + RRP + X_1 + X_2 \tag{78}$$

Where p_i, *i=1..8* are again lumped parameters. As shown in the Appendix and by numerical parameter sampling below, φ can have increasing and decreasing parts, and therefore **this topology is capable of bistability**. Sample bifurcation plots are shown in Figure 32.

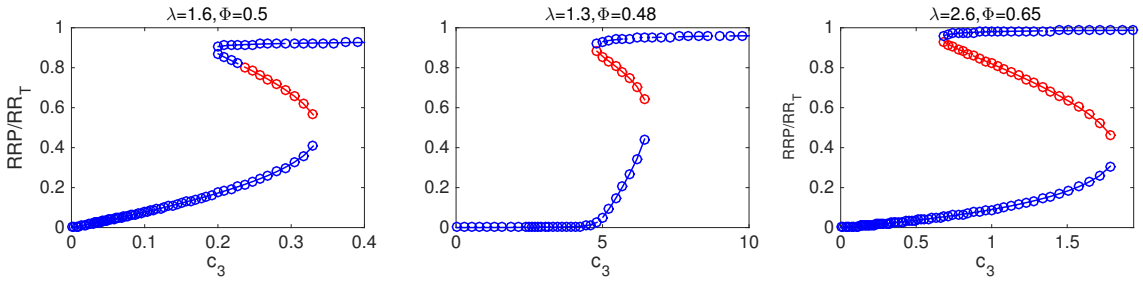

Figure 32. Bifurcation diagrams showing steady states of RRP as a function of c_3, for 9 randomly chosen parameter sets of Topology 7 (2.3.7). Unstable steady states are depicted with red circles. Each plot has its bistability metrics above it, λ and Φ.

Parameter analysis shows marked differences in some parameter values, shown by the histograms in Figure 33. Specifically, bistable parameter sets have higher absolute levels of the SKs ($SK1$ and $SK2$), a higher ratio of $SK1$ to $SK2$, and a stronger interaction between them ($K_d = a_3/d_3$). This is intuitive, as the interaction between the two SKs competes with the dephosphorylation of RRP, constituting the mechanism behind bistable behavior. At the same time, spontaneous dephosphorylation of $SK1P$ or RRP (rate constants c_α and c_β) works against bistability.

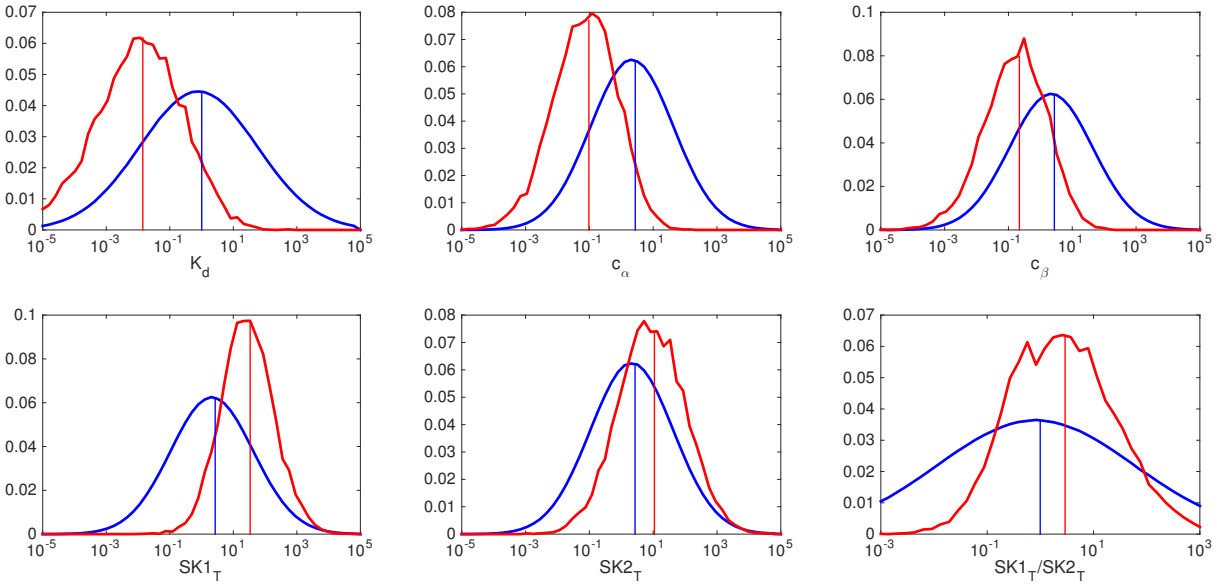

Figure 33. Distributions of parameter values for mono- (blue) and bistable (red) parameter sets, for Topology 7. Vertical line shows the median.

2.4 Transcriptional feedback leading to bistability in TC systems

Most TC systems are auto-inducing, with pathway activation inducing the expression of the same pathway's components, constituting a positive feedback loop [122, 156, 158]. Therefore, bistability could also be caused by transcriptional regulation, and the interaction between post-translational mechanisms and the transcriptionally-regulated production of the pathway's species has to be taken into account.

It is intuitive that if the transcriptional positive feedback is on a monofunctional SK, this makes bistability possible, as the production curve of SK (and RR) is a non-linear (sigmoidal, see Appendix 4.3) function of RRP due to the dimerization of RRP molecules and because a monofunctional SK is an activator of RRP, making the sign of the feedback positive. These two criteria, sigmoidality of feedback induction and positive sign of the feedback, is sufficient for bistability [6, 7].

In the case of a bifunctional SK however, that both activates and deactivates the RR molecule, it is less clear what the effect of the induction would be and whether it can lead to bistability. A number of publications illustrated the possibility of bistability in TC systems with a bifunctional SK [77, 156, 169], but under special conditions. In [156], a second (parallel) feedback loop is present besides the direct self-induction of SK and RR, and this additional feedback loop is strongly non-linear, enabling bistability. Therefore, the topology under investigation is more complex than the core TC topology. In [77] only one parameter set is analyzed and the feedback loop is only on

RR, not SK.

Below, I investigate the core TC topology with a bifunctional SK and auto-induction of both pathway components by algebraically reducing it to a single equation and then applying extensive parameter sampling to find bistable parameter sets. The structure of the system is illustrated in Figure 34.

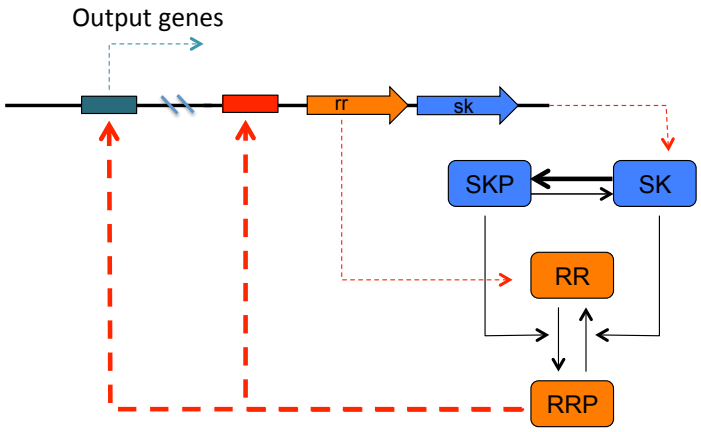

Figure 34. Auto-induction in the canonical TC system topology with a bifunctional SK.

To describe the system with transcriptional induction and degradation, I use a Hill-equation with a cooperativity index of two, to model the effect of dimerization of the activated transcription factor, RRP. In the Appendix, I show that using a quadratic Hill-function instead of explicit modeling of dimerization is legitimate. The degradation of species is modeled as a linear (first-order) process. The degradation terms can be thought of as a combination of protein degradation and the dilution of components due to cell growth. Growth-rate dependence of the degradation rates themselves [39, 148] is not considered here. mRNA molecules are not represented separately, instead the concentration of RRP directly regulates the production rate of RR and SK as:

$$\begin{aligned} v_{prod}(SK) &= \beta + \phi \frac{RRP^2}{RRP^2 + \theta^2} \\ v_{prod}(RR) &= \lambda \left(\beta + \phi \frac{RRP^2}{RRP^2 + \theta^2} \right) \end{aligned} \tag{79}$$

As SK and RR are in most cases co-transcribed from one autoregulated operon [156], the dependency of the production rate on RRP is set to be identical. Differences in mRNA processing however result in different copy numbers, typically 10-100-fold higher copy numbers for response regulators. This is captured by the scaling parameter λ, defining the RR_T to SK_T ratio. β is the basal production rate from the operon, ϕ the maximal induced rate of production, and θ is

the concentration of the activated transcription factor (RRP) at which the production rate is half-maximal.

The full system of equations for the bifunctional TC with transcriptional feedback and degradation of each species is then:

$$\begin{aligned}
\dot{SK} &= \left(\beta + \phi\frac{RRP^2}{RRP^2+\theta^2} - \gamma SK\right) - c_0 SK - a_2 SK\ RRP + (c_2+d_2)X_2 + c_1 X_1 \\
\dot{RR} &= \left(\lambda\left(\beta + \phi\frac{RRP^2}{RRP^2+\theta^2}\right) - \gamma RR\right) - a_1 SKP\ RR + d_1 X_1 + c_2 X_2 \\
\dot{X_1} &= -\gamma X_1 + a_1 SKP\ RR - (d_1+c_1)X_1 \\
\dot{X_2} &= -\gamma X_2 + a_2 SK\ RRP - (d_2+c_2)X_2 \\
\dot{RRP} &= -\gamma RRP - a_2 SK\ RRP + d_2 X_2 + c_1 X_1 \\
\dot{SKP} &= -\gamma SKP - a_1 SKP\ RR + d_1 X_1 + c_0 SK
\end{aligned} \tag{80}$$

Due to the production and degradation (with γ the first-order rate constant) of species, there are no such conserved quantities as total concentrations (SK_T and RR_T) when considering post-translational mechanisms only. Setting the left-hand side of the ODEs to 0, and making use of the fact that in steady state, the inflow and outflow of phosphate groups has to be equal, one can reduce the system to an equation in one variable, RRP. This equation is an algebraic relation, where we have the input parameter c_0 on the left-hand side of the equation and a rational function in the steady state value of RRP on the right, $f(RRP)$. This is an inverted bifurcation diagram, as c_0 (which is on the y-axis) is the input parameter. For the core TC topology with a bifunctional SK, this relation is:

$$c_0 = \frac{\mathrm{RRP}\left(c_2\left(a_2\left(\beta\theta+\mathrm{RRP}^2(\beta+\phi)\right)+\gamma^2\left(\theta+\mathrm{RRP}^2\right)\right)+\gamma^2 d_2\left(\theta+\mathrm{RRP}^2\right)\right)\left(c_1\left(a_1\left(-\beta\theta\lambda+\gamma\mathrm{RRP}^3-\lambda\mathrm{RRP}^2(\beta+\phi)+\gamma\theta\mathrm{RRP}\right)-\gamma^2\left(\theta+\mathrm{RRP}^2\right)\right)-\gamma^2 d_1\left(\theta+\mathrm{RRP}^2\right)\right)}{(c_2+d_2)\left(c_1\left(a_1(\beta\theta+\mathrm{RRP}^2(\beta+\phi))(-\beta\theta\lambda+\gamma\mathrm{RRP}^3-\lambda\mathrm{RRP}^2(\beta+\phi)+\gamma\theta\mathrm{RRP})+\gamma^3\mathrm{RRP}(\theta+\mathrm{RRP}^2)^2\right)+\gamma^3 d_1\mathrm{RRP}(\theta+\mathrm{RRP}^2)^2\right)} \tag{81}$$

Or, converting the numerator and denominator both into polynomial form:

$$c_0 = \frac{RRP\left(\sum_{i=0}^{5} a_i RRP^i\right)}{\sum_{j=0}^{5} b_j RRP^j} \tag{82}$$

where the coefficients are:

$$p_0 = -\theta^2\left(c_2\left(a_2\beta+\gamma^2\right)+\gamma^2 d_2\right)\left(c_1\left(a_1\beta\lambda+\gamma^2\right)+\gamma^2 d_1\right)$$

$$p_1 = a_1\gamma c_1\theta^2\left(c_2\left(a_2\beta+\gamma^2\right)+\gamma^2 d_2\right)$$

$$p_2 = -\theta(c_1(c_2(a_1\lambda(2a_2\beta(\beta+\phi)+\gamma^2(2\beta+\phi))+\gamma^2$$

$(a_2(2\beta+\phi)+2\gamma^2))+\gamma^2 d_2(a_1\lambda(2\beta+\phi)+2\gamma^2))+\gamma^2 d_1(c_2(a_2(2\beta+\phi)+2\gamma^2)+2\gamma^2 d_2))$

$p_3 = a_1\gamma c_1\theta\left(c_2\left(a_2(2\beta+\phi)+2\gamma^2\right)+2\gamma^2 d_2\right)$

$p_4 = \left(c_2\left(a_2(\beta+\phi)+\gamma^2\right)+\gamma^2 d_2\right)\left(-\left(c_1\left(a_1\lambda(\beta+\phi)+\gamma^2\right)+\gamma^2 d_1\right)\right)$

$p_5 = a_1\gamma c_1\left(c_2\left(a_2(\beta+\phi)+\gamma^2\right)+\gamma^2 d_2\right)$

and

$r_0 = a_1\left(-\beta^2\right)c_1\theta^2\lambda\left(c_2+d_2\right)$

$r_1 = \gamma\theta^2\left(c_2+d_2\right)\left(c_1\left(a_1\beta+\gamma^2\right)+\gamma^2 d_1\right)$

$r_2 = -2a_1\beta c_1\theta\lambda(\beta+\phi)\left(c_2+d_2\right)$

$r_3 = \gamma\theta\left(c_2+d_2\right)\left(c_1\left(a_1(2\beta+\phi)+2\gamma^2\right)+2\gamma^2 d_1\right)$

$r_4 = a_1c_1(-\lambda)(\beta+\phi)^2\left(c_2+d_2\right)$

$r_5 = \gamma\left(c_2+d_2\right)\left(c_1\left(a_1(\beta+\phi)+\gamma^2\right)+\gamma^2 d_1\right).$

For the topology to be capable of bistability, there has to be some c_0 value where $c_0 = f(RRP(1)) = f(RRP(2)) = f(RRP(3))$, and $RRP(1) \neq RRP(2) \neq RRP(3)$ are both true. For these conditions to be satisfied, the function $f(RRP)$ has to have two critical points, that is, the derivative of $f(RRP)$ has to have two biologically meaningful roots. To search for such parameter sets, I take the derivative of $f(RRP)$, which is also a rational function that is the ratio of two polynomials, and look for roots of the numerator while performing parameter sampling. Parameters are randomly generated numbers from lognormal distributions, with the properties shown in Table 6. The parameters are centred around biochemically realistic values and are defined in such a way that the total concentration of pathway components are in the $nM - \mu M$ range, as reported in the literature.

Table 6. Unit and median of the randomly generated parameter values for the canonical TC topology with transcriptional induction. Every parameter is generated from a lognormal distribution with a standard deviation of 2.

Parameters	Unit	Logarithm of median
a_1, a_2	$(\mu M min)^{-1}$	2.5
d_1, d_2	min^{-1}	2.5
c_1, c_2	min^{-1}	2.5
γ	min^{-1}	-2
β	$\mu M/min$	-2
Φ	$\mu M/min$	-2
θ	μM	-2
λ	unitless	2

Physically unfeasible bifurcation plots are discarded, e.g. if the lower branch of steady states extends to the right indefinitely. I have also discarded parameter sets where there is nominal bistability, but the two bistability metrics have very low values, specifically if $\lambda < 2$ or $\Phi < 0.1$.

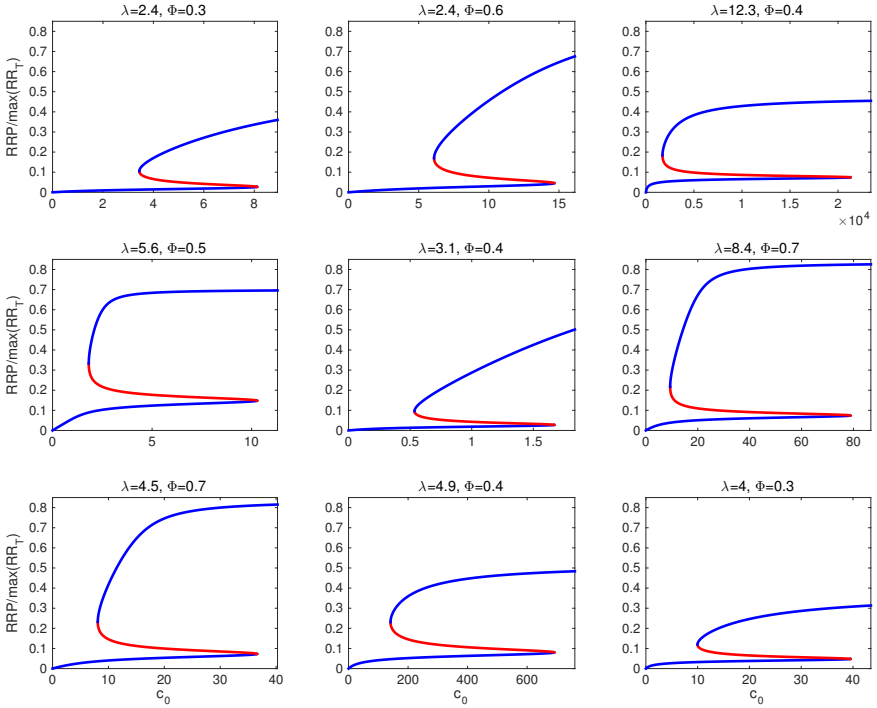

Figure 35. Bifurcation diagrams for the transcriptionally auto-regulating core TC topology, with a biunctional SK. Each plot has its bistability metrics above it, λ and Φ. Unstable steady states in red.

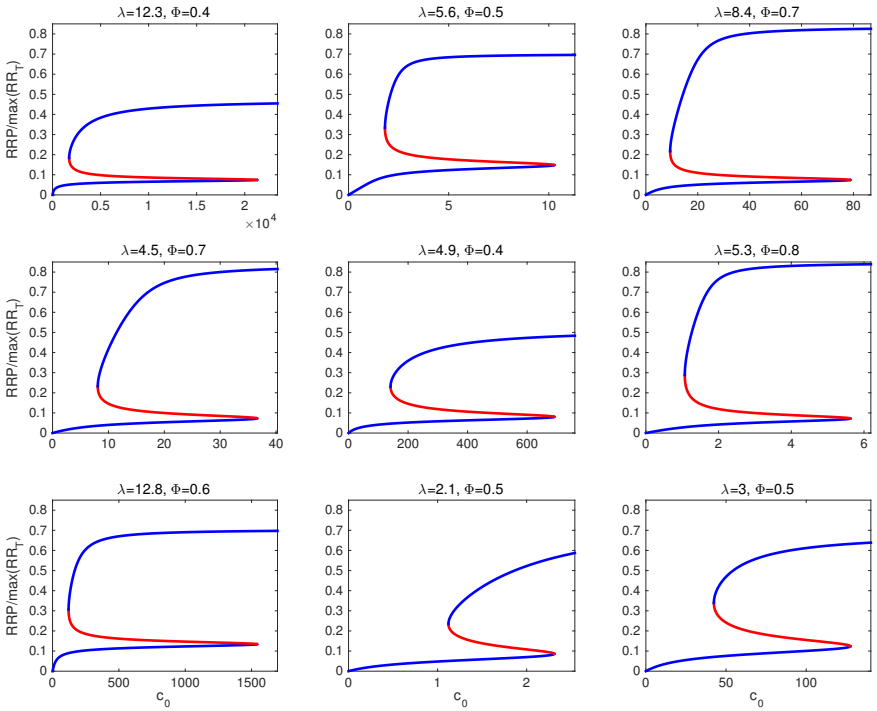

Figure 36. Bifurcation diagrams for the transcriptionally auto-regulating core TC topology, with a bifunctional SK. Solutions shown where the first bifurcation point is at $RRP/max(RR_T) > 0.05$. Each plot has its bistability metrics above it, λ and Φ. Unstable steady states in red.

Φ is now defined slightly differently, than in Figure 25: it is the difference between the value of the output variable at the bifurcation point x_2 and the value of the upper branch at the same x value. The bifurcation plots of some sample bistable parameter sets are shown in Figure 35. As we can see, for many of the bistable systems the lower branch of solutions is at a very low value, which means that the system is barely induced, i.e. there is only very low expression of RR and SK. This means that the system works as an all-or-none bistable switch. By filtering out solutions where at the bifurcation point for the lower branch of solutions (x_2 in Figure 25) $RRP/max(RR_T) < 0.05$, we can see that there are also parameter sets where the system is already significantly induced before the bifurcation occurs, as shown in Figure 36. As a last step, some bistable parameter sets were selected and the original system of ODEs was re-simulated from two different initial values of expression levels (but at the same value of the input parameter c_0) to show bistability in the dynamical behavior of the system, shown of Figure 38.

Turning to the analysis of parameters now, the results of the parameter scan highlight five biologically meaningful parameters that have significantly different values in the case of bistable parameter sets:

- **basal expression level**, β: the median value of β for (strongly) bistable parameter sets is significantly *lower* than for all parameter sets.

- **fold change of induction**, Φ/β: the median value of Φ/β for (strongly) bistable parameter sets is significantly *higher* than for all parameter sets.

- the **maximal amount of pathway components** SK_T ($\frac{\beta+\phi}{\gamma}$) and RR_T ($\lambda\frac{\beta+\phi}{\gamma}$): both are significantly *lower* for (strongly) bistable parameter sets than for the entire parameter set.

- **EC_{50} of transcriptional induction** as a fraction of maximal amount of RR_T, $\frac{\theta}{max(RR_T)}$: the median value for (strongly) bistable parameter sets is significantly *higher* than for all parameter sets.

To summarize, we can see that bistability due to transcriptional auto-induction is indeed possible in the minimal TC topology with a bifunctional SK. I found that bistable systems typically have lower copy numbers, a lower basal expression level, a higher fold change and a higher EC_{50} (relative to the maximal expression level of RR_T) of transcriptional induction.

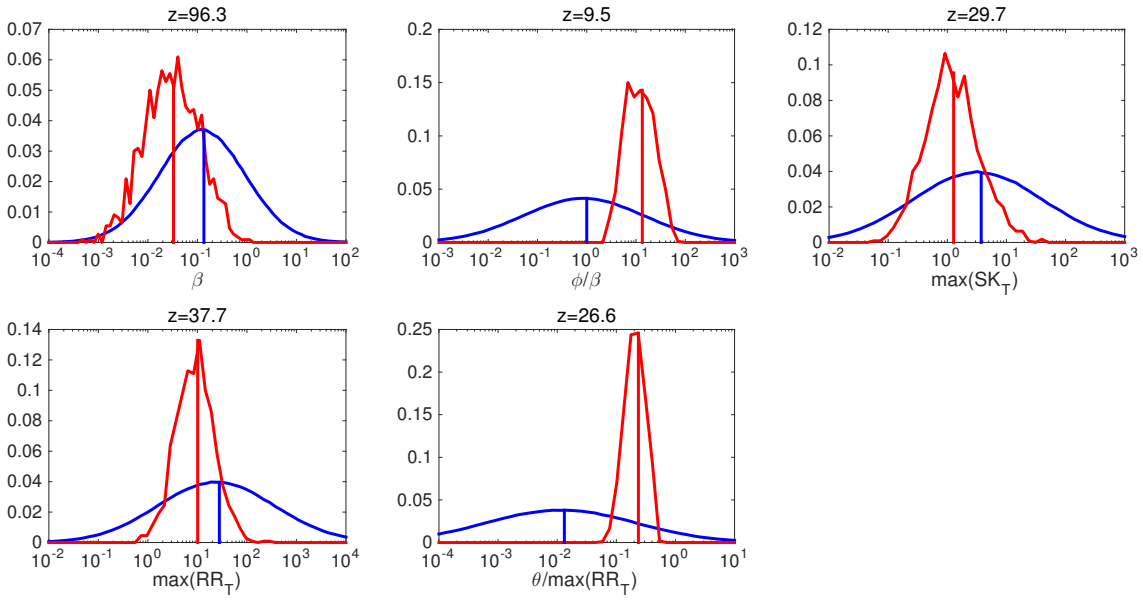

Figure 37. Parameter histograms. The value above the subplots is the z-score quantifying how significant the difference is between the two distributions, $z = \frac{\mu_1 - \mu_2}{\sqrt{\frac{\sigma_1^2}{\sqrt{n_1}} - \frac{\sigma_2^2}{\sqrt{n_2}}}}$. The blue curves are the histograms for the total parameter scan of 10^6 parameter sets, the red curves are for the 1028 strongly bistable parameter sets, as defined in the text ($\lambda > 2$ and $\Phi > 0.1$).

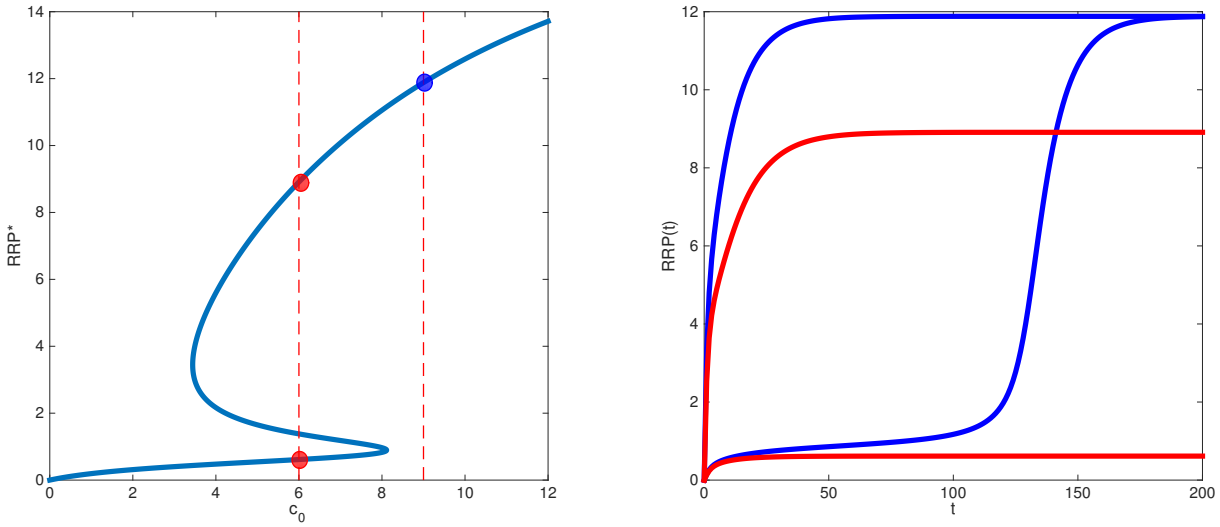

Figure 38. Resimulation of a sample bistable system with the full system of ODEs. On the left panel is the bifurcation diagram of a sample bistable system. I select two values of c_0. One is within the bistable range with two stable steady states ($c_0 = 6$, red circles). For the other value of $c_0 = 9$ the system has only one steady state (blue circle). On the right panel are dynamic simulations of the original system of ODEs at the two selected c_0 values. For the c_0 value within the bistable range the system can converge to two different steady states (red curves), depending on whether its initial condition is the basal expression level of SK and RR, or the maximal induction level. In the case of $c_0 = 9$, the system converges to the same (unique) steady state irrespective of its initial condition, albeit with different dynamics.

2.5 Conclusions

I looked at post-translational mechanisms and the auto-inducing transcriptional feedback loop present in many TC systems to see if they are capable of generating bistable behavior. Bistability for TC systems that control developmental transitions might be needed for different reasons. On the one hand they can be required for an irreversible shift to occur in the expression level of the controlled genes at a single-cell level. Through the same process, at a population level bistable control systems can generate two distinct subpopulations with different means of expression levels. This can be an advantageous strategy for a population in a fluctuating, unpredictable environment (bet-hedging).

I analyzed TC systems in two frameworks, first considering only post-translational mechanisms, with fixed total concentrations. In the second, more realistic approximation I also include degradation of species and their transcriptional auto-induction.

In the first approximation, looking at post-translational interactions only, one mechanism that enables bistability is complex formation between inactive pathway components coupled with a SK-independent dephosphorylation route. Another is split SKs, already analyzed in an article [4]. Following numerical sampling I looked at parameter distributions of bistable and monostable systems and highlighted the key parameters for the existence of bistability.

In the second approximation, I showed conclusively that the minimal TC system with transcriptional auto-induction can indeed be bistable. Furthermore, by analyzing the distributions of parameter values for mono- and bistable parameter sets, I identified parametric properties of transcriptionally induced bistability. Transcriptionally bistable TC systems have a low basal expression level, a high fold change of transcriptional induction and a higher relative EC_{50} of transcriptional induction.

The above analysis can be extended in a number of directions. First, the models above can be converted into stochastic ones, exploring the effects of bistability at a population level. Second, by analysis of the coefficients of polynomial equations that I obtained for each system, one might derive inequalities between parameters that have to be fulfilled for bistability. Third, the dimerization of RRPs and their binding to a promoter site can be explicitly modeled, as well as transcription and translation as separate processes. Fourth, the transient behavior of bistable systems could also be analyzed in more detail. Finally, the parametric conditions derived for transcriptionally induced bistability are potentially amenable for experimental implementation, such as a higher EC_{50} of expression, a higher fold change or a lower basal level of expression. By following these criteria, engineering a monostable TC system into a bistable one might be experimentally feasible.

3 Microbial motility: increased directional persistence by lateral flagellation

3.1 Introduction: bacterial motility and chemotaxis

Any organism that is able to actively explore and exploit the resources of its environment has a major advantage over its competitors. Therefore, it is no surprise that in evolution, we see the emergence of the capacity for motility and in particular directed movement already in the simplest organisms, that is, bacteria [76, 88]. Most bacterial species navigate their environment by a so-called random walk [15, 16], a process that is the succession of random steps. The common organelle for locomotion in bacteria are flagella, consisting of long protein filaments protruding from the cell's surface and rotated by a membrane-embedded motor. A bacterial random walk consists of straight runs (perturbed by rotational diffusion to some extent) and reorientations of the cell. Without chemical gradients that bacteria can detect, the process of random walks results in uniform spreading. Many bacterial species however evolved a chemotactic apparatus to detect gradients of nutrients (attactants) or toxic compounds (repellents), making it possible to actively seek out and exploit the resources of their environment. Whereas chemotactic eukaryotic cells can sense gradients by direct comparisons of concentrations along their cell body [40], bacteria employ the strategy of temporal comparisons along their swimming trajectory [18]. Early theoretical work on chemotaxis showed [17] that for the size and swimming velocity of bacterial cells this is the workable sensing strategy. In the presence of a gradient of a compound that bacterial chemoreceptors can detect, the bacterial random walk becomes a biased random walk. When swimming in a favourable direction, cells suppress reorientations and maintain their runs by making temporal comparisons of the stimulus strength (concentration of some compound). The components of the chemotaxis machinery are shown in Figure 39. Bacteria can have one or multiple chemotaxis systems that detect stimuli to control flagellar motors accordingly [81, 91, 140, 141]. The signal is detected and amplified by clusters of receptor proteins on the cell surface. The signal is then transmitted by the histidine kinase CheA that interacts with the receptors, and phoshorylates the intracellular signaling protein, CheY accordingly.

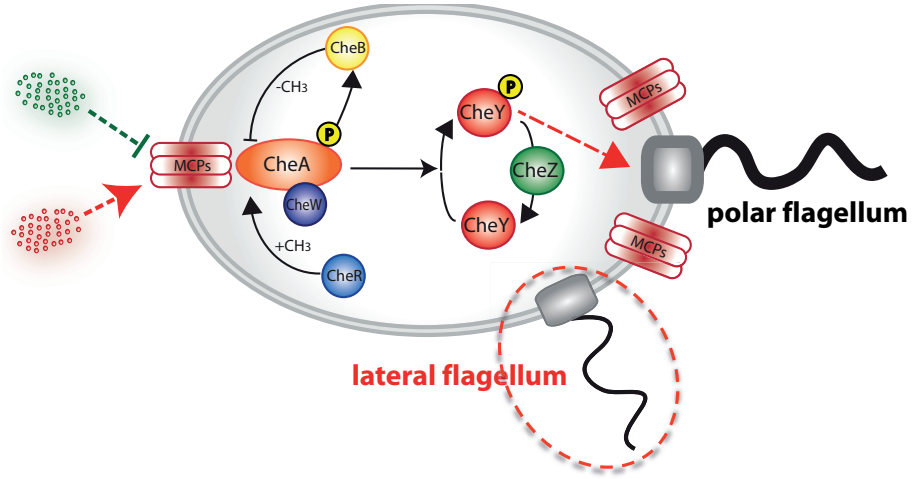

Figure 39. Components of the chemotaxis signaling system and its relation to the polar flagellum in *Shewanella*. This figure is to illustrate the interaction of the chemotaxis signaling system with the polar flagella; in the case of *Shewanella* chemotactic clusters (MCPs) are in reality located at the pole only. The lateral flagellum operates independently of the signaling system.

Phosphorylated CheY diffuses to and directly interacts with the flagellar motor and changes the motor bias in an ultrasensitive fashion, inducing a switch in rotation or a motor break. Most bacterial motors are bidirectional and can rotate either clockwise (CW) or counter-clockwise (CCW). In peritrichously flagellated bacteria, the flagella are distributed all over the cell body's surface, such as in the case of *E. coli*. In the case of these bacteria, CCW rotation leads to the formation of a flagellar bundle, propelling the cell forward in a 'run'. Switching to CW rotation of the motors leads to the disassembly of the bundle, resulting in a 'tumble' and reorientation of the cell. Following the cell's reorientation, a run in a different direction is started, with the motor rotating CCW again [15, 18].

Numerous bacterial species in contrast are polarly flagellated, resulting in a different swimming pattern. For instance, *Vibrio alginolyticus*, a bacteria with a polar flagellar filament, is also propelled forward by the motor rotating CCW, but the cell is then pulled backward when it switches to CW rotation. Also, cell re-orientation does not happen through a 'tumble' but an instantaneous reorientation of the cell ('flick'), caused by a buckling instability of the flagellar hook, when switching back to CCW rotation [139]. This 'run-reverse-flick' pattern results in realignments of approximately 90 degrees and is used for spreading and chemotaxis by Vibrio and some Pseudomonas species [120, 139]. In the species under consideration, *Shewanella putrefaciens*, there is a secondary flagellar system in addition to the primary polar one [26]. A significant fraction of cells express the secondary flagellar system already under planktonic conditions, having one or two additional lateral filament(s).

3.2 Experimental results

A number of experiments were performed by my collaborators Dr. Sebastian Bubendorfer and Florian Rossmann, where the spreading and chemotactic efficiency of Shewanella cells with and without lateral flagellation was compared. In these experiments the flagellar motor protein $FliM_2$ (a component only occurring in the lateral flagellar system) was functionally fused to sfGFP, to distinguish cells with and without the lateral flagellar system. A mutant strain $\Delta flaAB2$ was constructed lacking (due to deletion) the flagellin subunits of the secondary flagellar system, flaA2 and flaB2. These cells exclusively form single polar flagellar filaments.

In one spreading experiment, wild type cells were placed on soft-agar plates and after the radial expansion of the bacterial population, samples were taken at different radial distances from the center. Close to the center of the lateral extension zone about half of sampled cells showed the green fluorescent loci (meaning that they induced the lateral system), a fraction similar to what is observed in planktonic cultures. In contrast all cells isolated from the fringes expressed FliM2-sfGFP, having one or two additional filament(s), as shown in Figure 40a, b.

In another set of experiments on soft-agar plates, the spreading performance of cells with and without functional lateral flagella was compared. Wildtype and mutant cells were mixed in equal amounts and allowed to spread on soft agar for 16h. The growth rate of the two cell types was almost identical. Again, samples were taken at different radial distances from the center and the ratio of wildtype to mutant cells was quantified with fluorescence microscopy. The larger the distance from the center of the lateral extension zone, the further the ratio of both strains was shifted towards the wild type, as shown in Figure 40c. At the fringes of the swimming zones, more than 90% of the population was wild-type, in most cases with a single lateral filament (in addition to the polar system).

Similar results were obtained with chambers consisting of two reservoirs connected by a channel. A 1:1 mixture of wildtype and $\Delta flaAB2$ cells were added to one reservoir. After 12 hours of incubation the samples taken from the other reservoir showed significant enrichment in wildtype cells with a single additional lateral filament, see Figure 40d. The presence of a lateral flagellar system improved the spreading capacity of cells again.

Trajectories of cells with lateral flagellar filaments are different from those with only polar ones, see Figure 41a, b. In both cases, cells follow a 'forward-reverse-flick' pattern: a long forward run is followed by a short backtracking phase, in turn followed by a quick cellular realignment. The average duration (length) and swimming speed of wild type and $\Delta flaAB2$ cells are given in Table 7.

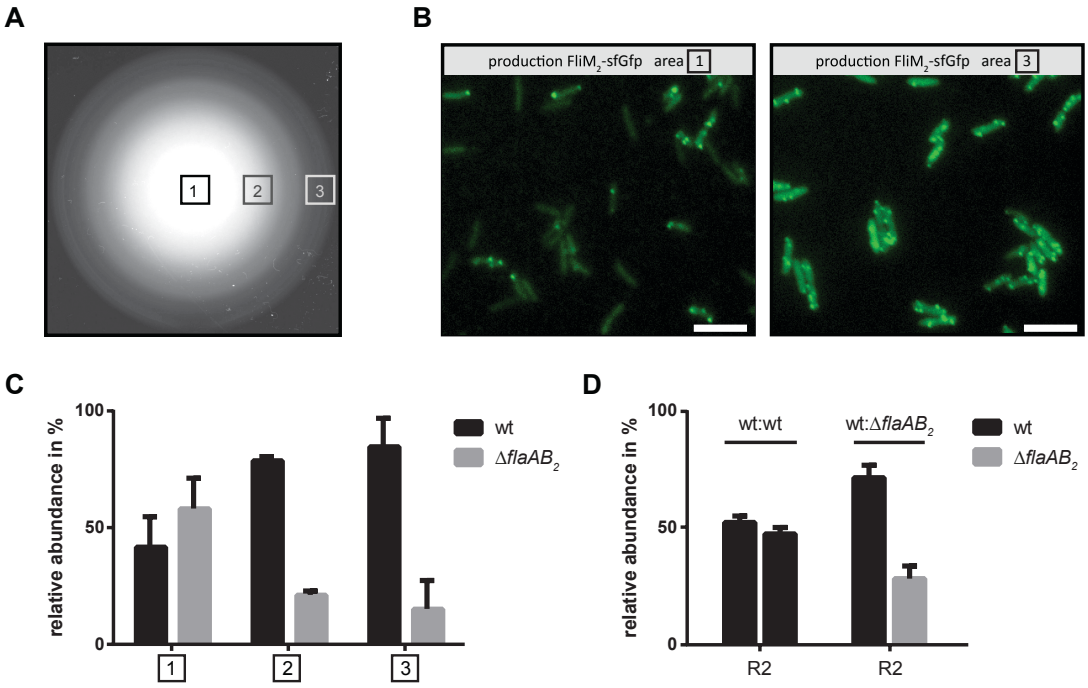

Figure 40. Cells with both polar and lateral flagellar systems outperform mutants with polar flagella only in both soft-agar and liquid medium. *a.* Cells' radial extension in soft agar. Numbers in boxes mark the corresponding sampling areas (1, center; 2, intermediate; 3, rim). *b.* Micrographs of CN-32 *fliM*$_2$*-sfgfp* cells isolated from sampling area 1 and sampling area 3. Scale bars represent 5 μm. *c.* Percentage of fluorescently labeled wild-type and $\Delta flaAB2$-mutant cells in samples isolated from the corresponding sampling areas. *d.* Percentage of fluorescently labeled wild-type and $\Delta flaAB2$-mutant cells after traveling from reservoir 1 (R1) to reservoir 2 (R2) through a medium-filled channel. Figure from joint publication [27]. Figure created by Dr Sebastian Bubendorfer.

However, there is also a difference between cells with and without a lateral filament in the distribution of turning angles during these realignments. Whereas for $\Delta flaAB2$ cells without a lateral flagellar system, the range of angles center around 90 degrees, the wild type cells change direction with a much wider spectrum of angles, and therefore their average turning angle is below 90 degrees. Further knockout experiments showed that the chemotaxis system interacts with the polar flagellar system only, responsible for chemotaxis-induced forward-backward movements. The lateral system on the other hand has a role in shifting the cellular reorientation to smaller angles.

I asked if this difference, also taking into account the other differences in the swimming parameters, duration and speed, can explain the observed differences in spreading performance. Furthermore I wanted to investigate the general effects of the turning angle distribution on spreading and chemotaxis.

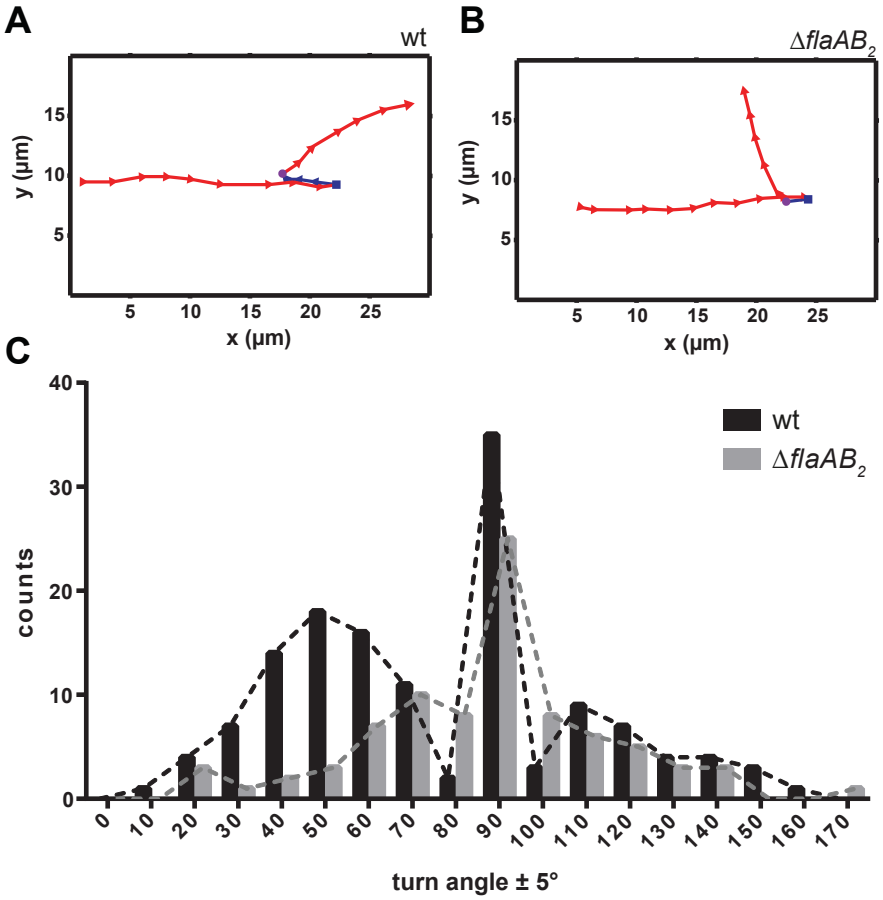

Figure 41. Lateral filament affects the trajectories of swimming cells. A representative trajectory of a wild-type (a) and $\Delta flaAB2$ mutant (b), showing a forward run (red triangles), reversal (blue square), short backward run (blue triangles), flick (purple circle), and forward run movement. (c) Turning angle distribution of wild-type (black) and $\Delta flaAB2$-mutant (gray) cells. Figure from joint publication [27]. Figure created by Dr Sebastian Bubendorfer.

3.3 Mathematical model: effects of the turning angle distribution

3.3.1 Computational Model of Spreading of Shewanella Wild-Type and Mutant Cells

To determine whether the observed differences in swimming behavior are sufficient to explain the observed advantage in spreading, I performed mathematical analysis and computer simulations of motility and chemotaxis of wild-type vs. mutant cells. The movement of cells in a uniform environment without gradients can be described analytically as a 2D correlated random walk [75, 151]. In this approximation, the mean square displacement (MSD) of the population after time t, $R(t)$, can be obtained from the autocorrelation function of the velocity:

$$\langle v(t)v(0)\rangle = exp\left(-\left(\lambda + 2D_r\right)t\right) v^2 exp(\lambda\gamma t) = v^2 exp\left(-\left(\lambda(1-\gamma) + 2D_r\right)t\right) \tag{83}$$

where λ is the turning rate, i.e., reciprocal of the mean run duration, D_r is the coefficient of rotational diffusion, v is the speed of swimming, and γ is the persistence factor of the movement, i.e., the mean of the cosine of the turning angles, $\gamma = \langle cos(\theta) \rangle$. The value of the parameters can be seen in Table 7.

Table 7. Parameters of swimming trajectories for wild type and $\Delta flaAB2$ mutant cells.

	wild type	$\Delta flaAB2$
$\langle cos(\theta) \rangle$	0.214 rad	0.058 rad
v (swimming speed)	47 μm/sec	57 μm/sec
$\langle d \rangle$ (run duration)	21 sec	10 sec

Here, I assumed an exponential distribution of run durations and neglected the short backtracking movement that *S. putrefaciens* CN-32 cells show following runs. The backtracking runs are included later on in stochastic numerical simulations to see if neglecting them has an effect.

Double integration in time on Equation 83 gives the value of the MSD:

$$R(t) = \frac{2v^2 \left(exp\left(-t(2D_r + \lambda(1-\gamma))\right) + 2D_r t - 1\right) + 2\lambda v^2 (1-\gamma)t}{\left(2D_r + \lambda(1-\gamma)\right)^2} \tag{84}$$

The exponential term in the numerator goes to zero on the timescale of spreading experiments (hours), simplifying Equation 84 to:

$$R(t) = \frac{2v^2 t}{2D_r + \lambda(1-\gamma)} - \frac{2v^2}{\left(2D_r + \lambda(1-\gamma)\right)^2} \tag{85}$$

Equation 85 shows that the value of $R(t)$ increases at higher values of the persistence factor γ, as proposed already in a previous theoretical study on insect movement [75]. The lower average turning angle observed for the movement of wild-type cells can thus yield higher persistence and lead to faster spreading.

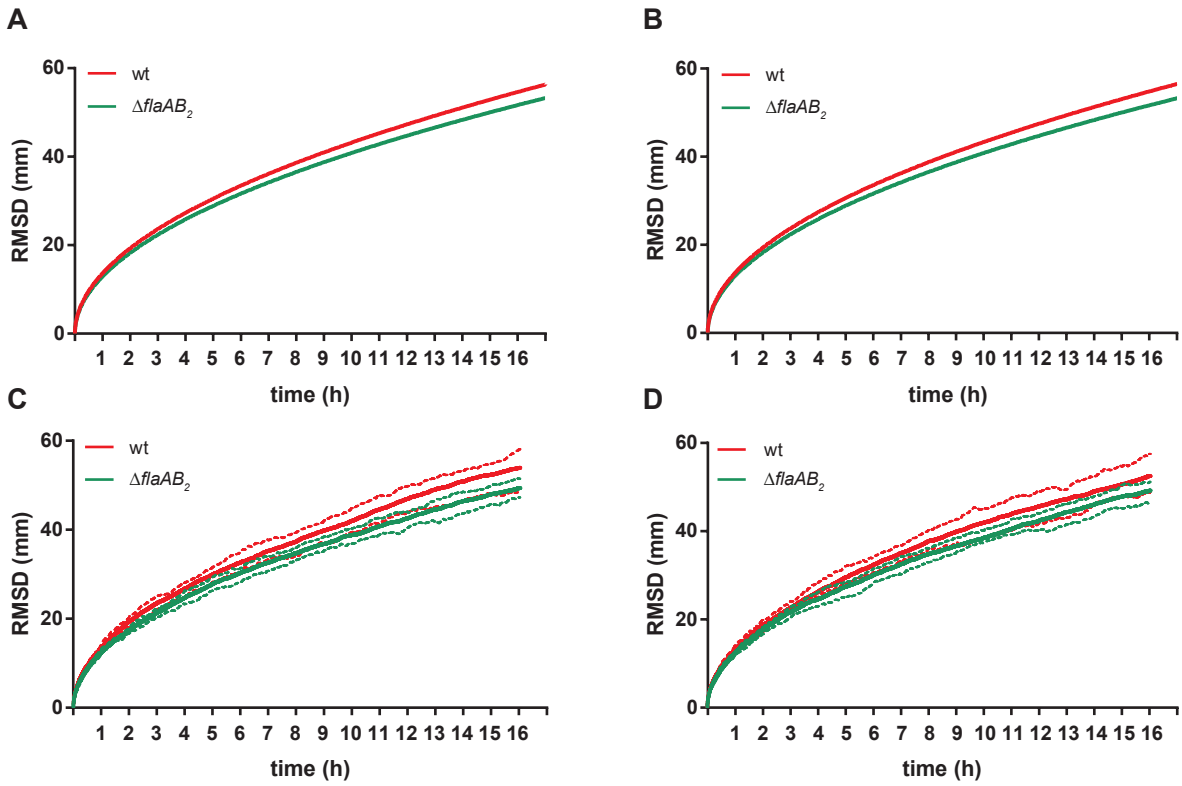

Figure 42. a. Analytical solution for the root mean square displacement (RMSD) of cells using identical parameter values ($v = 57\mu m/s$, $\lambda = 0.1/s$), except for the persistence factor ($\gamma_{WT} = 0.214$, $\gamma_{mutant} = 0.058$). **b.** Same as in panel a, but with experimentally measured parameter values ($v_{mutant} = 57\mu m/s$, $\lambda_{mutant} = 0.1/s$, $\gamma_{mutant} = 0.058$ and $v_{WT} = 47\mu m/s$, $\lambda_{WT} = 0.05/s$, $\gamma_{WT} = 0.214$). $D_r = 0.023 rad^2/s$. **c.** Numerical simulations with same parameters as in **a**, but including backtracking, with duration of backtracking 0.3sec on average. The lines show the mean of 10 independent simulations, with RMSD of 200 cells determined in each simulation. Dots show minimal and maximal values. **d.** Numerical simulations of the population spreading with same parameters as in **b**, but with backtracking included. Figure from joint publication [27].

I next calculated the root mean square distance (RMSD) for the mutant and wild-type strains using the full expression of Equation 84 and the experimentally determined parameter values.

The difference in RMSD in our example is not solely due to the difference in the persistence factor γ, but is a combination of differences in the parameter values: besides higher persistence wildtype cells on the one hand swim slower, but on the other have longer runs. I separately analyzed these effects of Figure 42, where on a and c all parameters of the wildtype and the mutant are set equal, except the persistence factor γ.

In wild-type cells, the effects of their longer run periods and lower speed are mutually compensatory, as can be calculated from Equation 84 (Figure 84 a compared to b) and confirmed by numerical simulations (Figure 84 c compared to d) as well.

The numerical simulations also took into account backward runs. The experimentally measured

angles were binned and assigned discrete probability values. Turning angles in the simulations are generated by drawing random numbers and binning them by these probability intervals. Similarly, run durations are also generated by random number generation from an exponential distribution with the experimentally determined means.

To go into more detail, the movement of an individual cell in the x and y coordinates during the mth run was described as

$$\begin{aligned} x(t+l) &= x(t) + v\ l(m)cos(\alpha(m)) \\ y(t+l) &= y(t) + v\ l(m)sin(\alpha(m)) \end{aligned} \tag{86}$$

where t is time, $l(m)$ is the duration of the mth run, v is the speed of movement, and $\alpha(m)$ is the orientation of the cell during the mth run. $\alpha(m)$ changes from the *m-1*th to the mth run as

$$\alpha(m) = \alpha(m-1) + \Theta(m) \tag{87}$$

where $\Theta(m)$ is the turning angle preceding the mth run. Because there are no observable tumbling periods for *Shewanella* cells, I assumed in our simulations that cells turn instantaneously at the end of runs (and after the short backtracking period). Taking into account rotational diffusion, cell orientation in our simulations changes at every time step Δt as

$$\alpha(t+\Delta t) = \alpha(t) + \eta \tag{88}$$

where η is the term due to rotational diffusion. I assumed the random variable η to be normally distributed as

$$N(m,\sigma) = N(0, [2D_r\Delta t]^{1/2}) \tag{89}$$

where D_r is the coefficient of rotational diffusion. The value of $D_r = 0.023\ rad^2/s$ was used, which is the value determined for *Pseudomonas putida* [151], a bacteria of similar size and polar flagellation. Run durations l and turning angles Θ have experimentally measured probability distributions $p(l)$ and $p(\Theta)$, respectively. I assume that $p(l)$ is exponentially distributed. Monte Carlo simulations were performed by drawing random numbers from the probability distributions of forward run durations, backward run durations and turning angles. The probability distribution for turning angles was obtained by binning our experimental data using 10° bins. For run durations, the means were experimentally measured, and values were generated from the exponential distribution with the respective mean. All scripts were written in $MATLAB$, using

MATLAB's *randn* algorithm to generate random numbers.

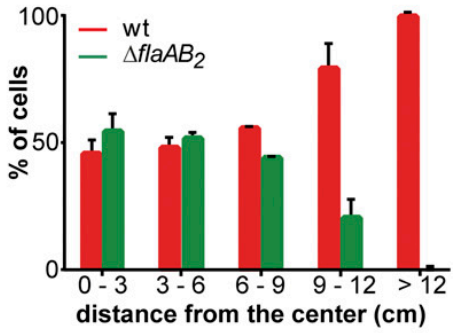

Figure 43. Percentage of wild-type and $\Delta flaAB2$ cells from the simulation in Figure 42 *b* after 16h, at different (radial) distances from the center. The ratio of wild-type to mutant cells rises with increasing distance from the center. The error bars are based on 10 independent simulations. Figure from joint publication [27].

Due to the mutually compensatory effect of the longer run duration but slower swimming speed in the case of wildtype cells, about 90% of the difference in RMSD is attributable to the higher persistence of the wildtype movement. The difference in terms of the RMSD is rather small, but it yields a consistent increase in the ratio of wild-type to mutant cells at the edge of the simulated spreading population, as shown in Figure 43, similar to that observed experimentally (Figure 40*c*).

3.3.2 Computational Model of Chemotaxis of Shewanella Wild-Type and Mutant Cells

The enhancement of spreading in a uniform environment might be an explanation in itself for the benefit conferred by the lateral flagella. Beyond spreading however, higher directional persistence has also been proposed to have a positive effect on the chemotactic movement of bacteria in gradients [94, 108, 151]. To see if this is the case, I constructed a phenomenological model of chemotaxis (based on a model proposed by [94]), to see the effect of the difference in the measured turning angle distribution. I chose this model as it does not require knowledge of the intracellular biochemical parameters of the chemotaxis pathway, since these are unknown for *Shewanella*.

I assumed (as in [94]) that in shallow gradients, the probability of discontinuing a run and turning, the "turning rate", depends on the recent concentration history of the cell as:

$$\lambda(t) = \lambda_0(1 - \Delta(t)) \tag{90}$$

where λ_0 is the basal turning rate (equal to the reciprocal of mean run duration if there is no gradient present) and $\Delta(t)$ is the fractional change of the turning rate. The turning rate is biased by a response function mapping the attractant concentration history of the cell into the fractional

change of the turning rate:

$$\Delta(t) = \int_{-\infty}^{t} c(\tau)R(t-\tau)\ d\tau \tag{91}$$

where $c(\tau)$ is the concentration of attractant experienced by the cell at time τ, and $R(t-\tau)$ is the response function of the cell, specifying the impulse response to the chemoattractant. The turning rate $\Delta(t)$ is then given as the convolution integral of the impulse response and the attractant concentration history, meaning that the chemotaxis system is treated as linear. This model is motivated by the experiments of Berg and Segall and coworkers [23, 129] and has been shown by previous publications to capture the adaptive properties of the chemotaxis pathway [34, 94, 127].

As *Shewanella* is also capable of chemotaxis, its response function should have a similar shape to that of *E. coli*, so that the cell is capable of performing temporal comparisons. $R(t)$ as a function of time should then be double-lobed, with the two important properties that:

$$\begin{aligned} \int_0^\infty R(t)\ dt &= 0, \\ \lim_{t>>1} R(t) &= 0, \end{aligned} \tag{92}$$

in the case of *E. coli*, for $t > 4/\lambda_0$, $R(t)$ should decay to zero.

The response function was previously described as having the form :

$$R(t) = Wexp(-\lambda_0 t)\left\{1 - A\left[\lambda_0 t + \frac{(\lambda_0 t)^2}{2}\right]\right\} \tag{93}$$

W and A are parameters to scale the response. When implementing the chemotaxis model, I chose to use a simpler, sinusoidal, response function that has the same two properties as mentioned in Equation 92, but is computationally less expensive:

$$R(t) = \begin{cases} \epsilon \frac{\lambda_0^2}{v_{swim}} \frac{\pi}{8} sin\left(\frac{\pi\lambda_0 t}{2}\right), & \text{if } 0 \le t \le 4/\lambda_0 \\ 0, & \text{otherwise} \end{cases} \tag{94}$$

so that only the last $4/\lambda_0$ seconds of the cell's concentration history has to be stored and used for the calculation.

When implementing the response function, I discretized time into time steps of $0.1s$, and the turning rate was calculated by a discrete approximation of the convolution integral of Equation 91, using MATLAB's *trapz* function. A random number p is then generated at each time step (*randn* function of MATLAB), and if $P < 0.1\lambda_0$ (the unit of λ_0 is s^{-1}, but time steps are in $0.1s$), the cell turns, with a turning angle generated from the discrete probability distribution of turning angles

we have from our experiments. Otherwise the run is continued. Rotational diffusion is also taken into account at each time step, as described above in Equation 88.

Results of the simulations at different values of the model parameters are shown in Figure 44.

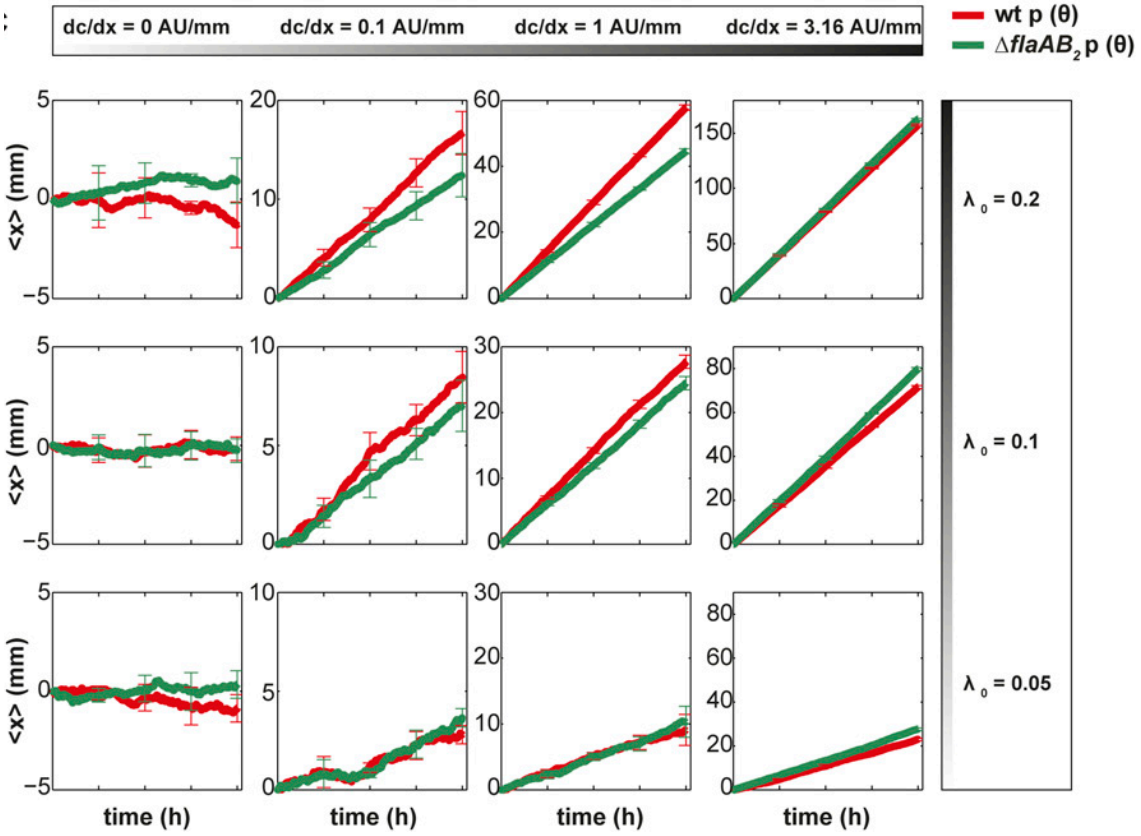

Figure 44. Simulations of chemotaxis in gradients, using the experimentally measured turning angle distributions for wild-type and $\Delta flaAB2$ cells. The scaling factor ϵ was set to $\epsilon = 0.2$. Results are from five independent simulations, each including 1.000 cells. Gradients of indicated steepness (dc/dx) are linearly increasing along the x axis, with $c = 0$ at $x = -100$. At the onset of simulation, cells are placed in random orientations at $x = 0$. The mean position, $\langle x \rangle$, of the cell population along the x axis indicates chemotactic drift along the gradient. The units of distance are millimeters, whereas the unit for concentration c is arbitrary. The basal turning rate λ_0 is varied. Figure from joint publication [27].

The values for the steepness of gradients displayed in the plots show the derivative $d[c]/dx$, the unit of distance being millimeters, whereas concentration $[c]$ is in arbitrary units. I also varied the time window for sensing and the gradients' steepness, to investigate the effect of persistence under different conditions. Wild-type cells indeed showed faster chemotactic movement in shallow attractant gradients (Figure 44), suggesting that under these conditions, the observed higher persistence of movement is sufficient to enhance chemotaxis. This difference became negligible in steeper gradients (Figure 44), presumably because already short directional runs in steep gradients enable cells to experience strong chemotactic stimulation. Moreover, the model used here is likely to

become imprecise in steep gradients. The positive effect of persistence on the chemotactic efficiency is also diminished or annulled by the increase in the run time (Figure 44), because during longer runs, rotational diffusion results in the loss of directional correlation. The exact relation between the run time and the benefit of persistence depends on the value of the coefficient of rotational diffusion, which is not known exactly for *S. putrefaciens CN-32*.

3.4 Conclusions

In the above analysis, I used analytical calculations and stochastic simulations to show that the lower mean turning angle observed in the laterally flagellated wild-type form of the bacteria *Shewanella* leads to more efficient spreading in a uniform environment.

The root mean square distance of a population moving in two dimensions can be derived analytically and analyzed as the function of the motility parameters: swimming speed, run duration and directional persistence. I calculated from this formula that the advantage in spreading that wild-type cells show is due to their higher directional persistence, which in turn is a result of the turning angle distribution having a lower mean.

Furthermore, by stochastic simulations of a phenomenological chemotaxis model, I also showed that higher directional persistence has a positive effect on directed movement (i.e. chemotaxis) as well, as long as gradients are relatively shallow, so that the response function of the turning bias can be modeled linearly. This advantage in spreading and chemotaxis is likely to be one evolutionary factor for the emergence and maintenance of the lateral flagellar system.

4 Appendix

4.1 Information theoretical analysis of sensing in the mating pathway

It is visually evident from Figure 45, showing the response of *wt* and *bar*1Δ cells to partner cell fraction θ_α (at $\rho_T = 2$), that the *wt* strains perform better at extracting information on the fraction of partner cells within the total population, due to the nearly linear, non-saturating response that signal attenuation leads to. I wanted to quantify how much information *wt* and *bar*1Δ cells can extract about the partner cell fraction (θ_α) by using the concept of mutual information from information theory. The main concepts of information theory are reviewed in the textbooks [117, 152], or, in a biological context, in the reviews [123, 167]. I review now very briefly the main concepts of information theory.

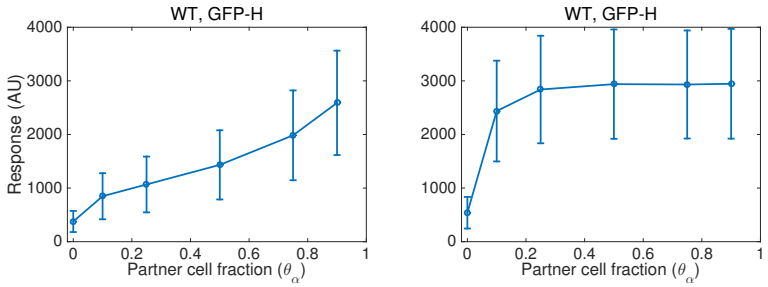

Figure 45. Mean responses in mixing experiments to partner cell fraction θ_α, for *wt* and *bar*1Δ cells. Responses to θ_α are shown at the highest total density $\rho_T = 2$ ($2 * 10^7$ cells/ml). Error bars show standard deviation of the underlying single cell data. The flow cytometry experiment measuring the output of the mating pathway reporter gene P_{FUS1}-GFP was carried out by Dr Alvaro Banderas.

4.1.1 Main concepts of information theory

Information theory was originally developed by Claude Shannon to analyze artificial communication systems [133], but it provides a general mathematical framework to quantify the amount of information that can be transmitted through a noisy communication channel. The attractive feature of this analytical framework, which makes it applicable to cell signaling as well, is that only input and output measurements are required, and a detailed understanding of the signaling system is not a prerequisite. Using information theory, a complex system can be reduced to a black box communication channel and its capacity for information transmission can be quantified.

Cellular signaling can be described as an information transmission problem, where chemical signals (such as α-pheromone) convey information about some feature of the external environment (such as the amount or fraction of α-cells) to the 'decision centers' (for instance the nucleus) of the

cell. Due to the stochastic nature of chemical reactions in the signaling networks (a noisy channel) of a cell, molecular noise will hamper the fidelity of any messages received by the cell, leaving it with imperfect information about the environmental cue. The traditional metrics for noise (such as variance) tell us the magnitude of noise, but they do not quantify the degree to which the noise hampers the ability to discriminate between different inputs. With the measures provided by information theory, such a quantification can be carried out. In the case of biological systems and biological noise, one would typically look at the distribution of responses to a certain input by a population of genetically identical cells. In this case, the variation in the response distribution has two fundamental sources, often termed 'intrinsic' and 'extrinsic' in the systems biology literature [43, 147]. One is molecular noise, due the stochastic nature of chemical events (intrinsic noise). The other is cell-to-cell variation in expression levels of the components of the signaling pathway or expression capacity (extrinsic noise).

To quantify the fidelity of information transmission by a given cellular signaling system, we need to describe it as a communication channel, which couples an input source of information to some output. A channel can be mathematically described by a random variable for its input and another random variable for its output, with the values of the two variables depending on each other. Measuring the output value helps to resolve the input value and we can quantify the amount of information gained by the concept of *mutual information*.

The concept most commonly used to quantify information itself is *Shannon-entropy* (from now on simply *entropy*), which is a measure of uncertainty, quantifying how unpredictable the value of a random variable is. For a discrete random variable X that can take on the values x_1, x_2 ... x_n with probabilities $p(x_1)$, $p(x_2)$,..., $p(x_n)$, the entropy H is calculated as:

$$H(X) = -\sum_{i=1}^{n} p(x_i) log_2(p(x_i)) \tag{95}$$

Using a base 2 logarithm means that the entropy is measured in bits. Because $0 \leq p(x_i) \leq 1$ (and in calculations we define $0\ log_2 0 = 0$) entropy is necessarily non-negative.

In a biological context, entropy is used both to quantify the uncertainty in the input (probability distribution of input values), and the responses that a population of cells produce at a given stimulus. If the variance of the response distribution is higher, there is more uncertainty in how an individual cell responds to the given stimulus, and therefore the associated entropy is higher.

Using the entropy measure, the fidelity of signaling is quantified by the concept of mutual information. Considering that the signaling pathway of a cell is a communication channel that maps an input to an output, successful communication occurs if the knowledge of the output value

makes it possible to determine the input value that was transmitted through the channel. Mutual information $I(X,Y)$ is the reduction in the uncertainty about the input X given the value of output Y, as can be seen in the mathematical definition for discrete random variables:

$$I(X,Y) = H(X) - H(X|Y) \tag{96}$$

$H(X|Y)$ is the conditional entropy, quantifying the amount of information we need to determine the outcome of random variable X (the input) given that the value of random variable Y (the response or output) is known. In the case of a communication channel without any noise, this is zero, and the mutual information is maximal, equal to $H(X)$. At the other extreme, $H(X|Y) = H(X)$, and the mutual information is 0, as the output does not reduce the uncertainty about the input at all.

Calculation of mutual information can be performed by the formula [123]:

$$I(X,Y) = \sum_{i,j} p(x_i, y_j) log_2 \frac{p(x_i, y_j)}{p(x_i)p(y_j)} \tag{97}$$

and requires binning of the data, to obtain marginal ($p(x_i)$, $p(y_j)$) and joint ($p(x_i, y_j)$) probability distributions. Because of the finite sample size, mutual information estimates obtained by binning can produce significant overestimates if samples are too small [33]. As the estimates I provide are either from flow cytometry data with typically 10,000 cells per input value, or are based on simulations, this bias due to undersampling is not a problem in our examples.

4.1.2 Application of information theory to the wild type response and noise correction

I quantified the mutual information of the response of *wt* and *bar1*Δ strains to θ_α (Figure 45) by binning of the data, as plotted in Figure 46. Here, as in all mutual information calculations below, a uniform distribution was assumed for the input θ_α.

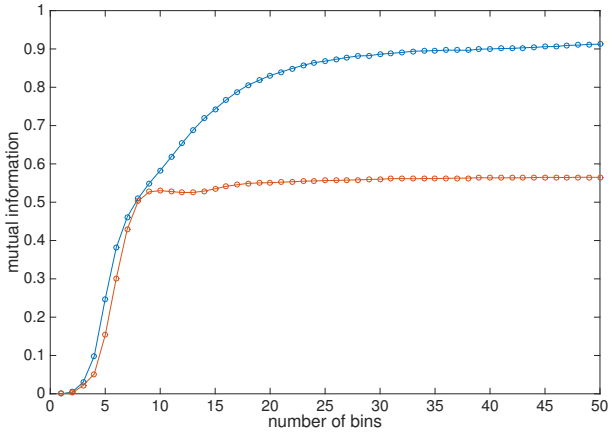

Figure 46. Mutual information estimate from flow cytometry experiment. Blue line is *wt* cells, red *bar*1Δ cells.

This estimate however is arguably underestimating the cells' capacity of information transmission, because of the following. Some of the variation in the response of the cells, lowering the mutual information estimate, is due to differences in their expression capacity, e.g. different number of ribosomes. As I wanted to have a measure of the fidelity of signaling by the mating pathway, I argued that this source of variation should be ideally separated and removed, as it does not constitute a measurement 'error' from the point of view of an individual cell. For instance, if the response of an individual cell could be measured over and over, its expression capacity would scale its responses identically. Also, its general resource investment (response of other genes induced by the mating pathway) into the mating response would also be scaled by its expression capacity. Therefore I wanted to remove the fraction of variation in the response of the population that is due to cell-to-cell differences in expression capacity, and then re-estimate the mutual information.

To do this, I used the linearization approximation for the output of a gene developed by [35]. At the same time, I made explicit some necessary assumptions required by this model that was not discussed there. In this approximation the output of a gene in an individual cell is described as:

$$y_i = (L_i + \lambda_i)(G_i + \gamma_i) \tag{98}$$

y_i is the output of a gene, which is described as the product of two subsystems, the 'pathway' and 'expression' subsystem. In each subsystem there are two sources of variation, stochastic chemical events (λ_i, γ_i) and cell-to-cell differences in 'capacity' (pathway capacity: L_i and expression capacity: G_i) that persist on a longer timescale (considered constant on the timescale of a mixing experiment for example). In an individual cell, if the experiment could be repeated over many times, the average output would be defined by the (product of) pathway and expression capacity,

as the deviations due to stochastic chemical reactions in both subsystems would average to zero. If however this could be repeated for another cell j, the average output (over time) would be different, defined by $L_j G_j$.

The first subsystem, the pathway, encompasses all steps that lead to the activation of transcription, i.e. the binding of activated transcription factors. The pathway capacity (L) is then the average level of pathway activation in a given cell at a certain level of stimulation. The stimulation (input) in our case is the concentration of α-factor, which in turn is a function of the amount of partner cells (α-cells, θ_α) in mixing experiments. Pathway capacity L could vary from cell to cell due to the expression levels of the pathway's regulatory proteins for example (which on a longer timescale could also change). The stochastic part (λ) of the pathway subsystem is due to the probabilistic nature of individual chemical reactions (binding-unbinding events and covalent modifications), even if expression levels are constant. Together their sum makes up the output of the pathway susbsystem: $P_i = L_i + \lambda_i$, which in the case of the mating pathway would be the number of active Ste12 molecules binding to the promoter P_{FUS1}.

The second subsystem, expression, includes all steps from transcription initiation to the accumulation of the protein, and its output is the amount of mature fluorescent reporter protein. The output is defined as a sum of expression capacity (G_i), which would include factors such as the numbers of ribosomes or RNA polymerase II complexes or the cellular energy level, and stochastic chemical events during the expression process (γ_i).

In this framework, the total variation ($\eta^2 = \frac{\sigma^2}{\mu^2}$) for a population of cells for a gene is a sum of these factors, plus a correlation term:

$$\eta^2 = \eta_L^2 + \eta_\lambda^2 + \eta_G^2 + \eta_\gamma^2 + 2\rho(L,G)\eta_L\eta_G \tag{99}$$

This relation is obtained by including only linear (and neglecting all higher order) terms when calculating the variance, as derived in [35]. The same linear approximation gives us the mean output:

$$\bar{y} = \bar{L}\bar{G}(1 + \rho(L,G)\eta_L\eta_G) \tag{100}$$

The stochastic noise term within the pathway subsystem, λ, cannot be separately determined from the data (see below), therefore I use the total variation of the pathway subsystem η_P from now on, replacing $\eta_L^2 + \eta_\lambda^2$ with η_P^2 and $\rho(L,G)\eta_L\eta_G$ with $\rho(P,G)\eta_P\eta_G$. Then Equations 99 and 100 become:

$$\eta^2 = \eta_P^2 + \eta_G^2 + \eta_\gamma^2 + 2\rho(P,G)\eta_P\eta_G \tag{101}$$

and

$$\bar{y} = \bar{P}\bar{G}(1 + \rho(P, G)\eta_P\eta_G) \tag{102}$$

The noise terms can be inferred from the data in the following way. First, in double reporter experiments with two copies of the same promoter, the only uncorrelated part of the variation are stochastic chemical events in the expression subsystem, η_γ. The variation (both stochastic events and variation in pathway capacity) in the pathway subsystem is transmitted to the expression subsystem, therefore these are correlated. The uncorrelated part of the variation (denoted Z) in this case (for two copies of gene i) is:

$$Z_{ii} = \eta_i^2(1 - \rho_{i,i}) = \eta_{\gamma i}^2 \tag{103}$$

η_i is the total variation calculated from the data for one fluorophore (under the control of the same promoter, I take this to be identical for the two flurophores), and $\rho_{i,i}$ is the correlation of the two fluorophores. From these equations one can determine the stochastic noise term of the expression subsystem, η_γ.

For double reporter experiments with two different promoters (promoters i and j, $i \neq j$) per cell, the uncorrelated part of the noise includes both the pathway subsystem (as the two promoters have different pathways) and the stochastic noise of the expression module, and Z is:

$$Z_{ij} = \frac{\eta_i^2 + \eta_j^2}{2} - \eta_i\eta_j\rho_{i,j} = \frac{\eta_{\gamma i}^2 + \eta_{\gamma j}^2}{2} + \frac{\eta_{Pi}^2 + \eta_{Pj}^2}{2} \tag{104}$$

Again, η_i, η_j and $\rho_{i,j}$ are empirical measures calculated from the data.

As the number of equations generated from Equations 103 and 104 is $\frac{n(n+1)}{2}$ (n being the number of reporter genes), and the number of unknowns $2n$, we need $\frac{n(n+1)}{2} = 2n$, $n=3$ (three reporter genes) to determine the pathway noise (η_P) and stochastic expression noise (η_γ) terms separately. If $n=2$, only the sum $\eta_{P1}^2 + \eta_{P2}^2$ could be determined. The three genes would be two constitutive (in practice inducible promoters, such as the doxycycline-induced repressor system P_{TET07}) promoters, and the third gene the pathway gene of interest, in our case P_{FUS1}, see Table 8 for the statistical parameters of each promoter that I used.

Working with three reporter genes, now we already have $\eta_{P1}, \eta_{P2}, \eta_{P3}$ and $\eta_{\gamma 1}, \eta_{\gamma 2}, \eta_{\gamma 3}$.

I want to calculate the width of the distribution without the variation in expression capacity (η_G). Having calculated η_P and η_γ, I can simply set the terms including expression variation η_G

to 0 in Equation 99, so that the equation for total noise becomes:

$$\hat{\eta}_i^2 = \eta_{Pi}^2 + \eta_{\gamma i}^2 \tag{105}$$

However, to calculate the distributions excluding expression capacity variation, I also need to re-calculate the means of the distributions (using Equation 102) as they also depend on expression capacity, because of the (possible) correlation of expression and pathway capacity. The corrected mean $\hat{\bar{y}}$ will be equal to $\bar{P}\bar{G}$, but I have no access to this product, so it has to be calculated from Equation 102, making it necessary to calculate η_G and the correlation terms $\rho(P, G)$ from the system of equations generated by Equation 106.

To determine η_G and the correlation terms $\rho(P_1, G), \rho(P_2, G), \rho(P_3, G)$, I can use the sums for the total noise of each gene:

$$\eta_i^2 = \eta_{Pi}^2 + \eta_G^2 + \eta_{\gamma i}^2 + 2\rho(P_i, G)\eta_{Pi}\eta_G \tag{106}$$

Alternatively, one can write down the equations for the correlated part of the variation of two reporter genes for identical promoters:

$$\rho_{ii}\eta_i^2 = \eta_{Pi}^2 + \eta_G^2 + 2\rho(P_i, G)\eta_{Pi}\eta_G \tag{107}$$

or for two different promoters ($i \neq j$):

$$\rho_{ij}\eta_i\eta_j = \eta_G^2 + \rho(P_i, G)\eta_{Pi}\eta_G + \rho(P_j, G)\eta_{Pj}\eta_G \tag{108}$$

The left hand side of each equation is determined from the data, as are the terms η_{Pi} and $\eta_{\gamma i}$ (from Equation 103 and 104), which can then be absorbed into a constant on the left-hand side, rewriting Equation 106 as

$$c_i = \eta_G(\eta_G + 2\rho(P_i, G)\eta_{Pi}) \tag{109}$$

and Equation 108 as

$$a_{ij} = \eta_G(\eta_G + \rho(P_i, G)\eta_{Pi} + \rho(P_j, G)\eta_{Pj}). \tag{110}$$

Clearly, $a_{ij} = \frac{c_i + c_j}{2}$, so I can only use the system of equations either from Equation 109 or Equation 110, as the two are equivalent. This gives us $n+1$ unknowns for n equations, namely η_G and $\rho(P_i, G)$, $i = 1...n$.

In the case of three promoters (reporter genes) the system of equations (using Equation 110) I have is:

$$\begin{aligned}\rho_{1,2}\eta_1\eta_2 &= \eta_G(\eta_G + \rho(P_1,G)\eta_{P1} + \rho(P_2,G)\eta_{P2})\\ \rho_{1,3}\eta_1\eta_3 &= \eta_G(\eta_G + \rho(P_1,G)\eta_{P1} + \rho(P_3,G)\eta_{P3})\\ \rho_{2,3}\eta_2\eta_3 &= \eta_G(\eta_G + \rho(P_2,G)\eta_{P2} + \rho(P_3,G)\eta_{P3})\end{aligned} \tag{111}$$

To solve for η_G and the correlation terms, at least one correlation term has to be arbitrarily defined (a fact that is not made clear in [35]). A biologically reasonable choice is to set the correlation $\rho(P_i, G) = 0$ in the case of a constitutively expressed reporter gene (in our example $\rho(P_1, G) = 0$), as here there are no pathway components (except for the repressor) for which a feedback effect as a function of global expression could be operational. Treating ρ_1 (shorthand for $\rho(P_1, G)$) as a parameter, we can solve for the other three unknowns (left-hand sides of Equations 111 denoted a_{12}, a_{13}, a_{23}, respectively). The positive solutions of this system of quadratic equations are:

$$\begin{aligned}\eta_G &= \sqrt{2a_{12} - a_{23} + \eta_{P1}^2\rho_1^2} - \eta_{P1}\rho_1\\ \rho_2 &= \frac{a_{12}\rho_1\eta_{\mathrm{P1}} - a_{12}\sqrt{2a_{12} - a_{23} + \rho_1^2\eta_{\mathrm{P1}}^2} + a_{23}\sqrt{2a_{12} - a_{23} + \rho_1^2\eta_{\mathrm{P1}}^2}}{2a_{12}\eta_{\mathrm{P2}} - a_{23}\eta_{\mathrm{P2}}}\\ \rho_3 &= \frac{a_{13}\left(\sqrt{2a_{12} - a_{23} + \rho_1^2\eta_{\mathrm{P1}}^2} + \rho_1\eta_{\mathrm{P1}}\right) + (a_{23} - 2a_{12})\sqrt{2a_{12} - a_{23} + \rho_1^2\eta_{\mathrm{P1}}^2}}{(2a_{12} - a_{23})\,\eta_{\mathrm{P3}}}\end{aligned} \tag{112}$$

When setting $\rho_1 = 0$, the solutions are:

$$\begin{aligned}\eta_G &= \sqrt{2a_{12} - a_{23}}\\ \rho_2 &= \frac{a_{23} - a_{12}}{\sqrt{2a_{12} - a_{23}}\eta_{\mathrm{P2}}}\\ \rho_3 &= \frac{-2a_{12} + a_{13} + a_{23}}{\sqrt{2a_{12} - a_{23}}\eta_{\mathrm{P3}}}\end{aligned} \tag{113}$$

In the following, I provide a numerical example with a total noise estimate from experimental data (experiments by Dr Alexander Anders) and noise composition from [35]. As I did not have the necessary experimental data, all values below are simulations. The parameters used are shown in Table 8. I use a schematic description of the mating pathway's behavior in wild type cells at a sufficiently high value of ρ_T, where the response is a function of the fraction of partner cells, θ_α (see Section 1.3). Specifically, I define the (normalized) mean response as simply equal to θ_α, $\bar{y} = \theta_\alpha$.

Table 8. Statistical properties of noise components for simulated mixing experiment. Pathway capacity (L) is correlated with the expression capacity (G) through the scaling factor β in the exponential term. The correlation is weak ($\beta = -0.02$) for the constitutive promoters which have a single 'pathway' component (a repressor), and stronger for the pathway reporter gene ($\beta = 0.5$). The variation terms L and G are gamma-distributed random values, with the probability distribution $\Gamma(k,\theta) = \frac{1}{\Gamma(k)\theta^k}x^{k-1}e^{-\frac{x}{\theta}}$, generated by MATLAB's *gamrnd* algorithm. The mean output of the pathway subsystem of gene 3, $\bar{L}_3$ is equal to the partner cell fraction θ_α.

	η_G	η_P	η_γ	$\rho(P,G)$
gene 1 (constitutive)	$\Gamma(30, 1/30)$	$L_i = \Gamma(10, \frac{1}{10}exp(\beta(G_i - < G >))$ $\beta = -0.02$ $\lambda \sim N(0, \sigma_\lambda = 10^{-1.5})$	$N(0, \sigma_\gamma = 10^{-1.5})$	≈ -0.05
gene 2 (constitutive)	$\Gamma(30, 1/30)$	$L_i = \Gamma(10, \frac{1}{10}exp(\beta(G_i - < G >))$ $\beta = -0.02$ $\lambda \sim N(0, \sigma_\lambda = 10^{-1.5})$	$N(0, \sigma_\gamma = 10^{-1.5})$	≈ -0.05
gene 3 (pathway)	$\Gamma(30, 1/30)$	$L_i = \Gamma(\theta_\alpha \frac{exp(\beta(G_i - <G>))}{0.18^2}, 0.18^2)$ $\beta = 0.5$ $\lambda \sim N(0, \sigma_\lambda = \theta_\alpha 10^{-1.5})$	$N(0, \sigma_\gamma = 10^{-1.5})$	$0.16 < \rho < 0.44$

The aim with this numerical calculation was two-fold. On the one hand, I wanted to see the extent of increase in mutual information by the mating pathway's reporter gene, if the variation due to expression capacity is removed through this noise decomposition method. Second, as I am working here with simulated 'data', I could assess to what extent the noise decomposition and subtraction of the expression capacity variation gives us a good estimate of the response variation 'cleansed' of this source of variation. To do this, I also generated a population of simulated 'cells' without any variation in expression capacity but with the other noise components having identical statistical properties. I compare the response distributions of these *in silico* cells to those we get by noise decomposition and subtraction η_G from the cells with all noise sources, see the results in Figure 51.

The mean value of the output follows the input due to pathway activity, so that $\bar{L} = \bar{P} = \theta_\alpha$. We do not expect the mean expression capacity $\bar{G}$ to vary with the input. The stochastic terms in the pathway and expression subsystems are modeled as normal variables with zero mean, $\lambda \sim N(0, \sigma_\lambda)$, $\gamma \sim N(0, \sigma_\gamma)$. The terms for pathway and expression capacity variation were modeled as gamma-distributions. Protein expression levels have been described to approximate the latter [21, 28, 53, 149], having the additional advantage in simulations of excluding negative values (that would have to be removed, thereby changing the shape of the distribution). As shown in Figure 47, the experimental data shows that the η^2 for the pathway decreases with mean pathway output, both in dose-response experiments with purified α-factor, or in mixing experiments, where θ_α is varied.

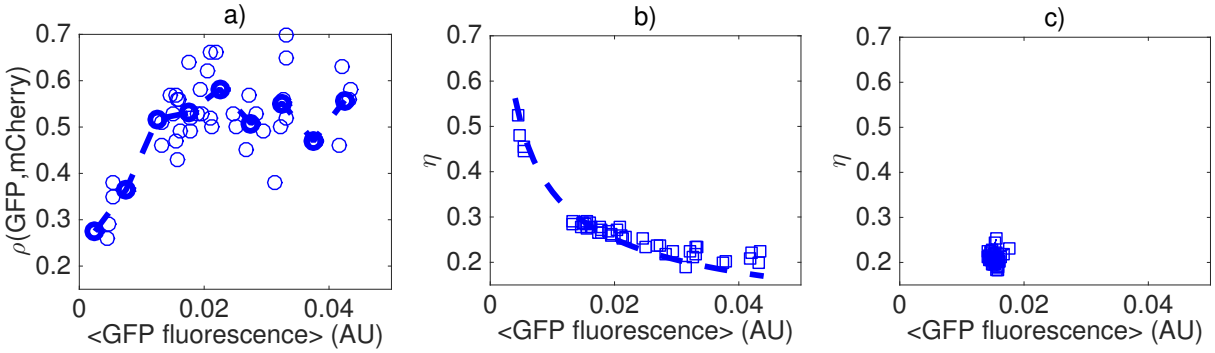

Figure 47. Coefficient of variation (η) and correlation measures from microscopy data (experiment by Dr Alexander Anders), as a function of the mean fluorescence of cells. Each blue circle or square is the mean GFP fluorescence at a given dose of α-pheromone. Data is from several dose-response experiments. *a*) Correlation of Fus1-GFP and mCherry values increasing with the mean Fus1-GFP value. The dashed blue line shows the mean correlation values after binning mean GFP fluorescence from 0 to 0.05 by bins of 0.005. *b*) Coefficient of variation of GFP values from the mating pathway gene *Fus1-GFP* as a function of their mean (μ) for dose response experiments (same as *a*)) with purified α-factor. Fitted (dashed blue line) with the relation $\eta \propto \frac{1}{\sqrt{\mu}}$. *c*) Coefficient of variation of GFP values from the doxycycline-induced constitutive promoter expressing *mCherry* as a function of their mean (μ). There is no noticeable trend, as the mean output does not change with the pheromone dose.

As η_G or η_γ should not vary with the mean pathway output, the decrease in total noise (with the mean output) is due to η_P, the variation in the pathway subsystem (which includes the binding of transcription factors as well). I defined $\eta_P \propto \frac{1}{\sqrt{\mu}}$ (μ the mean output of the pathway subsystem) in simulations. in Figure 47 we can see the increasing correlation of P_{FUS1}-GFP and P_{TET07}-mCherry values in microscopy data.

As already explained above, the noise decomposition and the subtraction of expression capacity variation η_G (Equations 103-113) can only be performed with three reporter genes (one, the pathway reporter of interest and two other constitutive promoters), each tagged with 2 different fluorescent proteins. In total, six experiments are needed, three experiments with two copies of identical promoters (Equation 103), and three experiments where each cell has two different promoters.

Figure 47 shows the η and correlation trends of the simulated data. The parameters used to generate the simulated data are shown in Table 8.

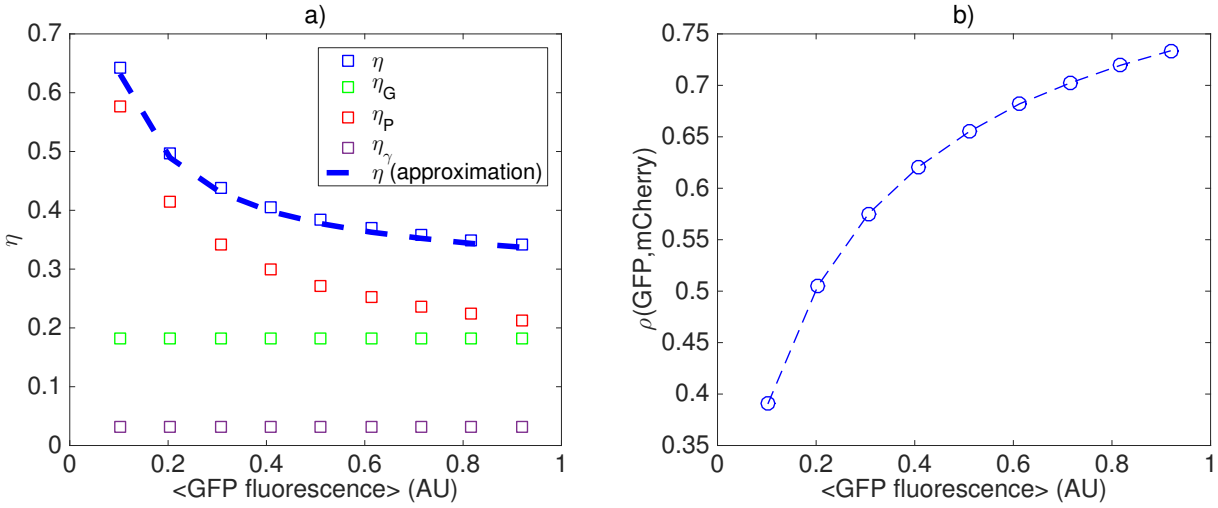

Figure 48. Coefficient of variation (η) and correlation measures for simulated data. *a*) The CV is plotted as a function of the mean value of the pathway reporter gene (gene 3 in Table 8), the different components of the total noise η (filled blue squares) are shown. The dashed blue line shows the noise estimate from the linearization approximation, $\eta = \sqrt{\eta_P^2 + \eta_G^2 + \eta_\gamma^2 + 2\rho(P,G)\eta_P\eta_G}$. *b*) Correlation between the pathway reporter gene and the constitutive reporter growing with the mean output of the former, as in the experimental data shown in Figure 47*a*).

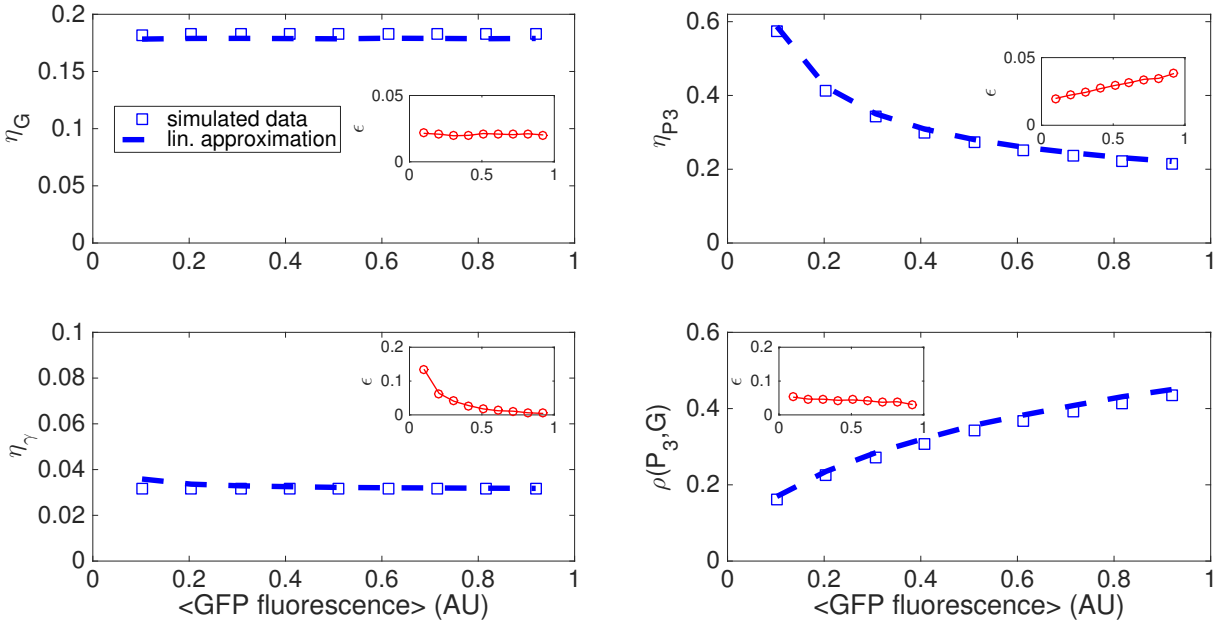

Figure 49. Noise components of the pathway output gene (gene 3 in Table 8) as a function of mean pathway output and their estimates inferred from simulated data using the linearization approximation, and setting $\rho(P_1, G) = 0$, see Equation 113. The insets show the relative error of the estimates, $\epsilon = |\frac{x - x_{approx.}}{x}|$, where x is (in this case simulated) data.

The actual values of the noise components and their estimates derived from the simulated data using the approximations (setting $\rho(P_1, G) = 0$) can be seen in Figure 49. As we have the actual values of the noise components, I can quantify the error of the approximation, plotted in the insets

of Figure 49, showing the relative error ϵ of the noise components η_G, η_{P3}, $\eta_{\gamma 3}$, and the correlation term $\rho(P_3, G)$. For each component of the total noise (of the pathway reporter gene), the relative error of the approximation is less than 10% (the only exception is the η_γ estimate at the lowest pathway output). The error estimates shown in this figure are for the case when the neglected correlation term $\rho(P_1, G) = -0.02$. Besides linearization, there is also an error introduced to the noise component estimates due to setting $\rho(P_1, G) = 0$. I also varied the value of this term to see how the error increases, see Figure 50. In the case of a weak correlation between expression and pathway capacity for the constitutive reporter gene, the error introduced by neglecting this term is minimal. If the correlation of global expression capacity (G) and pathway capacity (L) is stronger, the deviation of the approximation from the actual value grows, as shown in Figure 50.

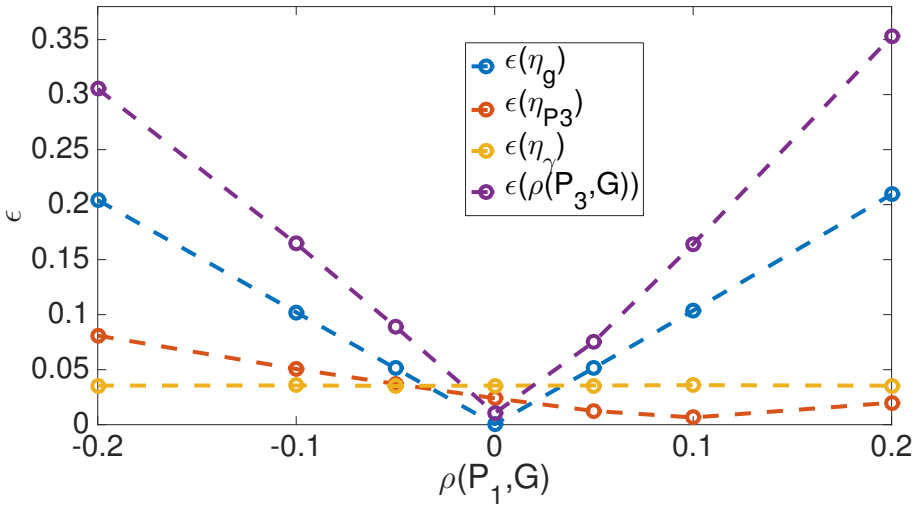

Figure 50. Relative error of noise components and correlation estimates as a function of the neglected correlation term $\rho(P_1, G)$.

Continuing with our numerical example where $\rho(P_1, G)$ was low (-0.02), I re-calculated the mean pathway outputs, as described by Equation 102: $\hat{\bar{y}} = \frac{\bar{y}}{1+\rho(P_3,G)\eta_{P_3}\eta_G}$, where $\bar{y}$ is the mean pathway output from the data, and $\hat{\bar{y}}$ the corrected one.

Next, I had to re-generate a distribution without the global expression variation term, that is: $\hat{\eta}^2 = \eta_{P3}^2 + \eta_\gamma^2$, $\hat{\eta}$ being the corrected CV. I re-generated the corrected distribution as a gamma distribution, as this was used for generating the noise components of our simulated data, but the procedure could also be performed with a normal distribution, if the experimental data can be better fit that way. Since we now have the CV ($\hat{\eta} = \frac{\sigma}{\mu}$) and the mean ($\hat{\bar{y}} = \mu$) of the corrected distribution, I could calculate the two parameters of the gamma distribution, as $\sigma^2 = k\theta^2$ and $\mu = k\theta$. After performing the noise decomposition and re-generating the response distributions without expression capacity variation, I looked at how these inferred distributions deviate from

those of the *in silico* cells without expression capacity variation. I made two comparisons here. First, I calculated the distance of the noise-corrected distributions from those obtained from the *in silico* cells without expression capacity variation (G_i=<G> for every cell). Second, I compared the estimates for mutual information from these two sources.

There are several distance metrics that can be used to compare two probability distributions, here I used total variation distance [90] of the distributions $P(x)$ and $Q(x)$, which on a countable state space Ω is:

$$\delta(P,Q) = \frac{1}{2}\sum_{x\epsilon\Omega} |P(x) - Q(x)| \tag{114}$$

This metric assumes values in [0, 1]. Although we have the analytical formula for the corrected distribution, this is not the case for the data from the *in silico* experiments without global expression variation, therefore for this calculation both distributions have to be binned. in Figure 51, I plotted the two distributions and their total variation distances.

We can see that the distance between the re-generated distributions based on the linearization approximation and those from the *in silico* experiment without global expression noise is minimal. As the last step, I calculated the mutual information between the response and the partner cell fraction θ_α. This was again compared to the mutual information from the *in silico* experiment without global expression noise, to see if the mutual information estimate from the linearization approximation is a faithful estimate of the information transmission by cells if we remove the variation of global expression capacity. Finally, the mutual information estimate of the corrected distribution was compared to that of the original (simulated) data to see the extent of improvement in information transmission after variation of global expression capacity was removed.

With the total noise estimate taken from our microscopy data and noise composition from the literature [35], we get a roughly 30% increase in mutual information. The relative error from the *in silico* experiment without global expression capacity variation (η_G) is 2%, which also shows that the estimate we get from the noise decomposition above is a faithful representation of the response distributions without variation in expression capacity. Naturally, if the fraction of global expression variation (η_G) (and/or its (positive) correlation with pathway capacity) is larger within the total noise, then the improvement in mutual information would be higher.

Since I worked here with simulated data using 10^6 datapoints per input value, overestimation of mutual information due to limited sample size [33] is not a problem.

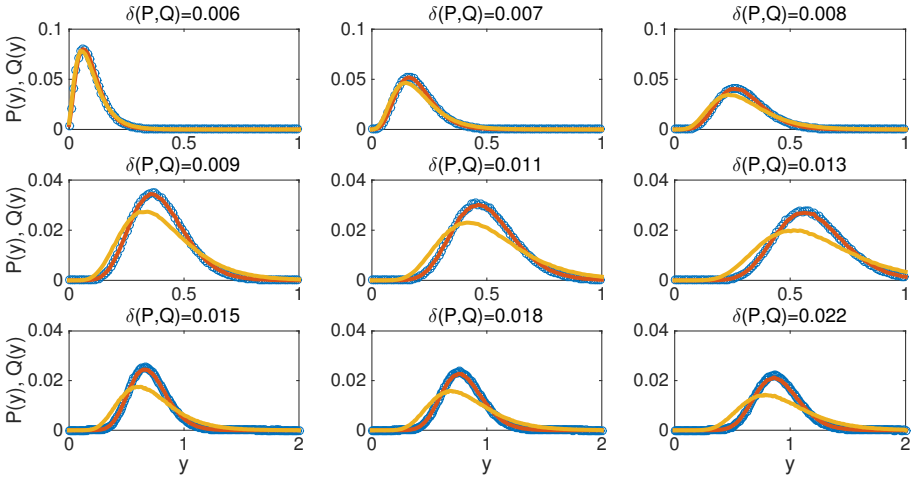

Figure 51. Comparison of distributions. Distribution of pathway output values from the *in silico* experiment without variation in global expression capacity (red), the corrected distribution inferred by the linearization approximation with this noise component removed (blue) and the original simulated data (orange). Each panel is at a different partner cell fraction θ_α, growing from left to right, from 0.1 (top left) to 0.9 (bottom right). The $\delta(P, Q)$ value shows the total variation distance between the corrected distribution and the 'data' from the *in silico* experiment without variation in global expression capacity.

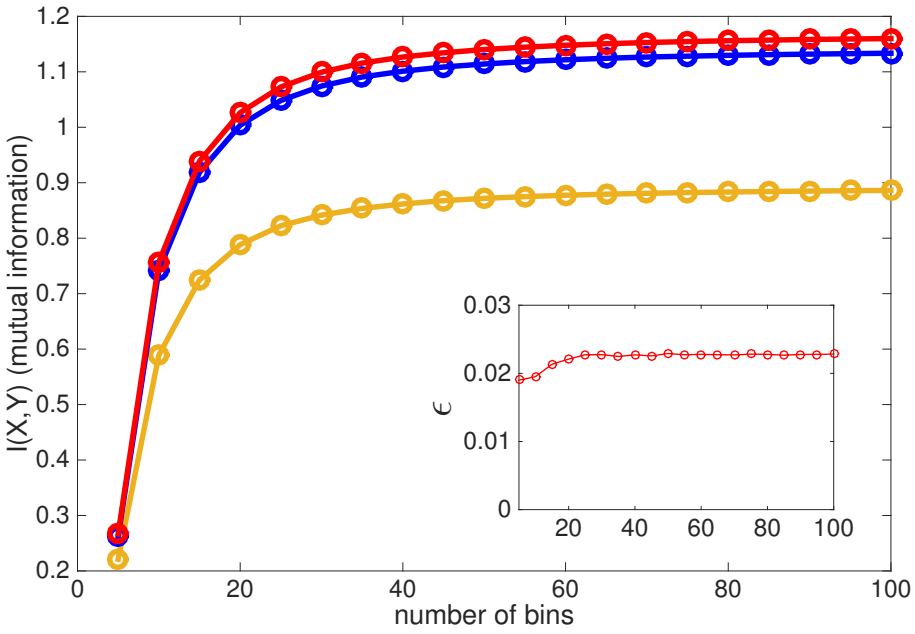

Figure 52. Mutual information estimates for the original (simulated) data (blue), the corrected distributions inferred by noise decomposition (red) and the *in silico* experiment without global expression capacity variation (orange). The inset shows the relative error of the corrected distribution's mutual information estimate from that of the *in silico* experiment without any variation in global expression capacity.

The method above relied on a number of assumptions. First of all the description of a gene's output as the product $y_i = P_i(G_i + \gamma_i)$ is highly schematic, and the assumption that global expression capacity (G) uniformly scales the output of different genes might not

be completely true. Another assumption is that the constitutive reporter's pathway capacity does not correlate (strongly) with global expression capacity ($\rho(P,G) \approx 0$), in the case of a doxycyline-induced repressor-system, repressor numbers are not compensated against (or amplified by) global expression capacity. For example, in a cell with a global expression capacity twice the population average (at a given doxycycline dose) the output would also be twice the population average, not less or more.

A further technical difficulty with actual experimental data is that different fluorophores, even when under the control of identical promoters will not have the same folding time or degradation dynamics. Therefore the marginal probability distributions of the gene outputs in a double-reporter experiment with identical promoters, which I used to infer η_γ, assuming marginal probability distribution for the two copies of each gene to have identical statistical properties, will not be the same. This is in effect another source of 'extrinsic' noise that I have not addressed above.

Despite these difficulties, the above analysis - based on experimental noise estimates - shows that double reporter experiments and noise decomposition through a schematic model of gene expression can be combined to give an improved estimate for the information transmission capacity of signaling pathways. A further question addressed by [130] is that the dynamics of signaling pathways can help to mitigate, and can potentially eliminate, extrinsic noise–induced information loss. Moreover, in the above analysis I quantified information transmission through a single output gene of a signaling pathway. If however a certain signaling pathway has multiple genes as outputs, the cell can also use this to extract more information about the pathway's input [136, 159].

4.2 Algebraic analysis of post-translational mechanisms in TC systems

4.2.1 Topology 2

Expressing SK, SKP and X_2 as functions of X_1:

$$SKP = \frac{X_1 c_\beta (c_0 + K_A c_1 X_1)}{c_0 c_\beta \kappa_1 R R_T - X_1 (K_A c_\alpha c_\beta + c_0 \kappa_1 (c_1 + c_\beta))}$$

$$SK = X_1 [\frac{c_\alpha c_\beta (c_0 + K_A c_1 X_1)}{c_0 (c_0 c_\beta \kappa_1 R R_T - X_1 (K_A c_\alpha c_\beta + c_0 \kappa_1 (c_1 + c_\beta)))} + \frac{c_1}{c_0}] = \frac{c_1}{c_0} X_1 + \frac{c_\alpha}{c_0} SKP$$

$$X_2 = K_A (X_1 [\frac{c_\alpha c_\beta (c_0 + K_A c_1 X_1)}{c_0 (c_0 c_\beta \kappa_1 R R_T - X_1 (K_A c_\alpha c_\beta + c_0 \kappa_1 (c_1 + c_\beta)))} + \frac{c_1}{c_0}]) (\frac{c_0 c_\beta \kappa_1 R R_T - X_1 (K_A c_\alpha c_\beta + c_0 \kappa_1 (c_1 + c_\beta))}{c_\beta \kappa_1 (c_0 + K_A c_1 X_1)}) =$$

$$= K_A X_1 \{\frac{c_\alpha}{c_0 \kappa_1} + \frac{c_1 (c_0 c_\beta \kappa_1 R R_T - X_1 (K_A c_\alpha c_\beta + c_0 \kappa_1 (c_1 + c_\beta)))}{c_0 c_\beta \kappa_1 (c_0 + K_A c_1 X_1)}\} = K_A X_1 \{\frac{c_\alpha c_\beta + c_1 \kappa_1 (R R_T c_\beta - (c_1 + c_\beta) X_1)}{c_\beta \kappa_1 (c_0 + K_A c_1 X_1)}\}$$

Then for the conservation equation of SK_T we get:

$SK_T = X_1 + \frac{c_1}{c_0}X_1 + (1 + \frac{c_\alpha}{c_0})[\frac{c_\beta(c_0+K_Ac_1X_1)X_1}{c_0c_\beta\kappa_1RR_T-(K_Ac_\alpha c_\beta+c_0\kappa_1(c_1+c_\beta)\ )X_1}] + K_A\{\frac{[c_\alpha c_\beta/\kappa_1+c_1c_\beta RR_T-c_1(c_1+c_\beta)X_1]X_1}{c_\beta(c_0+K_Ac_1X_1)}\}$

The first two terms are linearly increasing with X_1. For the last two terms, let us lump the parameters and write:

$\frac{c_\beta(c_0+K_Ac_1X_1)X_1}{c_0c_\beta\kappa_1RR_T-(K_Ac_\alpha c_\beta+c_0\kappa_1(c_1+c_\beta)\ )X_1}$ as $f(X_1) = \frac{(p_1+p_2X_1)X_1}{p_3-p_4X_1}$ and

$\frac{(c_\alpha c_\beta/\kappa_1+c_1c_\beta RR_T-c_1(c_1+c_\beta)X_1)X_1}{c_\beta(c_0+K_Ac_1X_1)}$ as $g(X_1) = \frac{(p_5-p_6X_1)X_1}{p_1+p_2X_1}$

Then the relation φ is $SK_T = \varphi(X_1) = \alpha X_1 + \beta\frac{(p_1+p_2X_1)X_1}{p_3-p_4X_1} + \gamma\frac{(p_5-p_6X_1)X_1}{p_1+p_2X_1}$.

$\alpha = (1 + \frac{c_1}{c_0})$, $\beta = (1 + \frac{c_\alpha}{c_0})$ and $\gamma = K_A$.

$p_1 = c_\beta c_0, p_2 = c_\beta c_1K_A, p_3 = c_0c_\beta\kappa_1RR_T, p_4 = K_Ac_\alpha c_\beta + c_0\kappa_1(c_1 + c_\beta), p_5 = \frac{c_\alpha c_\beta}{\kappa_1} + c_1c_\beta RR_T, p_6 = c_1(c_1 + c_\beta)$

To obtain positive values for SKP, $X_1 < \frac{p_3}{p_4}$ has to be true.

To obtain positive values for X_2, $X_1 < \frac{p_5}{p_6}$ has to be true.

The derivative of $f(X_1)$ is $\frac{\partial f}{\partial X_1} = \frac{2p_2p_3X_1+p_1p_3-p_2p_4X_1^2}{(p_3-p_4X_1)^2}$.

At $X_1 = 0$ the derivative $\frac{\partial f}{\partial X_1} = \frac{p_1p_3}{p_5}$, that is, positive.

At the maximal value $X_1 = \frac{p_3}{p_4}$, the numerator of $\frac{\partial f}{\partial X_1}$ equals $\frac{p_2p_3^2}{p_4} + p_1p_3$, which is also positive. Therefore, the parabola opens downward, and between the values of 0 and $\frac{p_3}{p_4}$ its value is always positive. Since the denominator is always positive, the derivative also has to be positive within the values 0 and $\frac{p_3}{p_4}$.

The interesting term is the last one, $g(X_1)$.

The derivative of g(X_1) is: $\frac{\partial g}{\partial X_1} = \frac{-p_2p_6X_1^2-2p_1p_6X_1+p_1p_5}{(p_1+p_2X_1)^2}$.

At $X_1 = 0$ the derivative $\frac{\partial g}{\partial X_1} = \frac{p_1}{p_5}$, that is, positive.

At the maximal value $X_1 = \frac{p_5}{p_6}$, the numerator of $\frac{\partial g}{\partial X_1}$ is $-p_1p_5 - \frac{p_2p_5^2}{p_6}$, that is, negative. In other words, if $min(\frac{p_5}{p_6}, \frac{p_3}{p_4}) > X_{1+}$, then the last term has an increasing and a decreasing part.

The positive root of the quadratic equation in the numerator is $X_{1+} = \frac{-p_1p_6+\sqrt{p_1p_6(p_1p_6+p_2p_5)}}{p_2p_6}$. Between 0 and this value $\frac{\partial g}{\partial X_1} > 0$, between X_{1+} and $\frac{p_5}{p_6}$, $\frac{\partial g}{\partial X_1} < 0$.

For multistationarity to be possible, there has to be three steady states (at least) in the range $X_1\epsilon\ [0, min(\frac{p_3}{p_4}, \frac{p_5}{p_6})]$, i.e. $\varphi(X_1) = \varphi(X_1^*) = \varphi(X_1^{**}) = SK_T$, with $X_1 \neq X_1^* \neq X_1^{**}$. At $X_1 = 0$ the function is increasing, therefore there has to be a range of X_1 values $0 < X_1 < min(\frac{p_3}{p_4}, \frac{p_5}{p_6})$ where $\varphi(X_1)' < 0$, and at $X_1 = min(\frac{p_3}{p_4}, \frac{p_5}{p_6})$ again $\varphi(X_1)' > 0$. In other words the function $\varphi(X_1)'$ has to have two roots in the range $0 \leq X_1 < min(\frac{p_3}{p_4}, \frac{p_5}{p_6})$, as φ and $\varphi(X_1)'$ are both continuous in this range.

As the first three terms are all positive in $X_1\epsilon\ [0, min(\frac{p_3}{p_4}, \frac{p_5}{p_6})]$, and the fourth term is positive in $X_1\epsilon\ [0, X_{1+}]$, $\varphi(X_1)' > 0$ is positive in $X_1\epsilon\ [0, X_{1+}]$.

Therefore, the 2 roots of $\varphi(X_1)'$ have to be in $X_1\epsilon\ [X_{1+}, min(\frac{p_3}{p_4}, \frac{p_5}{p_6})]$.

If $\frac{p_3}{p_4} > \frac{p_5}{p_6}$, then $X_1\epsilon\ [0, \frac{p_5}{p_6}]$, if $\frac{p_3}{p_4} < \frac{p_5}{p_6}$ then $X_1\epsilon\ [0, \frac{p_3}{p_4}]$.

The derivative of $\varphi(X_1)$ is:

$\varphi(X_1)' = \alpha + \beta(\frac{2p_2p_3X_1+p_1p_3-p_2p_4X_1^2}{(p_3-p_4X_1)^2}) + \gamma(\frac{-p_2p_6X_1^2-2p_1p_6X_1+p_1p_5}{(p_1+p_2X_1)^2})$

Which can be rewritten as a quartic polynomial. This polynomial has to have 2 roots in $X_1\epsilon\ [X_{1+}, min(\frac{p_5}{p_6}, \frac{p_3}{p_4})]$.

Numerical sampling in the parameters show that the derivative $\varphi(X_1)'$ can indeed have 2 roots in $X_1\epsilon\ [0, min(\frac{p_5}{p_6}, \frac{p_3}{p_4})]$, so there are values $X_1 \neq X_1^* \neq X_1^{**}$, that $\varphi(X_1) = \varphi(X_1^*) = \varphi(X_1^{**}) = SK_T$ is true.

4.2.2 Topology 5

Let us start with the first term, which is $\phi(RR)$, its constituent terms $g(RR) = \frac{1}{1+c_1/c_\beta}(\frac{c_1}{c_0} + \frac{c_\alpha}{c_0\kappa_1 RR})$ and $h(RR) = RR_T - \frac{RR(1+E1_TK_{a_1}+K_{a_1}RR)}{1+K_{a_1}RR}$, so that $\phi = g\ h$.

Following the chain rule of differentiation, $f'(RR) = g'h+gh'$. The function g is always positive for positive values of RR (not defined for RR = 0), and h has to be positive as well to yield a biologically meaningful value for SK.

Therefore, $RR\ \epsilon\ (0, \frac{-1+K_{a_1}(RR_T-E1_T)+\sqrt{4K_{a_1}RR_T+[1+K_{a_1}(E1_T-RR_T)]^2}}{2K_{a_1}}]$. As both g and h are strictly decreasing in RR, their derivatives are negative, therefore $\phi'(RR) = g'h + gh' < 0$.

The same reasoning can be applied to the second and third term (the latter one is simply the function $h(RR)$).

Turning to the last term, we note that $\phi(RR)$ is the same as the first term (SK) of the entire function φ, which is strictly decreasing in RR. It is the reciprocal of $\phi(RR)$ in the denominator of the fourth term, and $(\phi(RR)^{-1})' = -\frac{\phi(RR)'}{\phi(RR)^2}$. As shown above $\phi(RR)'$ is always negative, whereas the $\phi(RR)^2$ has to be positive, therefore $(\phi(RR)^{-1})' > 0$.

Then $\frac{\partial(K_{A3}\frac{E2_T}{1/\phi(RR)+K_{A3}})}{\partial RR} = -\frac{K_{A3}E2_T}{(1/\phi(RR)+K_{A3})^2}(-\frac{\phi(RR)'}{\phi(RR)^2}) = \frac{K_{A3}E2_T}{(1/\phi(RR)+K_{A3})^2}\frac{\phi(RR)'}{\phi(RR)^2}$.

As shown above, $\phi(RR)'$ is always negative, and the other terms are positive, therefore the whole term is always negative, meaning that the last term is strictly decreasing in RR.

We have therefore shown that all terms are strictly decreasing in the rational function φ,

4.2.3 Topology 6

Expressing SKP as a function of RRP, $f_1(\mathrm{RRP})$ from the conservation law on RR_T:

$$\boxed{SKP = f_1(RRP) = -RRP\frac{\mathrm{RRP}^3\kappa_2^2K_Ac_\beta^2 + \mathrm{RRP}^2p_8 + \mathrm{RRP}p_9 + c_0\left(c_\beta + c_2\kappa_2F_T\right)}{p_1\mathrm{RRP}^3 + p_2\mathrm{RRP}^2 + p_3\mathrm{RRP} - c_0c_1\kappa_1\mathrm{RR}_T}}$$

Where $p_1 = \kappa_2^2K_Ac_\alpha c_\beta + c_0\kappa_1\kappa_2^2c_\beta + c_0c_1\kappa_1\kappa_2^2$

$p_2 = c_2\kappa_2^2K_Ac_\alpha F_T + 2\kappa_2K_Ac_\alpha c_\beta + 2c_0\kappa_1\kappa_2c_\beta + c_0c_1\kappa_1\kappa_2^2F_T + c_0c_2\kappa_1\kappa_2^2F_T + 2c_0c_1\kappa_1\kappa_2 - c_0c_1\kappa_1\kappa_2^2\mathrm{RR}_T$

$p_3 = c_2\kappa_2K_Ac_\alpha F_T + K_Ac_\alpha c_\beta + c_0\kappa_1c_\beta + c_0c_1\kappa_1\kappa_2F_T + c_0c_2\kappa_1\kappa_2F_T + c_0c_1\kappa_1 - 2c_0c_1\kappa_1\kappa_2\mathrm{RR}_T.$

As the coefficients in the numerator are all positive, the denominator has to be negative, so that SKP is positive.

Expressing SK as a function of RRP, after some rearrangements:

$$\boxed{SK = f_2(\mathrm{RRP}) = RRP\frac{p_4\mathrm{RRP}^3 + p_5\mathrm{RRP}^2 + p_6\mathrm{RRP} - p_7}{p_1\mathrm{RRP}^3 + p_2\mathrm{RRP}^2 + p_3\mathrm{RRP} - c_0c_1\kappa_1\mathrm{RRT}}}$$

Where

$p_4 = \kappa_1\kappa_2^2c_\beta^2 + c_1\kappa_1\kappa_2^2c_\beta$

$p_5 = \kappa_2\left(c_1\kappa_1\left(c_\beta\left(\kappa_2F_T - \kappa_2\mathrm{RR}_T + 2\right) + c_2\kappa_2F_T\right) + c_\beta\left(2\kappa_1c_\beta - \kappa_2\left(c_\alpha - 2c_2\kappa_1F_T\right)\right)\right)$

$p_6 = \kappa_1c_\beta^2 + c_1\kappa_1[c_\beta\left(\kappa_2F_T - 2\kappa_2\mathrm{RR}_T + 1\right) + c_2\kappa_2F_T\left(\kappa_2F_T - \kappa_2\mathrm{RR}_T + 1\right)]$

$-2\kappa_2c_\beta\left(c_\alpha - c_2\kappa_1F_T\right) + c_2\kappa_2^2F_T\left(c_2\kappa_1F_T - c_\alpha\right)$

$p_7 = \left(c_\beta + c_2\kappa_2F_T\right)\left(c_\alpha + c_1\kappa_1\mathrm{RR}_T\right)$

Expressing X_1 as a function of RRP:

$$\boxed{X_1 = f_3(\mathrm{RRP}) = \frac{\mathrm{RRP}\left(c_\beta + \frac{(c_2\kappa_2)F_T}{\kappa_2\mathrm{RRP}+1}\right)}{c_1}}$$

Expressing $X_2 = f_4(\mathrm{RRP})$

$$\boxed{X_2 = f_4(RRP) = -K_A\mathrm{RRP}\frac{\left(p_4\mathrm{RRP}^3 + p_5\mathrm{RRP}^2 + p_6\mathrm{RRP} - p_7\right)}{c_1\kappa_1[\mathrm{RRP}^3\kappa_2^2K_Ac_\beta + \mathrm{RRP}^2p_{10} + \mathrm{RRP}p_{11} + c_0]}}$$

As the denominator is always positive, the numerator $p_4\mathrm{RRP}^3 + p_5\mathrm{RRP}^2 + p_6\mathrm{RRP} - p_7$ has to be negative to obtain positive values for X_2.

Using the conservation identity for SK_T :

$\varphi(RRP) = SK + SKP + X_1 + X_2 = f_2(\mathrm{RRP}) + f_1(\mathrm{RRP}) + f_3(\mathrm{RRP}) + f_4(\mathrm{RRP})$

$SK_T = \varphi(RRP) = f_2(\mathrm{RRP}) + f_1(\mathrm{RRP}) + f_3(\mathrm{RRP}) + f_4(\mathrm{RRP})$

$f_3(\mathrm{RRP})(X_1)$ is strictly increasing in RRP, but the other terms' derivatives can all change sign several times in the range $RRP \,\epsilon\, [0, RR_T]$.

The derivatives are:

$f_1(\mathrm{RRP})' = \frac{\sum_{i=0}^{6} \alpha_i RRP^i}{[\mathrm{RRP}(p_1\mathrm{RRP}^2+p_2\mathrm{RRP}+p_3)-c_0\mathrm{RRT}(c_1+\kappa_1)]^2}$

$\alpha_0, \alpha_1 > 0$, $\alpha_5, \alpha_6 < 0$ and $\alpha_2, \alpha_3, \alpha_4$ can be either 0, negative or positive.

$f_2(\mathrm{RRP})' = \frac{\sum_{i=0}^{6} \beta_i RRP^i}{[\mathrm{RRP}(p_1\mathrm{RRP}^2+p_2\mathrm{RRP}+p_3)-c_0\mathrm{RRT}(c_1+\kappa_1)]^2}$

$\beta_5, \beta_6 > 0$, $\beta_0 < 0$ and $\beta_1, \beta_2, \beta_3, \beta_4$ can be either 0, negative or positive.

$f_3(\mathrm{RRP})' = \frac{\kappa_1\left(c_2\kappa_2 F_T + c_\beta(\kappa_2\mathrm{RRP}+1)^2\right)}{(c_1+\kappa_1)(\kappa_2\mathrm{RRP}+1)^2}$

The derivative $f_3(\mathrm{RRP})'$ (X_1') is always positive, therefore X_1 is strictly increasing in RRP.

$f_4(\mathrm{RRP})' = -K_A \frac{\sum_{i=0}^{6} \gamma_i RRP^i}{c_1\kappa_1(\kappa_2\mathrm{RRP}+1)^2(\mathrm{RRP}K_A(c_2\kappa_2 F_T + c_\beta(\kappa_2\mathrm{RRP}+1))+c_0(\kappa_2\mathrm{RRP}+1))^2}$

$\gamma_0, \gamma_5, \gamma_6 < 0$, and $\gamma_1, \gamma_2, \gamma_3, \gamma_4$ can be either negative, 0 or positive.

Multistationarity is possible if

a) the function φ is continuous, then the derivative φ' has to have at least 2 roots in the range $RRP \,\epsilon\, [0, RR_T]$ for $\varphi(RRP_1) = \varphi(RRP_2) = \varphi(RRP_3), RRP_1 \neq RRP_2 \neq RRP_3$ to be true.

or

b) there are discontinuities in the range $RRP \,\epsilon\, [0, RR_T]$, then the derivative φ' does not have to have multiple roots for $\varphi(RRP_1) = \varphi(RRP_2) = \varphi(RRP_3), RRP_1 \neq RRP_2 \neq RRP_3$ to be true. The terms SKP and SK have a singularity if $p_1\mathrm{RRP}^3 + p_2\mathrm{RRP}^2 + p_3\mathrm{RRP} - (c_1+\kappa_1)\mathrm{RR}_T = 0$. No other discontinuities are possible, because the other denominators cannot be 0.

$p_1\mathrm{RRP}^3 + p_2\mathrm{RRP}^2 + p_3\mathrm{RRP} - (c_1+\kappa_1)\mathrm{RR}_T = 0$ can only have one positive root.

This is because $p_2/\kappa_2 > p_3$, therefore if p_2 is negative, then p_3 is also negative. p_1 is always positive, and the last term's sign is always negative. Therefore the possible signs of the coefficients are thus { + - - - }, {+ + + - } or { + + - - }, therefore according to Descartes's rule of signs, there can only be one positive solution.

As $p_1\mathrm{RRP}^3+p_2\mathrm{RRP}^2+p_3\mathrm{RRP}-(c_1+\kappa_1)$ is negative at $RRP = 0$, and positive at $RRP = RR_T$, the real positive root of $p_1\mathrm{RRP}^3 + p_2\mathrm{RRP}^2 + p_3\mathrm{RRP} - (c_1+\kappa_1)$ has to be in $RRP \,\epsilon\, [0, RR_T]$. However, for values larger than the root, RRP_+ , $p_1\mathrm{RRP}^3 + p_2\mathrm{RRP}^2 + p_3\mathrm{RRP} - (c_1+\kappa_1) > 0$, which would make SK negative, and therefore not admissible. Consequently, the function φ is only defined $RRP \,\epsilon\, [0, RRP_+]$. In this range however, the function is continuous and multistationarity is only possible in case *a*).

If the function is continuous (as I have showed it has to be in the physically meaningful range), we can find multistationary solutions in the following way.

We perform numerical sampling for the parameters $c_0, c_\alpha, a_1, d_1, c_1, a_\gamma, d_\gamma, a_2, d_2, c_2$ and RR_T and solve the equation $\varphi(RRP)' = f_1(\mathrm{RRP})' + f_2(\mathrm{RRP})' + f_3(\mathrm{RRP})' + f_4(\mathrm{RRP})' = 0$ numerically.

If the equation has multiple solutions $RRP \in [0, RR_T]$, then at some SK_T value(s) the given parameter set exhibits multistationarity. Substituting the RRP values where the roots are located back into the equation $\varphi(RRP)$, we obtain the SK_T values between which the parameter set exhibits multistationary behavior.

4.3 Algebraic analysis of feedback mechanisms in TC systems: using a Hill-equation instead of explicit dimerization.

In the model including transcriptional feedback in Section 2.4, I used a Hill-equation with a cooperativity index of 2, to model the nonlinearity introduced by dimerization of activated transcription factors (RRP). I show here that this approximation is legitimate. I start by a standard model of transcription [73, 125], with the rate of transcription proportional to the fractional occupancy of the promoter by its transcription factor x:

$$v_{transcr} = \frac{x}{x + K} \tag{115}$$

I take a self-inducing system, producing the protein x, with x dimerizing and binding to its own promoter, thereby inducing its own expression. It is the dimer that binds to the operator site, therefore the fractional occupancy of the latter scales with the dimer concentration as with x in Equation 115. Treating the mono- and dimeric versions of the protein as separate variables I can describe the system as in Equation 116 below. One feature of the system neglected here is that some of the dimer pool is bound to the operator site.

$$\begin{aligned} \dot{x}(t) = \left(\beta + \phi\frac{d(t)}{d(t) + K} - \gamma_1 x(t)\right) + \left(2k_{off}d(t) - 2k_{on}x(t)^2\right) \\ \dot{d}(t) = k_{on}x(t)^2 - (k_{off} + \gamma_2)d(t) \end{aligned} \tag{116}$$

It is easy to see that in the case of the degradation rate γ_2 of the dimer being zero, in steady state $d = \frac{k_{on}}{k_{off}}x^2$. This simplifies the first equation to the quadratic Hill-equation (setting $k_{on} = k_{off} = 1$), and in steady state the equation is:

$$0 = \beta + \phi\frac{x^2}{x^2 + K} - \gamma x \tag{117}$$

This equation can have three roots. We can obtain the range of bistability by rearranging the equation, treating the basal expression rate β as the dependent variable: $\beta = \gamma x - \phi\frac{x^2}{x^2+K}$. With that I assume that β is the input parameter of the system. The derivative with respect to x of the right-hand side of the equation is $\frac{\partial\beta}{\partial x} = \frac{x^4+2x^2-2\phi x+1}{(x^2+1)^2}$.

The (real and positive) roots of the derivative are the bifurcation points and define the range of bistability, as shown in Figure 53 for the parameter values $\phi = 1.8$, $K = 1$. The total concentration of x at steady state is $x_T = x + x^2$.

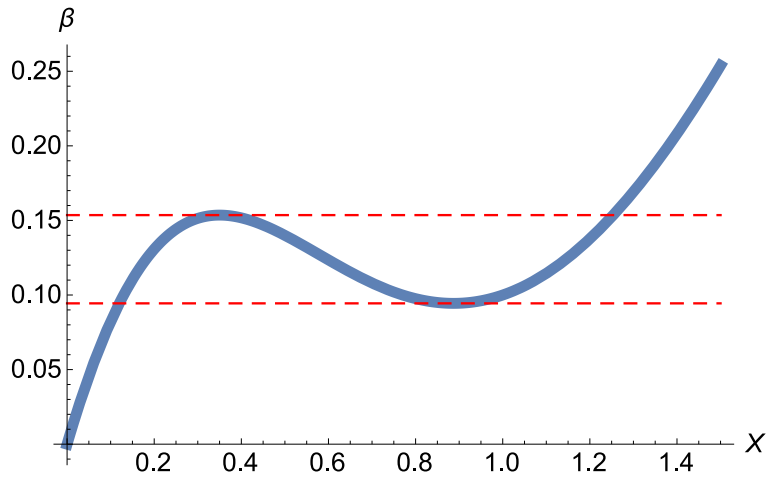

Figure 53. Bistable range of an auto-inducing transcriptional system with dimerization of the transcription factor.

If instead we describe the system by not having a dimer fraction, so now the entire system is simply:

$$\dot{x}(t) = \beta + \phi \frac{x(t)^2}{x(t)^2 + K} - \gamma_1 x(t) \tag{118}$$

The steady state equation and its bistability range will be the same, the roots of $\frac{\partial \beta}{\partial x} = \frac{x^4+2x^2-2\phi x+1}{(x^2+1)^2} = 0$. In this case however, the solutions for x stand for the total pool of protein, as now $x_T = x$.

Since in Section 2.4 our goal was to detect the existence of bistability and to determine the relative range of bistability in terms of both the input and the output, this simplification does not qualitatively change the results.

References

[1] Phillip Aldridge, Ralf Paul, Patrick Goymer, Paul Rainey, and Urs Jenal. "Role of the GGDEF regulator PleD in polar development of Caulobacter crescentus". In: *Molecular microbiology* 47.6 (2003), pp. 1695–1708.

[2] Rui Alves and Michael A Savageau. "Comparative analysis of prototype two-component systems with either bifunctional or monofunctional sensors: differences in molecular structure and physiological function". In: *Molecular microbiology* 48.1 (2003), pp. 25–51.

[3] Munia Amin, Varun B Kothamachu, Elisenda Feliu, Birgit E Scharf, Steven L Porter, and Orkun S Soyer. "Phosphate sink containing two-component signaling systems as tunable threshold devices". In: *PLOS Comput Biol* 10.10 (2014), e1003890.

[4] Munia Amin, Steven L Porter, and Orkun S Soyer. "Split histidine kinases enable ultrasensitivity and bistability in two-component signaling networks". In: *PLoS Comput Biol* 9.3 (2013), e1002949.

[5] James B Anderson, Caroline Sirjusingh, and Nicole Ricker. "Haploidy, diploidy and evolution of antifungal drug resistance in Saccharomyces cerevisiae". In: *Genetics* 168.4 (2004), pp. 1915–1923.

[6] David Angeli, James E Ferrell, and Eduardo D Sontag. "Detection of multistability, bifurcations, and hysteresis in a large class of biological positive-feedback systems". In: *Proceedings of the National Academy of Sciences of the United States of America* 101.7 (2004), pp. 1822–1827.

[7] David Angeli and Eduardo D Sontag. "Multi-stability in monotone input/output systems". In: *Systems & Control Letters* 51.3 (2004), pp. 185–202.

[8] Janis Antonovics and Norman C Ellstrand. "Experimental studies of the evolutionary significance of sexual reproduction. I. A test of the frequency-dependent selection hypothesis". In: *Evolution* (1984), pp. 103–115.

[9] Robert A Arkowitz. "Chemical gradients and chemotropism in yeast". In: *Cold Spring Harbor perspectives in biology* 1.2 (2009), a001958.

[10] Gabor Balazsi, Alexander van Oudenaarden, and James J Collins. "Cellular decision making and biological noise: from microbes to mammals". In: *Cell* 144.6 (2011), pp. 910–925.

[11] Natalya Baranova and Hiroshi Nikaido. “The baeSR two-component regulatory system activates transcription of the yegMNOB (mdtABCD) transporter gene cluster in Escherichia coli and increases its resistance to novobiocin and deoxycholate”. In: *Journal of bacteriology* 184.15 (2002), pp. 4168–4176.

[12] Lee Bardwell. “A walk-through of the yeast mating pheromone response pathway”. In: *Peptides* 25.9 (2004), pp. 1465–1476.

[13] Naama Barkai, Mark D Rose, and Ned S Wingreen. “Protease helps yeast find mating partners”. In: *Nature* 396.6710 (1998), pp. 422–423.

[14] Kanadpriya Basu and Xinfeng Liu. “Mathematical modeling for multisite phosphorylation with scaffold binding in cell signaling”. In: *Mathematical Methods in the Applied Sciences* 38.18 (2015), pp. 4521–4529.

[15] Howard C Berg. *E. coli in Motion*. Springer Science & Business Media, 2008.

[16] Howard C Berg. *Random walks in biology*. Princeton University Press, 1993.

[17] Howard C Berg and Edward M Purcell. “Physics of chemoreception.” In: *Biophysical journal* 20.2 (1977), p. 193.

[18] Howard C Berg, Douglas A Brown, et al. “Chemotaxis in Escherichia coli analysed by three-dimensional tracking”. In: *Nature* 239.5374 (1972), pp. 500–504.

[19] Upinder Singh Bhalla. “Trafficking motifs as the basis for two-compartment signaling systems to form multiple stable states”. In: *Biophysical journal* 101.1 (2011), pp. 21–32.

[20] John A Birdsell and Christopher Wills. “The evolutionary origin and maintenance of sexual recombination: a review of contemporary models”. In: *Evolutionary Biology*. Springer, 2003, pp. 27–138.

[21] Marc R Birtwistle, Alexander von Kriegsheim, Maciej Dobrzynski, Boris N Kholodenko, and Walter Kolch. “Mammalian protein expression noise: scaling principles and the implications for knockdown experiments”. In: *Molecular BioSystems* 8.11 (2012), pp. 3068–3076.

[22] Marc R Birtwistle, Jens Rauch, Anatoly Kiyatkin, Edita Aksamitiene, Maciej Dobrzyński, Jan B Hoek, Walter Kolch, Babatunde A Ogunnaike, and Boris N Kholodenko. “Emergence of bimodal cell population responses from the interplay between analog single-cell signaling and protein expression noise”. In: *BMC systems biology* 6.1 (2012), p. 1.

[23] Steven M Block, Jeffrey E Segall, and Howard C Berg. “Impulse responses in bacterial chemotaxis”. In: *Cell* 31.1 (1982), pp. 215–226.

[24] Nils Blüthgen, Frank J Bruggeman, Stefan Legewie, Hanspeter Herzel, Hans V Westerhoff, and Boris N Kholodenko. "Effects of sequestration on signal transduction cascades". In: *Febs Journal* 273.5 (2006), pp. 895–906.

[25] Clive G Bowsher and Peter S Swain. "Environmental sensing, information transfer, and cellular decision-making". In: *Current opinion in biotechnology* 28 (2014), pp. 149–155.

[26] Sebastian Bubendorfer, Susanne Held, Natalie Windel, Anja Paulick, Andreas Klingl, and Kai M Thormann. "Specificity of motor components in the dual flagellar system of Shewanella putrefaciens CN-32". In: *Molecular microbiology* 83.2 (2012), pp. 335–350.

[27] Sebastian Bubendorfer, Mihaly Koltai, Florian Rossmann, Victor Sourjik, and Kai M Thormann. "Secondary bacterial flagellar system improves bacterial spreading by increasing the directional persistence of swimming". In: *Proceedings of the National Academy of Sciences* 111.31 (2014), pp. 11485–11490.

[28] Long Cai, Nir Friedman, and X Sunney Xie. "Stochastic protein expression in individual cells at the single molecule level". In: *Nature* 440.7082 (2006), pp. 358–362.

[29] Emily J Capra and Michael T Laub. "The Evolution of Two-Component Signal Transduction Systems". In: *Annual review of microbiology* 66 (2012), p. 325.

[30] Yunrong Chai, Frances Chu, Roberto Kolter, and Richard Losick. "Bistability and biofilm formation in Bacillus subtilis". In: *Molecular microbiology* 67.2 (2008), pp. 254–263.

[31] Smarajit Chakraborty, J Sivaraman, Ka Yin Leung, and Yu-Keung Mok. "Two-component PhoB-PhoR regulatory system and ferric uptake regulator sense phosphate and iron to control virulence genes in type III and VI secretion systems of Edwardsiella tarda". In: *Journal of Biological Chemistry* 286.45 (2011), pp. 39417–39430.

[32] Carlo Chan, Xinfeng Liu, Liming Wang, Lee Bardwell, Qing Nie, and German Enciso. "Protein scaffolds can enhance the bistability of multisite phosphorylation systems". In: *PLoS Comput Biol* 8.6 (2012), e1002551.

[33] Raymond Cheong, Alex Rhee, Chiaochun Joanne Wang, Ilya Nemenman, and Andre Levchenko. "Information Transduction Capacity of Noisy Biochemical Signaling Networks". In: *Science* 334.6054 (2011), pp. 1–11.

[34] Damon A Clark and Lars C Grant. "The bacterial chemotactic response reflects a compromise between transient and steady-state behavior". In: *Proceedings of the National Academy of Sciences of the United States of America* 102.26 (2005), pp. 9150–9155.

[35] Alejandro Colman-Lerner, Andrew Gordon, Eduard Serra, Tina Chin, Orna Resnekov, Drew Endy, C Gustavo Pesce, and Roger Brent. "Regulated cell-to-cell variation in a cell-fate decision system". In: *Nature* 437.29 (2005), pp. 699–706.

[36] Alison E Coluccio, Rachael K Rodriguez, Maurice J Kernan, and Aaron M Neiman. "The yeast spore wall enables spores to survive passage through the digestive tract of Drosophila". In: *PLoS One* 3.8 (2008), e2873.

[37] James F Crow. "Advantages of sexual reproduction". In: *Developmental genetics* 15.3 (1994), pp. 205–213.

[38] Erez Dekel and Uri Alon. "Optimality and evolutionary tuning of the expression level of a protein". In: *Nature* 436.7050 (2005), pp. 588–592.

[39] J Barrett Deris, Minsu Kim, Zhongge Zhang, Hiroyuki Okano, Rutger Hermsen, Alexander Groisman, and Terence Hwa. "The innate growth bistability and fitness landscapes of antibiotic-resistant bacteria". In: *Science* 342.6162 (2013), p. 1237435.

[40] Peter Devreotes and Chris Janetopoulos. "Eukaryotic chemotaxis: distinctions between directional sensing and polarization". In: *Journal of biological chemistry* 278.23 (2003), pp. 20445–20448.

[41] Christian Diener, Gabriele Schreiber, Wolfgang Giese, Gabriel del Rio, Andreas Schröder, and Edda Klipp. "Yeast Mating and Image-Based Quantification of Spatial Pattern Formation". In: *PLoS Computational Biology* 10.6 (2014).

[42] David Dubnau and Richard Losick. "Bistability in bacteria". In: *Molecular microbiology* 61.3 (2006), pp. 564–572.

[43] Michael B Elowitz, Arnold J Levine, Eric D Siggia, and Peter S Swain. "Stochastic gene expression in a single cell". In: *Science* 297.5584 (2002), pp. 1183–1186.

[44] Fanny Ewann, Mary Jackson, Kevin Pethe, Andrea Cooper, Nathalie Mielcarek, Danielle Ensergueix, Brigitte Gicquel, Camille Locht, and Philip Supply. "Transient requirement of the PrrA-PrrB two-component system for early intracellular multiplication of Mycobacterium tuberculosis". In: *Infection and immunity* 70.5 (2002), pp. 2256–2263.

[45] Martin Feinberg. "Chemical reaction network structure and the stability of complex isothermal reactors—I. The deficiency zero and deficiency one theorems". In: *Chemical Engineering Science* 42.10 (1987), pp. 2229–2268.

[46] Martin Feinberg. “Chemical reaction network structure and the stability of complex isothermal reactors—II. Multiple steady states for networks of deficiency one”. In: *Chemical Engineering Science* 43.1 (1988), pp. 1–25.

[47] Elisenda Feliu, Michael Knudsen, Lars N Andersen, and Carsten Wiuf. “An algebraic approach to signaling cascades with n layers”. In: *Bulletin of mathematical biology* 74.1 (2012), pp. 45–72.

[48] Elisenda Feliu and Carsten Wiuf. “Enzyme-sharing as a cause of multi-stationarity in signalling systems”. In: *Journal of The Royal Society Interface* (2011), rsif20110664.

[49] Elisenda Feliu and Carsten Wiuf. “Simplifying biochemical models with intermediate species”. In: *Journal of The Royal Society Interface* 10.87 (2013), p. 20130484.

[50] James E Ferrell Jr and Wen Xiong. “Bistability in cell signaling: How to make continuous processes discontinuous, and reversible processes irreversible”. In: *Chaos: An Interdisciplinary Journal of Nonlinear Science* 11.1 (2001), pp. 227–236.

[51] James E Ferrell. “Self-perpetuating states in signal transduction: positive feedback, double-negative feedback and bistability”. In: *Current opinion in cell biology* 14.2 (2002), pp. 140–148.

[52] James E Ferrell and Eric M Machleder. “The biochemical basis of an all-or-none cell fate switch in Xenopus oocytes”. In: *Science* 280.5365 (1998), pp. 895–898.

[53] Nir Friedman, Long Cai, and X Sunney Xie. “Linking stochastic dynamics to population distribution: an analytical framework of gene expression”. In: *Physical review letters* 97.16 (2006), p. 168302.

[54] Koichi Fujimoto and Satoshi Sawai. “A design principle of group-level decision making in cell populations”. In: *PLoS Comput. Biol* 9 (2013), e1003110.

[55] Masaya Fujita, José Eduardo González-Pastor, and Richard Losick. “High-and low-threshold genes in the Spo0A regulon of Bacillus subtilis”. In: *Journal of bacteriology* 187.4 (2005), pp. 1357–1368.

[56] Masaya Fujita and Yoshito Sadaie. “Feedback loops involving Spo0A and AbrB in in vitro transcription of the genes involved in the initiation of sporulation in Bacillus subtilis”. In: *Journal of biochemistry* 124.1 (1998), pp. 98–104.

[57] Michael Y Galperin. “Structural classification of bacterial response regulators: diversity of output domains and domain combinations”. In: *Journal of bacteriology* 188.12 (2006), pp. 4169–4182.

[58] Rong Gao, Timothy R Mack, and Ann M Stock. "Bacterial response regulators: versatile regulatory strategies from common domains". In: *Trends in biochemical sciences* 32.5 (2007), pp. 225–234.

[59] Timothy S Gardner, Charles R Cantor, and James J Collins. "Construction of a genetic toggle switch in Escherichia coli". In: *Nature* 403.6767 (2000), pp. 339–342.

[60] Aleeza C Gerstein and Sarah P Otto. "Cryptic fitness advantage: diploids invade haploid populations despite lacking any apparent advantage as measured by standard fitness assays". In: *PloS one* 6.12 (2011), e26599.

[61] Sayantari Ghosh, Kamakshi Sureka, Bhaswar Ghosh, Indrani Bose, Joyoti Basu, and Manikuntala Kundu. "Phenotypic heterogeneity in mycobacterial stringent response". In: *BMC systems biology* 5.1 (2011), p. 18.

[62] Daniel T Gillespie. "Exact stochastic simulation of coupled chemical reactions". In: *The journal of physical chemistry* 81.25 (1977), pp. 2340–2361.

[63] Eli S Groban, Elizabeth J Clarke, Howard M Salis, Susan M Miller, and Christopher A Voigt. "Kinetic buffering of cross talk between bacterial two-component sensors". In: *Journal of molecular biology* 390.3 (2009), pp. 380–393.

[64] Eduardo A Groisman. "The pleiotropic two-component regulatory system PhoP-PhoQ". In: *Journal of bacteriology* 183.6 (2001), pp. 1835–1842.

[65] Swapna Aravind Gudipaty, Andrew S Larsen, Christopher Rensing, and Megan M McEvoy. "Regulation of Cu (I)/Ag (I) efflux genes in Escherichia coli by the sensor kinase CusS". In: *FEMS microbiology letters* 330.1 (2012), pp. 30–37.

[66] Gianluca M Guidi and Albert Goldbeter. "Bistability without hysteresis in chemical reaction systems: a theoretical analysis of irreversible transitions between multiple steady states". In: *The Journal of Physical Chemistry A* 101.49 (1997), pp. 9367–9376.

[67] Jeremy Gunawardena. "Multisite protein phosphorylation makes a good threshold but can be a poor switch". In: *Proceedings of the National Academy of Sciences of the United States of America* 102.41 (2005), pp. 14617–14622.

[68] Heather A Harrington, Elisenda Feliu, Carsten Wiuf, and Michael PH Stumpf. "Cellular compartments cause multistability and allow cells to process more information". In: *Biophysical journal* 104.8 (2013), pp. 1824–1831.

[69] Joseph Heitman. "Sexual reproduction and the evolution of microbial pathogens". In: *Current Biology* 16.17 (2006), R711–R725.

[70] Alistair Howell, Sarah Dubrac, Kasper Krogh Andersen, David Noone, Juliette Fert, Tarek Msadek, and Kevin Devine. “Genes controlled by the essential YycG/YycF two-component system of Bacillus subtilis revealed through a novel hybrid regulator approach”. In: *Molecular microbiology* 49.6 (2003), pp. 1639–1655.

[71] Michele M Igo, Alexander J Ninfa, Jeffry B Stock, and Thomas J Silhavy. “Phosphorylation and dephosphorylation of a bacterial transcriptional activator by a transmembrane receptor.” In: *Genes & development* 3.11 (1989), pp. 1725–1734.

[72] Oleg A Igoshin, Rui Alves, and Michael A Savageau. “Hysteretic and graded responses in bacterial two-component signal transduction”. In: *Molecular microbiology* 68.5 (2008), pp. 1196–1215.

[73] Brian P Ingalls. *Mathematical Modeling in Systems Biology - An Introduction*. MIT Press, 2013.

[74] Meng Jin, Beverly Errede, Marcelo Behar, Will Mather, Sujata Nayak, Jeff Hasty, Henrik G Dohlman, and Timothy C Elston. “Yeast dynamically modify their environment to achieve better mating efficiency”. In: *Science signaling* 4.186 (2011), ra54.

[75] PM Kareiva and N Shigesada. “Analyzing insect movement as a correlated random walk”. In: *Oecologia* 56.2-3 (1983), pp. 234–238.

[76] Francis X Kelly, Karen J Dapsis, and Douglas A Lauffenburger. “Effect of bacterial chemotaxis on dynamics of microbial competition”. In: *Microbial Ecology* 16.2 (1988), pp. 115–131.

[77] Andrzej M Kierzek, Lu Zhou, and Barry L Wanner. “Stochastic kinetic model of two component system signalling reveals all-or-none, graded and mixed mode stochastic switching responses”. In: *Molecular bioSystems* 6.3 (2010), pp. 531–542.

[78] Yoosik Kim, Ze’ev Paroush, Knud Nairz, Ernst Hafen, Gerardo Jimenez, and Stanislav Y Shvartsman. “Substrate-dependent control of MAPK phosphorylation in vivo”. In: *Molecular systems biology* 7.1 (2011), p. 467.

[79] Michael Knop. “Evolution of the hemiascomycete yeasts: on life styles and the importance of inbreeding”. In: *Bioessays* 28.7 (2006), pp. 696–708.

[80] Bente Kofahl and Edda Klipp. “Modelling the dynamics of the yeast pheromone pathway”. In: *Yeast* 21.10 (2004), pp. 831–850.

[81] Markus Kollmann, Linda Lovdok, Kilian Bartholome, Jens Timmer, and Victor Sourjik. "Design principles of a bacterial signalling network". In: *Nature* 438.7067 (2005), pp. 504–507.

[82] Kristin K Koretke, Andrei N Lupas, Patrick V Warren, Martin Rosenberg, and James R Brown. "Evolution of two-component signal transduction". In: *Molecular Biology and Evolution* 17.12 (2000), pp. 1956–1970.

[83] Varun B Kothamachu, Elisenda Feliu, Luca Cardelli, and Orkun S Soyer. "Unlimited multistability and Boolean logic in microbial signalling". In: *Journal of the Royal Society interface* 12.108 (2015), p. 20150234.

[84] Tobias Kraxenberger, Luitpold Fried, Stefan Behr, and Kirsten Jung. "First insights into the unexplored two-component system YehU/YehT in Escherichia coli". In: *Journal of bacteriology* 194.16 (2012), pp. 4272–4284.

[85] Edo Kussell and Stanislas Leibler. "Phenotypic diversity, population growth, and information in fluctuating environments". In: *Science* 309.5743 (2005), pp. 2075–2078.

[86] Martin G Lamarche, Barry L Wanner, Sebastien Crepin, and Josee Harel. "The phosphate regulon and bacterial virulence: a regulatory network connecting phosphate homeostasis and pathogenesis". In: *FEMS microbiology reviews* 32.3 (2008), pp. 461–473.

[87] Michael T Laub and Mark Goulian. "Specificity in two-component signal transduction pathways". In: *Annu. Rev. Genet.* 41 (2007), pp. 121–145.

[88] Douglas A Lauffenburger. "Quantitative studies of bacterial chemotaxis and microbial population dynamics". In: *Microbial Ecology* 22.1 (1991), pp. 175–185.

[89] Stefan Legewie, Birgit Schoeberl, Nils Blüthgen, and Hanspeter Herzel. "Competing docking interactions can bring about bistability in the MAPK cascade". In: *Biophysical journal* 93.7 (2007), pp. 2279–2288.

[90] David A. Levin, Yuval Peres, and Wilmer Elizabeth L. *Markov Chains and Mixing Times.* American Mathematical Society, 2008.

[91] Hui Li and Victor Sourjik. "Assembly and stability of flagellar motor in Escherichia coli". In: *Molecular microbiology* 80.4 (2011), pp. 886–899.

[92] Peter N Lipke and Janet Kurjan. "Sexual agglutination in budding yeasts: structure, function, and regulation of adhesion glycoproteins." In: *Microbiological reviews* 56.1 (1992), pp. 180–194.

[93] David G Lloyd. “Benefits and handicaps of sexual reproduction”. In: *Evolutionary biology*. Springer, 1980, pp. 69–111.

[94] Janos Tobias Locsei. “Persistence of direction increases the drift velocity of run and tumble chemotaxis”. In: *Journal of mathematical biology* 55.1 (2007), pp. 41–60.

[95] Barbara K Mable and Sarah P Otto. “Masking and purging mutations following EMS treatment in haploid, diploid and tetraploid yeast (Saccharomyces cerevisiae)”. In: *Genetical research* 77.01 (2001), pp. 9–26.

[96] Vivian L MacKay, SK Welch, Margaret Y Insley, Thomas R Manney, Julie Holly, Gena C Saari, and Michael L Parker. “The Saccharomyces cerevisiae BAR1 gene encodes an exported protein with homology to pepsin”. In: *Proceedings of the National Academy of Sciences* 85.1 (1988), pp. 55–59.

[97] Nick I Markevich, Jan B Hoek, and Boris N Kholodenko. “Signaling switches and bistability arising from multisite phosphorylation in protein kinase cascades”. In: *The Journal of cell biology* 164.3 (2004), pp. 353–359.

[98] Megan N McClean, Areez Mody, James R Broach, and Sharad Ramanathan. “Cross-talk and decision making in MAP kinase pathways”. In: *Nature genetics* 39.3 (2007), pp. 409–414.

[99] Thomas Millat, Eric Bullinger, Johann Rohwer, and Olaf Wolkenhauer. “Approximations and their consequences for dynamic modelling of signal transduction pathways”. In: *Mathematical biosciences* 207.1 (2007), pp. 40–57.

[100] Thomas Millat, Sree N Sreenath, Radina P Soebiyanto, Jayant Avva, Kwang-Hyun Cho, and Olaf Wolkenhauer. “The role of dynamic stimulation pattern in the analysis of bistable intracellular networks”. In: *Biosystems* 92.3 (2008), pp. 270–281.

[101] Amir Mitchell, Ping Wei, and Wendell A Lim. “Oscillatory stress stimulation uncovers an Achilles’ heel of the yeast MAPK signaling network”. In: *Science* 350.6266 (2015), pp. 1379–1383.

[102] Alexander Y Mitrophanov and Eduardo A Groisman. “Positive feedback in cellular control systems”. In: *Bioessays* 30.6 (2008), pp. 542–555.

[103] Martin Montagne, Alexandre Martel, and Herve Le Moual. “Characterization of the Catalytic Activities of the PhoQ Histidine Protein Kinase of Salmonella entericaSerovar Typhimurium”. In: *Journal of bacteriology* 183.5 (2001), pp. 1787–1791.

[104] Travis I Moore, Ching-Shan Chou, Qing Nie, Noo Li Jeon, and Tau-Mu Yi. "Robust spatial sensing of mating pheromone gradients by yeast cells". In: *PloS one* 3.12 (2008), e3865–e3865.

[105] Michiko M Nakano, Peter Zuber, Philippe Glaser, Antoine Danchin, and F Marion Hulett. "Two-component regulatory proteins ResD-ResE are required for transcriptional activation of fnr upon oxygen limitation in Bacillus subtilis." In: *Journal of Bacteriology* 178.13 (1996), pp. 3796–3802.

[106] R Nath. "Properties of Barrier, a novel Saccharomyces cerevisiae acid protease". In: *Biochimie* 75.6 (1993), pp. 467–472.

[107] John A Nelder and R Jacob Baker. "Generalized linear models". In: *Encyclopedia of Statistical Sciences* (1972).

[108] Dan V Nicolau, Judith P Armitage, and Philip K Maini. "Directional persistence and the optimality of run-and-tumble chemotaxis". In: *Computational biology and chemistry* 33.4 (2009), pp. 269–274.

[109] Bela Novak and John J Tyson. "Numerical analysis of a comprehensive model of M-phase control in Xenopus oocyte extracts and intact embryos". In: *Journal of cell science* 106.4 (1993), pp. 1153–1168.

[110] Fernando Ortega, Jose L Garces, Francesc Mas, Boris N Kholodenko, and Marta Cascante. "Bistability from double phosphorylation in signal transduction". In: *Febs Journal* 273.17 (2006), pp. 3915–3926.

[111] Sarah P Otto. "The evolutionary enigma of sex". In: *the american naturalist* 174.S1 (2009), S1–S14.

[112] Saurabh Paliwal, Pablo A Iglesias, Kyle Campbell, Zoe Hilioti, Alex Groisman, and Andre Levchenko. "MAPK-mediated bimodal gene expression and adaptive gradient sensing in yeast". In: *Nature* 446.7131 (2007), pp. 46–51.

[113] Nikki M Parrish, James D Dick, and William R Bishai. "Mechanisms of latency in Mycobacterium tuberculosis". In: *Trends in microbiology* 6.3 (1998), pp. 107–112.

[114] Marta Perego, Philippe Glaser, and James A Hoch. "Aspartyl-phosphate phosphatases deactivate the response regulator components of the sporulation signal transduction system in Bacillus subtilis". In: *Molecular microbiology* 19.6 (1996), pp. 1151–1157.

[115] Marta Perego and James A Hoch. "Protein aspartate phosphatases control the output of two-component signal transduction systems". In: *Trends in Genetics* 12.3 (1996), pp. 97–101.

[116] Theodore J Perkins and Peter S Swain. "Strategies for cellular decision-making". In: *Molecular systems biology* 5.1 (2009), p. 326.

[117] John R Pierce. *An introduction to information theory: symbols, signals and noise*. Courier Corporation, 2012.

[118] Anna I Podgornaia and Michael T Laub. "Determinants of specificity in two-component signal transduction". In: *Current opinion in microbiology* 16.2 (2013), pp. 156–162.

[119] Francesc Posas, Mutsuhiro Takekawa, and Haruo Saito. "Signal transduction by MAP kinase cascades in budding yeast". In: *Current opinion in microbiology* 1.2 (1998), pp. 175–182.

[120] Chen Qian, Chui Ching Wong, Sanjay Swarup, and Keng-Hwee Chiam. "Bacterial tethering analysis reveals a "run-reverse-turn" mechanism for Pseudomonas species motility". In: *Applied and environmental microbiology* 79.15 (2013), pp. 4734–4743.

[121] Liang Qiao, Robert B Nachbar, Ioannis G Kevrekidis, and Stanislav Y Shvartsman. "Bistability and oscillations in the Huang-Ferrell model of MAPK signaling". In: *PLoS Comput Biol* 3.9 (2007), e184.

[122] J Christian J Ray and Oleg A Igoshin. "Adaptable functionality of transcriptional feedback in bacterial two-component systems". In: *PLoS Comput Biol* 6.2 (2010), e1000676.

[123] Alex Rhee, Raymond Cheong, and Andre Levchenko. "The application of information theory to biochemical signaling systems". In: *Phys. Biol.* 9.045011 (2012), pp. 354–358.

[124] AMIT Roy, CF Lu, DL Marykwas, PN Lipke, and J Kurjan. "The AGA1 product is involved in cell surface attachment of the Saccharomyces cerevisiae cell adhesion glycoprotein a-agglutinin." In: *Molecular and cellular biology* 11.8 (1991), pp. 4196–4206.

[125] Herbert M Sauro. *Enzyme kinetics for systems biology*. Future Skill Software, 2012.

[126] Michael A Savageau. "Alternative designs for a genetic switch: analysis of switching times using the piecewise power-law representation". In: *Mathematical biosciences* 180.1 (2002), pp. 237–253.

[127] Mark J Schnitzer. "Theory of continuum random walks and application to chemotaxis". In: *Physical Review E* 48.4 (1993), p. 2553.

[128] Jeffrey E Segall. "Polarization of yeast cells in spatial gradients of alpha mating factor". In: *Proceedings of the National Academy of Sciences* 90.18 (1993), pp. 8332–8336.

[129] Jeffrey E Segall, Steven M Block, and Howard C Berg. “Temporal comparisons in bacterial chemotaxis”. In: *Proceedings of the National Academy of Sciences* 83.23 (1986), pp. 8987–8991.

[130] Jangir Selimkhanov, Brooks Taylor, Jason Yao, Anna Pilko, John Albeck, Alexander Hoffmann, Lev Tsimring, and Roy Wollman. “Accurate information transmission through dynamic biochemical signaling networks”. In: *Science* 346.6215 (2014), pp. 1370–1373.

[131] Elissa P Sena, David N Radin, and Seymour Fogel. “Synchronous mating in yeast”. In: *Proceedings of the National Academy of Sciences* 70.5 (1973), pp. 1373–1377.

[132] Jacques-Alexandre Sepulchre and Alejandra C Ventura. “Intrinsic Feedbacks in MAPK Signaling Cascades Lead to Bistability and Oscillations”. In: *Acta biotheoretica* 61.1 (2013), pp. 59–78.

[133] Claude Elwood Shannon. “A mathematical theory of communication”. In: *ACM SIGMOBILE Mobile Computing and Communications Review* 5.1 (2001), pp. 3–55.

[134] Guy Shinar, Ron Milo, Maria Rodriguez Martinez, and Uri Alon. “Input-output robustness in simple bacterial signaling systems”. In: *Proceedings of the National Academy of Sciences* 104.50 (2007), pp. 19931–19935.

[135] Albert Siryaporn and Mark Goulian. “Cross-talk suppression between the CpxA-CpxR and EnvZ–OmpR two-component systems in E. coli”. In: *Molecular microbiology* 70.2 (2008), pp. 494–506.

[136] Noam Slonim, Gurinder S Atwal, Gasper Tkacik, and William Bialek. “Estimating mutual information and multi–information in large networks”. In: *arXiv preprint cs/0502017* (2005).

[137] John Maynard Smith and John Maynard-Smith. *The evolution of sex*. Cambridge Univ Press, 1978.

[138] Wiep Klaas Smits, Caroline C Eschevins, Kim A Susanna, Sierd Bron, Oscar P Kuipers, and Leendert W Hamoen. “Stripping Bacillus: ComK auto-stimulation is responsible for the bistable response in competence development”. In: *Molecular microbiology* 56.3 (2005), pp. 604–614.

[139] Kwangmin Son, Jeffrey S Guasto, and Roman Stocker. “Bacteria can exploit a flagellar buckling instability to change direction”. In: *Nature physics* 9.8 (2013), pp. 494–498.

[140] Victor Sourjik and Howard C Berg. “Receptor sensitivity in bacterial chemotaxis”. In: *Proceedings of the National Academy of Sciences* 99.1 (2002), pp. 123–127.

[141] Victor Sourjik and Ned S Wingreen. "Responding to chemical gradients: bacterial chemotaxis". In: *Current opinion in cell biology* 24.2 (2012), pp. 262–268.

[142] Joan R Strazdis and Vivian L MacKay. "Induction of yeast mating pheromone a-factor by α cells". In: (1983).

[143] Gurol M Suel, Jordi Garcia-Ojalvo, Louisa M Liberman, and Michael B Elowitz. "An excitable gene regulatory circuit induces transient cellular differentiation". In: *Nature* 440.7083 (2006), pp. 545–550.

[144] Kamakshi Sureka, Bhaswar Ghosh, Arunava Dasgupta, Joyoti Basu, Manikuntala Kundu, and Indrani Bose. "Positive feedback and noise activate the stringent response regulator rel in mycobacteria". In: *PLoS One* 3.3 (2008), e1771.

[145] Thapanar Suwanmajo and J Krishnan. "Mixed mechanisms of multi-site phosphorylation". In: *Journal of The Royal Society Interface* 12.107 (2015), p. 20141405.

[146] Shingo Suzuki, Ali Ferjani, Iwane Suzuki, and Norio Murata. "The SphS-SphR two component system is the exclusive sensor for the induction of gene expression in response to phosphate limitation in Synechocystis". In: *Journal of Biological Chemistry* 279.13 (2004), pp. 13234–13240.

[147] Peter S Swain, Michael B Elowitz, and Eric D Siggia. "Intrinsic and extrinsic contributions to stochasticity in gene expression". In: *Proceedings of the National Academy of Sciences* 99.20 (2002), pp. 12795–12800.

[148] Cheemeng Tan, Philippe Marguet, and Lingchong You. "Emergent bistability by a growth-modulating positive feedback circuit". In: *Nature chemical biology* 5.11 (2009), pp. 842–848.

[149] Yuichi Taniguchi, Paul J Choi, Gene-Wei Li, Huiyi Chen, Mohan Babu, Jeremy Hearn, Andrew Emili, and X Sunney Xie. "Quantifying E. coli proteome and transcriptome with single-molecule sensitivity in single cells". In: *Science* 329.5991 (2010), pp. 533–538.

[150] Mukund Thattai and Alexander Van Oudenaarden. "Stochastic gene expression in fluctuating environments". In: *Genetics* 167.1 (2004), pp. 523–530.

[151] Matthias Theves, Johannes Taktikos, Vasily Zaburdaev, Holger Stark, and Carsten Beta. "A bacterial swimmer with two alternating speeds of propagation". In: *Biophysical journal* 105.8 (2013), pp. 1915–1924.

[152] Joy A. Thomas and Cover Thomas M. *Elements of information theory*. Wiley, New York, 1991.

[153] Matthew Thomson and Jeremy Gunawardena. “Unlimited multistability in multisite phosphorylation systems”. In: *Nature* 460.7252 (2009), pp. 274–277.

[154] Ty M Thomson, Kirsten R Benjamin, Alan Bush, Tonya Love, David Pincus, Orna Resnekov, C Yu Richard, Andrew Gordon, Alejandro Colman-Lerner, Drew Endy, et al. “Scaffold number in yeast signaling system sets tradeoff between system output and dynamic range”. In: *Proceedings of the National Academy of Sciences* 108.50 (2011), pp. 20265–20270.

[155] CD Thron. “Bistable biochemical switching and the control of the events of the cell cycle”. In: *Nonlinear Analysis: Theory, Methods & Applications* 30.3 (1997), pp. 1825–1834.

[156] Abhinav Tiwari, Gabor Balazsi, Maria Laura Gennaro, and Oleg A Igoshin. “The interplay of multiple feedback loops with post-translational kinetics results in bistability of mycobacterial stress response”. In: *Physical biology* 7.3 (2010), p. 036005.

[157] Abhinav Tiwari and Oleg A Igoshin. “Coupling between feedback loops in autoregulatory networks affects bistability range, open-loop gain and switching times”. In: *Physical biology* 9.5 (2012), p. 055003.

[158] Abhinav Tiwari, J Christian J Ray, Jatin Narula, and Oleg A Igoshin. “Bistable responses in bacterial genetic networks: designs and dynamical consequences”. In: *Mathematical biosciences* 231.1 (2011), pp. 76–89.

[159] Gašper Tkačik, Curtis G Callan Jr, and William Bialek. “Information capacity of genetic regulatory elements”. In: *Physical Review E* 78.1 (2008), p. 011910.

[160] Tsz-Leung To and Narendra Maheshri. “Noise can induce bimodality in positive transcriptional feedback loops without bistability”. In: *Science* 327.5969 (2010), pp. 1142–1145.

[161] Jan-Willem Veening, Leendert W Hamoen, and Oscar P Kuipers. “Phosphatases modulate the bistable sporulation gene expression pattern in Bacillus subtilis”. In: *Molecular microbiology* 56.6 (2005), pp. 1481–1494.

[162] Jan-Willem Veening, Oleg A Igoshin, Robyn T Eijlander, Reindert Nijland, Leendert W Hamoen, and Oscar P Kuipers. “Transient heterogeneity in extracellular protease production by Bacillus subtilis”. In: *Molecular systems biology* 4.1 (2008).

[163] Jan-Willem Veening, Wiep Klaas Smits, and Oscar P Kuipers. “Bistability, epigenetics, and bet-hedging in bacteria”. In: *Annu. Rev. Microbiol.* 62 (2008), pp. 193–210.

[164] Alejandra C Ventura, Peng Jiang, Lauren Van Wassenhove, Domitilla Del Vecchio, Sofia D Merajver, and Alexander J Ninfa. "Signaling properties of a covalent modification cycle are altered by a downstream target". In: *Proceedings of the National Academy of Sciences* 107.22 (2010), pp. 10032–10037.

[165] Alejandra C Ventura, Jacques-A Sepulchre, and Sofia D Merajver. "A hidden feedback in signaling cascades is revealed". In: *PLoS Comput Biol* 4.3 (2008), e1000041.

[166] Daniel T Verhamme, Jos C Arents, Pieter W Postma, Wim Crielaard, and Klaas J Hellingwerf. "Investigation of in vivo cross-talk between key two-component systems of Escherichia coli". In: *Microbiology* 148.1 (2002), pp. 69–78.

[167] Christian Waltermann and Edda Klipp. "Information theory based approaches to cellular signaling". In: *Biochimica et Biophysica Acta* 1810.10 (2011), pp. 924–932.

[168] Liming Wang and Eduardo D Sontag. "On the number of steady states in a multiple futile cycle". In: *Journal of mathematical biology* 57.1 (2008), pp. 29–52.

[169] Katy Wei, Maxim Moinat, Timo R Maarleveld, and Frank J Bruggeman. "Stochastic simulation of prokaryotic two-component signalling indicates stochasticity-induced active-state locking and growth-rate dependent bistability". In: *Molecular BioSystems* 10.9 (2014), pp. 2338–2346.

[170] Stanly B Williams and Valley Stewart. "Discrimination between structurally related ligands nitrate and nitrite controls autokinase activity of the NarX transmembrane signal transducer of Escherichia coli K-12". In: *Molecular microbiology* 26.5 (1997), pp. 911–925.

[171] Hui Zhao, Zheng-Ming Shen, Peter C Kahn, and Peter N Lipke. "Interaction of α-agglutinin and a-agglutinin, Saccharomyces cerevisiae sexual cell adhesion molecules". In: *Journal of bacteriology* 183.9 (2001), pp. 2874–2880.

[172] Enikö Zörgö, Karolina Chwialkowska, Arne B Gjuvsland, Elena GarrE, Per Sunnerhagen, Gianni Liti, Anders Blomberg, Stig W Omholt, and Jonas Warringer. "Ancient evolutionary trade-offs between yeast ploidy states". In: *PLoS Genet* 9.3 (2013), e1003388.

[173] Martin Zumsande and Thilo Gross. "Bifurcations and chaos in the MAPK signaling cascade". In: *Journal of theoretical biology* 265.3 (2010), pp. 481–491.